

NORTHWESTERN UNIVERSITY

Modeling of Elastic Wave Propagation and
Viscoelastic Characterization of Biofilms and Soft Materials

A DISSERTATION

SUBMITTED TO THE GRADUATE SCHOOL
IN PARTIAL FULFILLMENT OF THE REQUIREMENTS

for the degree

DOCTOR OF PHILOSOPHY

Field of Mechanical Engineering

By

Hong-Cin Liou

EVANSTON, ILLINOIS

March 2020

© Copyright by Hong-Cin Liou 2020

All Rights Reserved

ABSTRACT

Modeling of Elastic Wave Propagation and
Viscoelastic Characterization of Biofilms and Soft Materials

Hong-Cin Liou

The viscoelastic properties of microbial biofilms have attracted great interests in recent years due to the ubiquity of biofilms and their wide range of industrial and municipal applications causing tremendous societal impacts. Biofilms are predominantly architected by extracellular polymeric substances (EPS) matrices composed of bacterial cells and biopolymers secreted by the cells. EPS matrices bridge the gene expression from bacterial cells and important explicit characteristics of biofilms (morphology, biological function, and physical robustness). It is believed that the viscoelastic properties of EPS play an important role to affect biofilms' characteristics, but these biofilm properties are understudied. The challenges of viscoelastic characterization in biofilms are due to their irregular geometry, spatially heterogeneous properties, and their delicate nature. In addition, most of existing tools are only suitable for rheological measurements at macro- or micro-scales, but not for mesoscale where numerous key features of biofilms directly link to. In this study, a novel framework of viscoelastic characterization for biofilms at mesoscale is developed. The framework combines Optical Coherence Elastography (OCE) technique and a theoretical acoustic wave model, where the former measures frequency-dependent phase velocity of elastic waves propagating in biofilms,

and the latter predicts dispersion curves based on given material properties, geometry, and boundary conditions. The viscoelastic properties of biofilms are determined through inverse modeling, calculating the dispersion curve that has the best curve-fitting result to the experimental data. This framework considers both a plate structure and a curved structure and are validated against soft hydrogel plates and spheres by obtaining their viscoelastic properties. Then, the framework is applied to estimate the shear modulus and viscosity of a lab-developed mixed-culture planar biofilm and a practical granular biofilm acquired directly from a full-scale wastewater processing reactor. This work represents the first attempt to explore elastic waves for quantitative mechanical characterization of biofilms in mesoscale. It provides a powerful tool that can facilitate the study of the relationships between biofilms' morphology, function, and mechanical properties.

Acknowledgments

First, I would like to express my deepest appreciation to my doctoral advisor Professor Balogun, who patiently guided me through this adventure of scientific exploration. His dedicated mentorship provided me with invaluable training from research vision and experimental skills to critical thinking and efficient communication of knowledge. It was a great privilege and honor to work with an advisor of the highest sincerity and kindness he possesses, and it would not be possible for me to complete this dissertation without his rigorous guidance and emphatic support in every aspect.

Besides my advisor, I would like to thank Dr. Fabrizio Sabba who provided not only the critical knowledge of biofilms and environmental engineering topics, but also the mentorship in interdisciplinary collaboration and academic writing. Dr. Sabba also broadened my horizon in terms of social relationships, work-life balance, and career vision. My friendship with him is one of the most precious assets I gained during my stay at Northwestern.

My sincere thanks also go to my thesis committee—Professor Wells and Professor Krishnaswamy—for their valuable feedback and generosity in reviewing my dissertation. The insight from Professor Wells regarding biofilms and their potential impact to our society was essential to my dissertation and the multiple successful publications from our collaboration.

It was a joyful journey to pursue my Ph.D. degree at Northwestern, working with a group of genius in the Center of Smart Structures and Materials and having accessible resources from the Department of Mechanical Engineering and the McCormick School of Engineering. I would also like to express my gratitude to the National Science Foundation

and the Department of Civil and Environmental Engineering for providing funding and Seed Grant that are absolutely indispensable for all the achievement in the dissertation.

Finally, I would like to thank my entire family. The warmest cheering from my family was always the best encouragement for me to persevere and tackle the challenges of language barrier, culture shock, and failures in research. I can never be grateful enough to my parents for their unimaginable effort devoted to the family and their unconditional support. I also would like to thank my aunt who has left us in a deeply unfortunate accident. Her ever-constant support, guidance, and love had always comforted me throughout my difficult times. This dissertation is dedicated to her and may her rest in peace.

Table of Contents

ABSTRACT	3
Acknowledgments	5
Table of Contents	7
List of Figures	9
List of Tables	13
Chapter 1. Introduction	14
1.1. Background	14
1.2. Research Vision and Objective	15
1.3. Review of Rheological Measurements on Biofilms	17
1.4. Research Approach	21
1.5. Chapters Layout	23
Chapter 2. Experimental Setup of Elastic Wave Generation and Detection	24
2.1. The Elastic Waves of Interest	25
2.2. The Frequency Response of the Paddle Actuator	26
2.3. Optical Coherence Tomography Microscope	27
Chapter 3. Mechanical Characterization of Planar Hydrogels and Biofilms	36
3.1. Introduction	36
3.2. Guided Wave Model of Plates	37

	8
3.3. Experimental Validation against Agarose Gel Phantoms	46
3.4. Viscoelastic Characterization of Planar Biofilms	53
3.5. Concluding Remarks	57
Chapter 4. Mechanical Characterization of Spherical Hydrogels	59
4.1. Introduction	59
4.2. Circumferential Interface Wave Model	60
4.3. Viscoelastic Characterization of Alginate Gel Spheres	75
4.4. Concluding Remarks	82
Chapter 5. Mechanical Characterization of Granular Biofilms	84
5.1. Introduction	84
5.2. Layered Circumferential Interface Wave Modeling	85
5.3. Local Wave Speed Probing	95
5.4. Viscoelastic Characterization of Alginate Gel Spheres with Biomass	107
5.5. Viscoelastic Characterization of a Granular Biofilm	111
5.6. Concluding Remarks	113
Chapter 6. Conclusions and Future Work	115
6.1. Key Findings and Significance	115
6.2. Opportunities for Future Work	117
References	118

List of Figures

1.1	The scope of this study. The part highlighted in red is of particular focus.	17
2.1	OCE experimental setup.	24
2.2	(a) Configuration of the knife-edge technique for frequency response characterization. (b) Relative amplitude of the axial displacement for the paddle actuator at different frequencies.	27
2.3	Relative locations of the reference beam and the sampling beam in the OCT interferometry.	29
2.4	Wave fringes in OCE images corresponding to different ωdt . (a) $\omega dt = 0.3\pi$, (b) $\omega dt = \pi$, and (c) $\omega dt = 2\pi$.	35
3.1	Geometry of the layered model. Symbols L and S represent compressional and shear waves. Positive and negative superscripts are used to indicate forward and backward (in z -direction) propagating partial waves.	38
3.2	Dispersion curves for (a) a pure-elastic layer with free-clamped boundary conditions, (b) a pure-elastic plate with liquid loading on the top surface and clamped boundary conditions at the bottom surface, and (c) and (d) a viscoelastic layer with liquid loading and clamped boundary conditions. The layer thickness is $h = 10$ mm for (a), (b), and (c), and $h = 1$ mm for (d).	45

		10
3.3	(a) OCT image of a 2.0% agarose gel phantom. The thickness of the water layer was reduced in this figure for visualization purposes. The experiments were conducted with a water layer of >2 mm thickness. (b) OCE image showing the distribution of phase difference $\Delta\phi$ for 1.4 kHz elastic waves in the sample. The pixel sizes along the x - and z -directions are 4 and 2 μm .	48
3.4	Measured guided elastic wave dispersion curves in agarose gel phantoms with (a) 1.0% and (b) 2.0% agarose concentrations, for different sample thicknesses.	50
3.5	Comparison of the measured dispersion data and the calculated dispersion curve of the guided elastic wave in gel samples with 1.0% (a and b), and 2.0% (c and d) agarose concentrations. Sample thickness = 10 mm in (a) and (c), and 1 mm in (b) and (d). Model parameters are listed in Table 3.1	51
3.6	The results of Rheometer measurements: (a) shear modulus and (b) complex viscosity.	52
3.7	(a) OCT image of a mixed-culture bacterial biofilm, (b) OCE image showing the distribution of the phase difference $\Delta\phi$ for the elastic wave at 660 Hz in the sample, and (c) dispersion curves calculated by the model (shear modulus 429 Pa and complex shear viscosity 0.06 Pa-s) and the dispersion data recorded in the experiment.	56
4.1	Geometry of the model cylinder for circumferential elastic waves. Symbols L and S represent longitudinal and shear waves. Positive and	

	negative superscripts represent outward and inward propagating partial waves. a and b are the inner and outer radii of the viscoelastic solid layer.	61
4.2	Validation of the theoretical model and the numerical calculation. Replicate of dispersion curves from Liu and Qu (1998) [97].	71
4.4	(a) OCT image and (b) OCE image showing circumferential interface wave propagation in an alginate gel sphere. An animated GIF file can be found in the supplementary information.	78
4.5	Experimentally measured elastic wave speeds in alginate gel samples and the best-fit dispersion curves calculated by the theoretical model. Each figure corresponds to an individual sample with the alginate concentration 0.8% (a–c) and 1.2% (d–f).	80
4.6	Mean values (circles) and standard deviations (error bars) for (a) shear moduli and (b) shear viscosities estimated for alginate gel samples.	82
5.1	Two-layered cylindrical model for circumferential interface wave.	86
5.2	Modified two-layered cylindrical model.	91
5.3	Comparison of dispersion curves for different inner core sizes.	93
5.4	Comparison of dispersion curves for different shear wave speeds of the inner core.	94
5.5	Model configuration of the numerical simulation.	97
5.6	(a), (c), and (e) Acoustic B-scans for the surface wave propagation in numerical simulations. (b), (d), and (f) Local wave speed estimation from the acoustic B-scans. Excitation frequency = 1 kHz (a and b), 2.1 kHz (c and d), and 4 kHz (e and f).	100

- 5.7 Mechanical resolution (L) of the local wave speed probing approach and the comparison to the wavelengths in the left and right regions (Λ_1 and Λ_2 , respectively). The inset shows the ratio of L/Λ_1 and L/Λ_2 . 101
- 5.8 Measurement of local wave speed probing on the layered agarose gel phantom. (a) OCT image showing the three layers. (b) OCE image recorded at 2.1 kHz showing the distribution of optical phase difference $\Delta\phi$. (c) Acoustic B-scan created by extracting $\Delta\phi$ from the white dashed line in (b) at different time delay. (d) Local wave speed estimated from the local slopes of the white dotted tracks in (c). 104
- 5.9 Images of the granular biofilm section recorded by the OCT microscope. (a) Camera image. (b) OCT image. (c) OCE image with wave excitation at 3.2 kHz. 105
- 5.10 Measurement of local wave speed probing on the granular biofilm section. (a) Acoustic B-scan created by extracting $\Delta\phi$ from the white dashed line in Fig. 5.9c at different time delay. (b) Local wave speed estimated from the local slopes of the white dotted tracks in (a). 106
- 5.11 (a) OCT image and (b) OCE image for the artificial alginate gel sphere with biomass. 108

List of Tables

3.1	Properties for the agarose gel phantoms estimated by the model.	51
4.1	Numerical values of Bessel functions $J_\nu(z)$ and $Y_\nu(z)$ calculated by three different algorithms. Red-colored numbers indicate the consistent digits with the reference.	70
4.2	Model inputs and estimated properties for alginate gel samples.	81
4.3	Mean values and variations of shear moduli and shear viscosities for alginate gel samples.	82
5.1	Model inputs and estimated properties for samples in Fig. 5.12.	111
5.2	Model inputs and estimated properties for the granular biofilm.	113

CHAPTER 1

Introduction

1.1. Background

Biofilms are microbial aggregates composed of multispecies bacterial cells and extracellular polymeric substances (EPS) produced by microorganisms. Although biofilms are ubiquitous, it was not until the late 1970s that we became familiar with the concept of biofilm introduced by a Canadian microbiologist Dr. John William Costerton [1]. The life cycle of biofilms starts from the planktonic bacteria cells floating in oligotrophic environments. When bacteria attach to a surface, they change their gene expression and switch from the planktonic state to the biofilm, producing biopolymers that provide the required adhesive force between the biofilm and the surface and the cohesive bonding within the biofilm. As the biofilm grows, both the bacterial cells and cell-polymer aggregates may detach and disperse in a planktonic form to a new area, initiating new biofilms [1, 2]. Among these different phases of the microbial life, biofilm is the most dominant one in aquatic, sediment, and soil environments [3, 4]. In most cases, biofilms are found detrimental. For example, biofouling often sabotages the industrial pipe systems or introduces unnecessary drag on maritime vehicles [5]. It has also been shown that biofilm-linked infections affect 17 million Americans annually, causing at least 550,000 deaths and placing an enormous economic burden on the US health care system [2]. On the contrary, some biofilms are beneficial. One example of this kind is the biofilms used in the wastewater treatment process for removing toxic substances or undesired chemicals in wastewater [5].

In wastewater treatment processes, together with the aforementioned surface-attached biofilms, another type of biofilms is also used. These biofilms form sphere-like aggregates typically at the millimeter scale [6–9] and they are termed as granular biofilm [10], granular sludge [11], granules [7, 8], or biogranules [6]. In this research, we will refer them as granular biofilm. In general, the forming process of granular biofilms is commonly separated by (1) initial inter-cell attachment induced by physical movement, (2) formation of micro-aggregates due to physical, chemical, and biochemical forces, (3) growth of cell clusters and EPS synthesis, and (4) granule maturation [7, 12]. Before the granular biofilms, their predecessor—flocculent sludge—has been widely used in wastewater treatment systems for decades. However, in recent years, granular biofilms have attracted great interests for their promising operational efficiency in wastewater treatment reactors to remove substances (carbon, nitrogen, phosphorous, organic pollutants [6, 7]) given their several advantages such as higher biomass density, stronger structure, shorter settling time, and less volume required to be separated from treated effluent [6–8, 12]. This study covers both types of biofilms—planar and granular—and aims at acquiring better understanding of biofilms’ characteristics that is urgently needed for developing strategies to mitigate detrimental biofilms as well as to retain beneficial biofilms.

1.2. Research Vision and Objective

Bacterial cells secrete a number of different EPS biopolymers, including polysaccharides, proteins, nucleic acids, and extracellular DNA [3, 5, 7]. Biopolymer secretion is predominantly affected by bacterial gene expression and the conditions of surrounding environment where the biofilms dwell, which ultimately leads to biofilms’ compositional and spatial heterogeneity [13]. The interaction of biopolymers in EPS matrices—entanglement,

protein binding, and cross-linking—play an important role in shaping the fundamental architecture of biofilms and presenting different topologies [14]. This EPS network provides biofilms the required cohesive bonding [15–19] and transient stress-bearing structure to resist external threats (invaders, chemicals, antibiotics, etc. [20–23]).

EPS are thought to dictate the physical robustness of biofilms, which is responsible for their numerous biological functions [24, 25]. Over the last few decades, researchers have investigated the physical properties of EPS [11, 19, 26–29], and these studies suggest that the EPS matrices are analogous to hydrogels since they share similar viscoelastic properties. For example, the behavior of EPS is solid-like under small strains as the storage (shear) modulus G' is always larger than the loss modulus G'' ; while under large strains, G'' may exceed G' so that the EPS is prone to be liquid-like [11, 19, 26, 27]. It is worth of highlighting that for hydrogels, the gelation phenomenon results from cross-linking between polymer chains, and the cross-link density is related to the storage modulus G' [19, 30]. These discoveries suggest that the viscoelasticity of the EPS is very crucial for the aggregation of biofilm; therefore, studying the viscoelastic properties can help elucidate key factors of interplays between biofilm structure and function.

Fig. 1.1 is a simplified layout of the scope for this study. It demonstrates the connections of the components related to biofilms. Bacterial cells produce biopolymers based on their gene expressions, which is affected by the environment, and the biopolymer network in the EPS controls the biofilm characteristics including structures, functions, and physical robustness. Among these characteristics, we aim at understanding the connection from physical robustness to other characteristics of biopolymers towards gene expression. Specifically, we focus on the viscoelastic properties of biofilms. In the next section, we will review the studies of biofilms' viscoelastic properties at different length scales, which provides a clear vision of the status quo, the knowledge gap, and the research need within the scope.

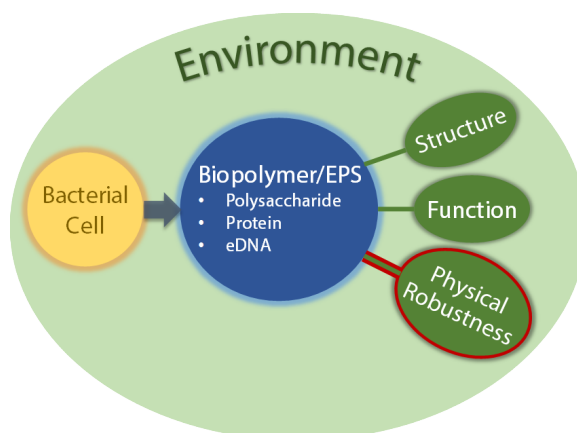


Figure 1.1: The scope of this study. The part highlighted in red is of particular focus.

1.3. Review of Rheological Measurements on Biofilms

Rheology is the metrology for measuring the viscoelastic properties of soft materials like biofilms. It investigates how a material reacts to a given force/torque. Different studies of rheological measurements on biofilms were reported, and, depending on the length scales, these studies can be categorized as macro- or micro-rheological measurements. The former is often at the scale of few centimeters while the latter is at few microns.

For macro-rheological techniques, rheometer is the most common apparatus to study biofilms. It often has the parallel-plate configuration with a fixed bottom plate that supports the sample and a moving top plate that applies shear stresses on the sample and monitors its responses. A rheometer typically operates in Amplitude Sweep or Frequency Sweep modes to measure the storage and loss moduli, depending on the need of the test. The former mode applies the shear load at a fixed frequency but with increasing amplitude; on the contrary, the latter mode increases the frequency of the shear load while fixing the amplitude. Examples of rheometer measurements on biofilms can be found in Wang *et al.* [11], Seviour *et al.* [19], Lin and Wang [26], and Ma *et al.* [27]. Although rheometry is a highly developed method for testing viscoelastic properties, it presents several limitations. Some rheometry tests are

destructive or quasi-destructive since the samples need to be prepared/trimmed to comply the geometry of the parallel plates. Also, as shown in Seviour *et al.* [19], the sample may not have the standard geometry, which may introduce large errors in the measurement results. Moreover, the rheometry tests can only be *ex situ* so that the sample properties may change when the sample is removed from its native environment.

Fluid shear is another method to apply shear load to the biofilm sample [2, 31]. In this method, biofilms often grow in channels where the nutrients are provided by the flowing fluid. The rate of the shear load can be changed by controlling the given flow, and the deformation of biofilms is monitored by time-lapse microscopy under different shear rate conditions. The biggest advantage of this method is that the measurements are implemented *in situ*. However, the growth environment of the tested biofilms is relatively artificial, which may bias certain gene expression in response to the given conditions.

Some other macro-rheological techniques were found very straightforward where uniaxial tension or compression tests were performed on biofilms [28, 32]. For specific kinds of bacteria that grow biofilm pellicle at the liquid surface, sample biofilms were grown between two movable plates that will be used to implement uniaxial tests [33, 34]. The advantage and disadvantage of this technique are similar to the fluid shear method—although this is an *in situ* test, biofilms need to grow in an artificial environment, whose properties may be biased due to human’s selection and may deviate from their counterpart in the natural environment.

For micro-rheology technique, literature has reported that atomic force microscopy (AFM) has been employed to study the cohesive bonding within the biofilm and the adhesive force between the biofilm and the surface it attaches to. AFM monitors the deflection of a micro-cantilever and relates the change of the deflection to the interaction force of interest. The report by Poppele and Hozalski showed an example of measuring the tensile

strength of biofilms using a micro-cantilever [35]. Aggarwal *et al.* adapted a similar setup and characterized the cohesiveness of intact biofilms [36]. Cooley *et al.* [37], Zeng *et al.* [38], and Chen *et al.* [39] demonstrated using AFM to study the interaction force between a single bacterium and the surface it attaches to. AFM is a very powerful tool especially in regard of studying the mechanics of a single cell or few cells. It can also be used to probe not only the local property of biofilms but also their topography. However, AFM measurements are basically *ex situ*, and the micro-cantilever usually makes contact with the sample. Also, the sampling region of AFM is limited to the sample surface, as such, it is unable to resolve property variations within the sample depth.

Some researchers have used magnetic micro-particles as embedded actuators to induce local dynamic responses in biofilms. The biofilms were grown in a fluid channel with a steady flow supply. The supplied flow carries the nutrients as well as the micro-particles so that the particles would be trapped in the EPS as the biofilms grow. During the tests, the magnetic particles were driven by a given magnetic field produced by external coils. Galy *et al.* [40] investigated the elastic and viscoelastic behavior of biofilms by applying a step force input to the particles in biofilms and monitoring the particle displacement. Using magnetic micro-particles as local actuators in the sample has the advantage of probing local properties and mapping the property heterogeneity. Also, the particles can be driven remotely by a magnetic field. However, it is a concern that the embedded particles may influence the biofilm growth, introducing biased selection of gene expression. Furthermore, this technique is only suitable for small-scale tests in the lab. It would be challenging to distribute particles in biofilms growing in industrial systems.

Optical tweezer (OT) is a relatively new technique in micro-rheology for soft materials yet applied to biofilms. The development of OT technique was awarded Nobel Prize [41], and OT is widely used for cell manipulation in biomedical field [42]. OT uses a focused laser

beam to generate forces on micrometer-sized particles. When the photons carried by the laser beam encounter the particle located on the optical path, their momentum changes when the photons are refracted or reflected. This momentum change provides the force exerted on the particle. When the particle is off axis or off focus, the momentum change is unbalanced on the particle, creating a finite net force to push the particle back to the equilibrium position. This technique was seen in the report by Leartprapun *et al.* which used an intensity-modulated laser to induce a local oscillation of a micro-particle to measure the resistance from the surrounding material [43]. A similar setup was used to test entangled DNAs to determine their frequency dependence of the linear elastic and viscous moduli [44]. OT shares similar advantages with magnetic particles such as the ability to excite dynamic responses remotely, to probe local properties, and to map the property heterogeneity. Furthermore, OT has better selectivity on the regions to excite since the laser beam has a more precise control on the particles. However, OT also has disadvantages similar to those of magnetic particles such as potential influences from embedded particles upon the biofilm growth and challenges to be applied to practical biofilms.

It can be summarized that the techniques reviewed above have some shared limitations: macro-rheological techniques only measure the bulk average of the properties and do not reveal the spatial variability and complexity of living biofilms [32, 40, 45], whereas micro-rheological techniques yield only highly localized measurements and are not capable of spatial mapping at the mm to cm scale [36, 46–49]. Here, we want to highlight that the length scales covered by these techniques are scattered on both extremes of the length spectrum—several millimeters to tens of millimeters for macro-rheological techniques and several micrometers to tens of micrometers for micro-rheological ones. However, metrology for biofilm characterization with the length scale between these two groups (mesoscale, 0.1–10mm) is understudied. It is worth noting that several key features of biofilms, such as rates

of biomass detachment, bulk mass transfer, and contaminant removal, are more directly linked to their mesoscale structure [50, 51]. Therefore, viscoelastic properties in mesoscale are extremely crucial within the scope of studying the relationships between physical robustness, structure, and function of biofilms. To this end, this study aims at developing a novel metrology approach for mesoscale viscoelasticity characterization of biofilms.

1.4. Research Approach

Recently, elastography techniques have enabled biomechanical characterization of soft structures by combining diagnostic imaging tools with specimen deformation approaches. In these techniques, the spatial deformation of a biological specimen is mapped under an applied external force, allowing for identifying regions with mechanical contrast and stiff tissues associated with different disease states. Existing elastography techniques include magnetic resonance elastography (MRE) [52], ultrasound elastography (USE) [53, 54], and optical coherence elastography (OCE) [55–57]. OCE is a powerful tool that overcomes the limitations of macro- and micro-rheology and is suitable for probing the viscoelastic properties of biofilms in mesoscale [57]. OCE has been used for viscoelastic characterization of soft biological materials, particularly in biomedical engineering field, to evaluate tissue mechanical properties [58–63]. OCE allows for 3D nondestructive imaging of mechanical properties with (1) high spatial resolution at micron-scale, (2) high displacement sensitivity at the nanoscale, which minimizes the required magnitude of the external load and prevents large disturbances in the sample, and (3) high sampling rate at 10–100 kHz, which enables real-time monitoring of the sample deformation. Moreover, the OCE image is co-registered with the Optical Coherence Tomography (OCT) image that shows sample’s internal structural features, such as pores in the matrix, which provides a useful tool to study the relationship between the sample morphology and mechanical properties [64].

OCE techniques can be classified as static or dynamic, depending on the time scale of the specimen deformation. Static OCE methods have been widely applied in biomechanical characterization experiments by the biomedical research community, where the heterogeneous strain map of tissue specimens produced in response to a uniform stress field has been used to predict the local Young's modulus [65]. This modulus is based on the ratio of the stress and strain, as obtained in a linear elastic solid. Measurements of viscoelastic properties, on the other hand, rely on tracking the temporal dynamics of the specimen deformation under an applied stress field. This is achieved using dynamic OCE methods, in which creep relaxation dynamics [66], elastic stress wave propagation [60, 61, 67–69], or underdamped acoustic vibrations [70, 71] are recorded using various motion tracking methods. Depending on the technique used to monitor the deformation, these methods can be classified into speckle tracking methods and phase sensitive OCT. The latter is of great interest and is used in this study because it provides a larger dynamic range for measurement and an inexpensive option for data acquisition [61].

This dissertation provides the first-of-its-kind OCE characterization of viscoelastic properties in bacterial biofilms based on elastic wave propagation measurement. Elastic wave-based dynamic OCE methods have been explored exclusively in biomedical applications for the characterization of viscoelastic properties in soft tissues [60, 67, 72]; however, biofilms have more complex geometrical and compositional features. These features, including irregular geometry (thickness, curvature, and roughness), heterogeneous composition, non-uniform porosity distribution, and bacterial hierarchical stratification [4, 73–76], make the modeling of elastic waves challenging and invaluable for interpreting the experimental data.

1.5. Chapters Layout

This study develops a novel metrology approach for mesoscale viscoelasticity characterization of both planar and granular biofilms. The approach combines the OCE measurement of elastic wave propagation and the inverse modeling to interpret the experimental results. The remainder of this dissertation is organized as follows:

- **Chapter 2** covers the background of elastic wave propagation in soft materials and the experimental apparatus, including the experimental setup, the frequency response of the wave source (the actuator), and the working principles of OCT microscope.
- **Chapter 3** details the development of the metrology approach in a soft plate, the validation against artificial agarose gel phantoms, and the application on a planar biofilm to estimate its shear modulus and viscosity.
- **Chapter 4** lays out the transition of the approach from a planar structure to a curved structure where the elastic waves propagate as circumferential waves. This transition was motivated by the surface curvature of granular biofilms. The approach of using circumferential wave to characterize the viscoelastic properties was validated against artificial alginate spheres.
- **Chapter 5** extends the modeling foundation laid in Chapter 4 to a layered curved structure, which was ultimately used for viscoelastic characterization of a granular biofilm. An additional method of local wave speed probing was also developed to obtain required information for the layered model.
- **Chapter 6** discusses the overall conclusions and suggests future work.

CHAPTER 2

Experimental Setup of Elastic Wave Generation and Detection

A schematic of the experimental configuration is shown in Fig. 2.1. The setup was used to generate and monitor elastic wave propagation in the samples. The waves were excited by a paddle actuator in light contact with the sample surface. The actuator was composed of a razor blade, an 18-gauge syringe needle, and a piezoelectric transducer (Thorlabs PZS001, NJ, USA) driven by a radio frequency function generator (Agilent 33120A, CA, USA). The function generator applied a sinusoidal voltage to the transducer to move the needle-blade assembly harmonically along its length, leading to small periodic indentation on the sample surface that generates harmonic elastic waves, including bulk waves—the compressional and shear waves—and surface waves. The local sample displacement induced by the elastic waves was then recorded with a phase-sensitive spectral-domain OCT system (Thorlabs GAN210C1). In this chapter, we cover the background related to the experiment and the apparatus, including (1) the elastic waves generated and the certain kinds that are of our interest, (2) the frequency response of the paddle actuator, and (3) the working principles of the OCT system.

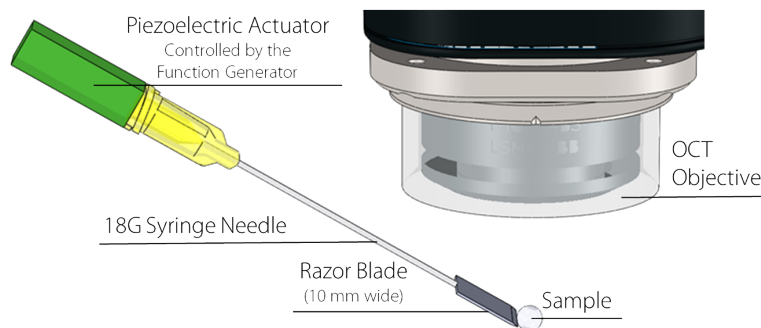


Figure 2.1: OCE experimental setup.

2.1. The Elastic Waves of Interest

The harmonic elastic waves generated by the experimental setup include bulk waves and surface waves. Bulk waves propagate through the interior regions of the sample and are reflected back into the sample or transmitted into the surrounding fluid at the sample boundaries; surface waves travel within the region that is near the sample boundary. Depending on the surface geometry and the boundary condition, the surface waves can be categorized into different kinds. In this study, we will discuss (1) Rayleigh wave, which travels at a traction-free and flat boundary, (2) Scholte wave, which travels at a liquid-loaded flat boundary, and (3) circumferential wave, which travels at a curved boundary. The third kind can be further distinguished as (a) normal circumferential wave when the boundary is traction-free and (b) circumferential interface wave when the boundary is loaded with liquid. Only type (b) is discussed in this study as the curved samples were submerged in water or their native aqueous solution during the experiments to preserve the moisture content or prevent changes to the material properties.

The choice of the elastic waves—bulk or surface waves—used in measurements affects the achievable spatial resolution. In soft samples, the wavelength of compressional waves in the kHz range is typically in the range of meters, while the wavelength of shear waves in the same frequency range is three orders of magnitude smaller. As such, shear waves in the kHz range are favored for acoustic mapping of elastic property variations in soft samples [77]. Operating with shear waves at MHz frequencies can lead to spatial resolution in the micron and sub-micron range; however, this is prohibited by attenuation of elastic waves resulting from the viscoelastic behavior of the materials.

For surface waves, their penetration depth predominantly affects their interaction with the sample structure and ultimately their propagation behavior. The penetration depth of the surface waves is positively related to the wavelength; therefore, it reduces with frequency.

When low-frequency waves are generated in thin samples where the elastic wavelengths are comparable to the sample thickness, the energy carried by the surface wave and shear wave would interact with the opposite boundary, overlap through the sample thickness, produce standing wave interference patterns, and propagate as guided waves in the lateral direction [78–80]. These guided waves have frequency-dependent (dispersive) phase velocities that depend on frequency, sample geometry, and sample material properties. This study relies on this dependency of dispersion relation on material properties to achieve the viscoelastic characterization of soft material phantoms and biofilms.

2.2. The Frequency Response of the Paddle Actuator

Since the local excitation of the elastic waves at different frequencies depends on the axial vibration of the actuator, it is important to investigate its dynamic responses within the frequency span. The dynamic response was characterized using the knife-edge technique as illustrated in Fig. 2.2a. A laser beam with constant beam width was guided directly to a photodetector which converts the detected intensity of the laser light to electric signal displayed on an oscilloscope. The laser beam was partially blocked by the edge of the razor blade so that the axial vibration of the actuator would cause the intensity variation of the laser beam that arrives at the photodetector. The peak-to-peak voltage, associated with the relative amplitude of the axial displacement, was recorded from the oscilloscope reading at every sampling frequency as shown in Fig. 2.2b. The result shows that the paddle actuator has three resonant frequencies (200 Hz, 2000 Hz, and 5800 Hz) and a region (1800–1900 Hz) with relatively low responses embedded in a moderate decreasing trend along the frequency. Nevertheless, sufficient vibration can be observed over the whole frequency span of interest, validating the capability of the paddle actuator to generate elastic waves.

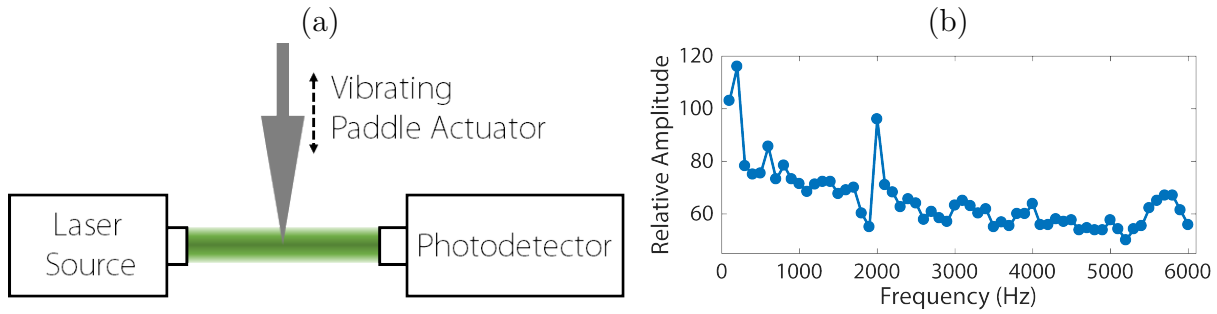


Figure 2.2: (a) Configuration of the knife-edge technique for frequency response characterization. (b) Relative amplitude of the axial displacement for the paddle actuator at different frequencies.

2.3. Optical Coherence Tomography Microscope

The OCT is operated with a near-infrared light source (center wavelength 930 nm and bandwidth 100 nm) and is capable of recording the sample morphology and the local dynamic response. The first kind of image output from the OCT microscope is a gray-scale image (termed as OCT image, e.g. Fig. 3.3a) which resolves sample’s morphology image. The OCT image is obtained by collecting a series of adjacent OCT A-scans and assembling the A-scans into a two-dimensional OCT B-scan in the x - z plane. Note that the definition of the terms “A-scan” and “B-scan” used in OCT community is different from those in the acoustics field, and we will specify them by “OCT A/B-scan” or “acoustic A/B-scan” when needed. The OCT A-scan corresponds to the one-dimensional scattering intensity along the vertical (z) direction through the depth of the sample, and the OCT B-scan is created by placing the OCT A-scans acquired along the x -direction together in sequence, meaning every pixel column in the OCT B-scan is a single OCT A-scan. As such, the intensity distribution in the OCT B-scan image represents the spatial variation of the local refractive index in the sample, which is correlated with the sample’s internal structure.

Here we provide the details of the OCT working principles [81, 82]:

Suppose the electric field of a light beam traveling in the space is described by

$$U(d, k, t) = E(k, t)e^{-ikd} \quad (2.1)$$

where $E(k, t)$ is the complex amplitude as a function of wavenumber k and time t , and d is the travel distance from the source reference. Then, the electric field of the reference beam from the OCT interferometer can be expressed as

$$U_R = E(k, t)a_R e^{-ik(2r)} \quad (2.2)$$

as a_R is the reflection potential which relates to the reflectivity R_R by the relationship:

$$R_R = a_R^2 \quad (2.3)$$

and $2r$ is the round-trip distance traveled by the reference beam.

Similarly, the light beam scattered from the sample can be expressed as

$$U_S = \int_0^\infty E(k, t)a(z)e^{-ik\cdot 2(r+nz)} dz \quad (2.4)$$

where $a(z)$ and $n = n(z)$ are the scattering potential and the refractive index, respectively, at different depth z in the sample. Note that the origin of z ($z = 0$) is at the location where the sampling beam travels a distance r from the source reference, rather than the sample surface as shown in Fig. 2.3. It's often the case that the sample surface is placed at $z = z_0$ with $z_0 > 0$.

Using the expressions of the reference beam and the sampling beam, the electric field of the light collected at the spectrometer can be written as a linear superposition of the two fields:

$$U_{total} = U_R + U_S = E(k, t) \left[a_R e^{-ik(2r)} + \int_0^\infty a(z) e^{-ik\cdot 2(r+nz)} dz \right] \quad (2.5)$$

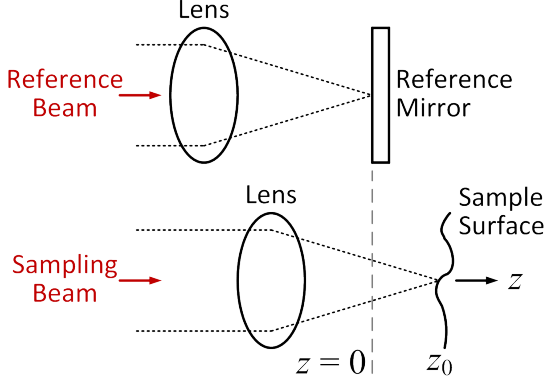


Figure 2.3: Relative locations of the reference beam and the sampling beam in the OCT interferometry.

and the intensity of U_{total} is defined by (assuming $a_R = 1$ for convenience)

$$I = \langle U_{total}^* U_{total} \rangle \quad (2.6)$$

where the angle brackets represent the temporal average with the definition:

$$\langle f(t) \rangle = \lim_{T \rightarrow \infty} \frac{1}{T} \int_{-T/2}^{T/2} f(t) dt \quad (2.7)$$

Substituting Eqn. 2.5 into Eqn. 2.6, we obtain

$$\begin{aligned} I &= \left\langle E^*(k, t) \left[e^{ik(2r)} + \int_0^\infty a(z') e^{ik \cdot 2(r+nz')} dz' \right] \cdot E(k, t) \left[e^{-ik(2r)} + \int_0^\infty a(z) e^{-ik \cdot 2(r+nz)} dz \right] \right\rangle \\ &= \left\langle E^*(k, t) E(k, t) \left[1 + 2 \int_0^\infty a(z) \cos(2knz) dz + \int_0^\infty \int_0^\infty a(z') a(z) e^{-ik \cdot 2n(z-z')} dz dz' \right] \right\rangle \end{aligned} \quad (2.8)$$

Note that all the terms in the square brackets of Eqn. 2.8 are time-independent, as such

$$I = S(k) \left[1 + 2 \int_0^\infty a(z) \cos(2knz) dz + \int_0^\infty \int_0^\infty a(z') a(z) e^{-ik \cdot 2n(z-z')} dz dz' \right] \quad (2.9)$$

where

$$S(k) = \langle E^*(k, t) E(k, t) \rangle \quad (2.10)$$

is the spectral density of the partially coherent light source of the OCT.

Now assume a function

$$\hat{a}(z) = a(z) + a(-z) \quad (2.11)$$

which is a symmetric expansion of $a(z)$; therefore,

$$\int_0^{\infty} a(z) \cos(2knz) dz = \frac{1}{2} \int_{-\infty}^{\infty} \hat{a}(z) \cos(2knz) dz \quad (2.12)$$

Substituting Eqn. 2.11 and 2.12 into Eqn. 2.9, yielding

$$I = S(k) \left[1 + \int_{-\infty}^{\infty} \hat{a}(z) \cos(2knz) dz + \frac{1}{4} \int_{-\infty}^{\infty} \int_{-\infty}^{\infty} \hat{a}(z') \hat{a}(z) e^{-ik \cdot 2n(z-z')} dz dz' \right] \quad (2.13)$$

It can be shown that

$$\int_{-\infty}^{\infty} \hat{a}(z) \cos(2knz) dz = \int_{-\infty}^{\infty} \hat{a}(z) e^{-i2knz} dz \quad (2.14)$$

since $\hat{a}(z)$ is an even function, and Eqn. 2.13 can be rewritten as

$$I = S(k) \left[1 + \int_{-\infty}^{\infty} \hat{a}(z) e^{-ik(2nz)} dz + \frac{1}{4} \int_{-\infty}^{\infty} \int_{-\infty}^{\infty} \hat{a}(z') \hat{a}(z) e^{-ik \cdot 2n(z-z')} dz dz' \right] \quad (2.15)$$

Note that in Eqn. 2.15, the second term in the square brackets is the Fourier transform of $\hat{a}(z)$; namely,

$$A(k) = \int_{-\infty}^{\infty} \hat{a}(z) e^{-ik(2nz)} dz \quad (2.16)$$

and the third term inside the square brackets is an autocorrelation term. If we use the *change of variables* formula, letting $\tau = z - z'$ and $\eta = z'$, then,

$$\begin{aligned}
d\tau d\eta &= |J(z, z')| dzdz' \\
&= \left| \det \begin{bmatrix} \frac{\partial \tau}{\partial z} & \frac{\partial \tau}{\partial z'} \\ \frac{\partial \eta}{\partial z} & \frac{\partial \eta}{\partial z'} \end{bmatrix} \right| dzdz' \\
&= \left| \det \begin{bmatrix} 1 & -1 \\ 0 & 1 \end{bmatrix} \right| dzdz' \\
&= dzdz'
\end{aligned} \tag{2.17}$$

and the autocorrelation term becomes

$$\begin{aligned}
\int_{-\infty}^{\infty} \int_{-\infty}^{\infty} \hat{a}(z') \hat{a}(z) e^{-ik \cdot 2n(z-z')} dzdz' &= \int_{-\infty}^{\infty} \int_{-\infty}^{\infty} \hat{a}(\eta) \hat{a}(\eta + \tau) e^{-ik \cdot 2n(z-z')} d\eta d\tau \\
&= \int_{-\infty}^{\infty} e^{-ik \cdot 2n\tau} \left[\int_{-\infty}^{\infty} \hat{a}(\eta) \hat{a}(\eta + \tau) d\eta \right] d\tau \\
&= AC(k)
\end{aligned} \tag{2.18}$$

which is the Fourier transform $AC(k)$ of the autocorrelation function acf in the square brackets of Eqn. 2.15.

From Eqn. 2.15 to Eqn. 2.18, the intensity is found to be a function of wavenumber k in the frequency domain:

$$\begin{aligned}
I &= I(k) \\
&= S(k) \left[1 + A(k) + \frac{1}{4} AC(k) \right]
\end{aligned} \tag{2.19}$$

Implementing inverse Fourier transform on $I(k)$ in Eqn. 2.19 yields

$$\mathcal{F}^{-1} [I(k)] = \mathcal{F}^{-1} [S(k)] \otimes [\delta(z) + \hat{a}(z) + acf] \tag{2.20}$$

where $\delta(z)$ is the Dirac delta function and $\hat{a}(z)$ is the target function of the OCT system which represents the scattering potential along the depth in the sample. Note that $\delta(z)$ and acf are centered at the origin of the z -axis and the widths of both functions depend on the optical property of the light source of the OCT, so if we select a proper value of z_0 , the target function $\hat{a}(z)$ can be separated from $\delta(z)$ and acf .

When the dynamic response is excited in the sample, inducing an axial (parallel to OCT's sampling beam) displacement u_z as a function of depth z , $u_z = u_z(z)$, the second term in the square brackets from Eqn. 2.15 becomes

$$\int_{-\infty}^{\infty} \hat{a}(z) e^{-ik \cdot 2n(z+u_z)} dz = \int_{-\infty}^{\infty} \hat{a}(z) e^{-ik \cdot 2n(u_z)} e^{-ik \cdot 2n(z)} dz \quad (2.21)$$

Thus, when implementing inverse Fourier transform, the corresponding term in Eqn. 2.20 becomes from $\hat{a}(z)$ to

$$\hat{a}(z) e^{-ik \cdot 2n(u_z)} \quad (2.22)$$

while the original scattering potential can be expressed in the complex plane by

$$\hat{a}(z) = \hat{a}(z) e^{-ik \cdot 2n(0)} \quad (2.23)$$

If we use the original scattering potential as the reference (without displacement), the phase difference between Eqn. 2.22 and Eqn. 2.23 induced by the displacement is

$$\Delta\phi = 2knu_z = \frac{4\pi nu_z}{\lambda_0} \quad (2.24)$$

as the wavenumber $k = 2\pi/\lambda_0$ and λ_0 is the center wavelength of the light source in OCT.

Eqn. 2.24 is the fundamental formula for OCT microscope to monitor the local dynamic response in the sample. Although the value of the optical phase ϕ in the OCT system may be random, the OCT can obtain the optical phase difference $\Delta\phi$ from two consecutive

A-scans recorded with a time delay dt . From Eqn. 2.24, the optical phase difference $\Delta\phi$ can be related to the local displacement from t to $t + dt$ as follow:

$$\Delta\phi(x, z, t) = 4\pi n(x, z)\Delta u_z(x, z, t)/\lambda_0 \quad (2.25)$$

where

$$\Delta u_z(x, z, t) = u_z(x, z, t + dt) - u_z(x, z, t) \quad (2.26)$$

For a quasi-static dynamic response whose variation rate is much smaller than the OCT frame rate, the response can be directly recorded by the default scanning settings in the OCT system. However, when the variation rate of the dynamic response is comparable to or higher than the OCT frame rate—like the elastic wave monitoring in this study—a synchronization device is needed to “freeze” the profile of the dynamic response at a certain time point. This profile of the dynamic response is the second kind of image output from the OCT microscope and is termed as OCE image (e.g. Fig. 2.4).

For example, if we attempt to capture the displacement profile of the continuous wave generated by the paddle actuator at $t = t_0$, at the location of the first pixel column $x = x_1$ in the OCE image, two exposures will be acquired at $t = t_0$ and $t = t_0 + dt$, respectively, to obtain $\Delta u_z(x_1, z, t_0)$. Then, at the location of the second pixel column $x = x_2$, two exposures will be acquired with a time delay T at $t = t_0 + T$ and $t = t_0 + T + dt$, respectively, to obtain $\Delta u_z(x_2, z, t_0 + T)$. If we let T to be the period of the continuous harmonic wave, then, because the harmonic wave has cyclic wave phase, $\Delta u_z(x_2, z, t_0 + T) = \Delta u_z(x_2, z, t_0)$. This relationship can be applied to every pixel column in the OCE image; that is, $\Delta u_z(x_n, z, t_0)$ at the n^{th} pixel column will be obtained at $t = t_0 + (n - 1)T$. Let's say the OCE image has totally m columns, then a total time $t_0 + (m - 1)T + dt$ is required to complete all exposures, whose equivalent frame rate f_{fr} would be $f_{fr} = 1/[(m - 1)T]$.

This technique to acquire the OCE image may give rise to some problems if the time delay dt between the two consecutive exposures is not carefully selected. Suppose the local displacement induced by the harmonic wave of angular frequency ω can be expressed by a sine function as

$$u_z(x, z, t) = A_0(x, z) \sin(\omega t + \gamma) \quad (2.27)$$

where $A_0(x, z)$ is the space-dependent amplitude and $\gamma = \gamma(x)$ is an initial phase shift. Then, the displacement difference $\Delta u_z(x, z, t)$ over the time delay dt is

$$\begin{aligned} \Delta u_z(x, z, t) &= A_0(x, z) \left\{ \sin [\omega(t + dt) + \gamma] - \sin(\omega t + \gamma) \right\} \\ &= 2A_0(x, z) \sin \left(\frac{\omega dt}{2} \right) \cos \left(\omega t + \frac{\omega dt}{2} + \gamma \right) \end{aligned} \quad (2.28)$$

which shows that $\Delta u_z(x, z, t)$ is a cosine function with an amplitude $2A_0(x, z) \sin(\omega dt/2)$. The amplitude will reach the maximal when $\omega dt = (4n+1)\pi$ and will vanish when $\omega dt = 2n\pi$ as $n = 1, 2, 3, \dots$

Fig. 2.4 shows the measurements with the same driving frequency ω with three different dt , which are $\omega dt = 0.3\pi$, π , and 2π . Note that the value of the phase difference $\Delta\phi$ ranges from $-\pi$ to π , but the color variation in the figures is set to saturate at the limits $-\pi/2$ and $\pi/2$ radians to enhance the color contrast. Also, because $\Delta\phi$ only ranges from $-\pi$ to π , when a $\Delta\phi$ value is larger than π , say 1.1π , it will flip over to the negative region and become -0.9π . This phenomenon is called phase wrapping. An example of phase wrapping is shown in Fig. 2.4a indicated by a dash-lined rectangle where the blue area should have the same sign with the surrounding red area.

Comparing Fig. 2.4a and b, several observations can be made: (1) The wave fringes have the same spatial variation throughout the field of view except a phase shift. The spatial variation is due to the same amplitude function $2A_0(x, z) \sin(\omega dt/2)$, and the phase shift is

resulted from the term $\omega dt/2$ in the cosine function. The relevant wave fringes are indicated by the arrows between the figures. (2) In Fig. 2.4b, the maximal amplitude is observed since $\omega dt = \pi$, showing stronger phase wrapping in the wave fringes than those in Fig. 2.4a. (3) The color contour is noisier in Fig. 2.4b than in Fig. 2.4a because a longer time delay would introduce more random background noise. On the other hand, in Fig. 2.4c, no wave fringes but random noise is observed, which validates the relation that $\Delta u_z = 0$ when $\omega dt = 2\pi$.

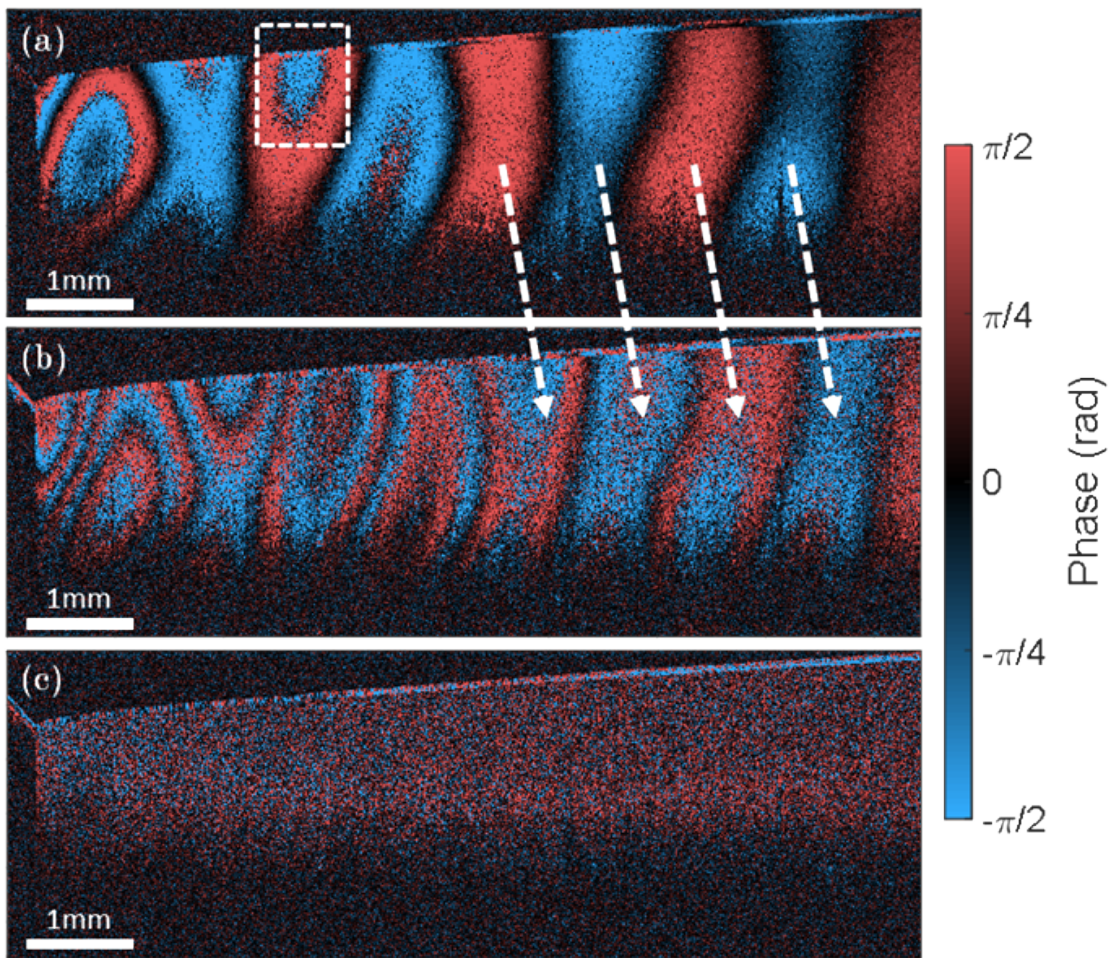


Figure 2.4: Wave fringes in OCE images corresponding to different ωdt . (a) $\omega dt = 0.3\pi$, (b) $\omega dt = \pi$, and (c) $\omega dt = 2\pi$.

CHAPTER 3

Mechanical Characterization of Planar Hydrogels and Biofilms

The content in this chapter is adapted from our previous publication: **Hong-Cin Liou**, Fabrizio Sabba, Aaron I. Packman, George Wells, and Oluwaseyi Balogun, “Nondestructive characterization of soft materials and biofilms by measurement of guided elastic wave propagation using optical coherence elastography,” *Soft Matter* **15**, pp. 575–586, (2019).

3.1. Introduction

This chapter provides the first-of-its-kind OCE characterization of viscoelastic properties in bacterial biofilms based on elastic wave propagation measurements. We first present a layered plate model that theoretically predicts the velocities of guided elastic waves at different frequencies in a soft viscoelastic plate with various thicknesses, shear moduli, and complex shear viscosities. The layered model simulates a soft plate in contact with a semi-infinite water/vacuum medium and a rigid substratum, which approximates the sample geometries tested by the OCE technique. The theoretical model was validated against experimental measurements in agarose gel phantoms of different thicknesses and concentrations. These experimental results on agarose gels were further verified by rheometry measurement. Then, the model was applied to estimate the viscoelastic properties of a mixed-culture bacterial biofilm from OCE measurements of the dispersion curves at frequencies up to 1 kHz. This chapter lays the foundation of the promising framework developed in this study for nondestructive quantification of biofilms’ viscoelastic properties based on elastic wave propagation measured by the OCE technique.

3.2. Guided Wave Model of Plates

3.2.1. Model Derivation

In this section, we present a model for guided elastic wave propagation in a multi-layer structure composed of a homogenous, isotropic, and viscoelastic hydrogel plate loaded by a water half-space on the top surface and attached to a stiff half-space at the bottom surface. A schematic diagram of the layered model system is shown in Fig. 3.1. The stiff (glass) substrate was assumed to be rigid since its Young's and shear moduli are orders of magnitude larger than those of the agarose gel layer. The water layer was assumed to be an ideal liquid which is homogenous, isotropic, inviscid, and does not support shear stresses. The model predicts the dispersion relation for the water loaded viscoelastic layer based on the solution to the elastodynamic wave equation for a homogeneous and isotropic material in the frequency domain, given by [83]

$$(\bar{\lambda} + \bar{\mu})\nabla(\nabla \cdot \vec{u}) + \bar{\mu}\nabla^2\vec{u} + \rho\omega^2\vec{u} = \vec{0} \quad (3.1)$$

where $\vec{u} = u_x\hat{e}_x + u_y\hat{e}_y + u_z\hat{e}_z$ is the displacement vector which comprises its components u_x , u_y , and u_z along x -, y -, and z - Cartesian axes with unit vectors \hat{e}_x , \hat{e}_y , and \hat{e}_z . ∇ is the differential operator in the three-dimensional space, ω is the angular frequency, ρ is the material density, and $\bar{\lambda}$ and $\bar{\mu}$ are the complex frequency-dependent relaxation functions of the Lamé material properties defined by

$$\bar{\lambda}(\omega) = \lambda + i\eta_\lambda\omega \quad (3.2)$$

$$\bar{\mu}(\omega) = \mu + i\eta_\mu\omega \quad (3.3)$$

where λ and μ are the asymptotic values of the relaxation functions, and η_λ and η_μ are complex viscosity terms. μ and η_μ represent the shear modulus and shear viscosity [84, 85], respectively, which are of particular interest in this work.

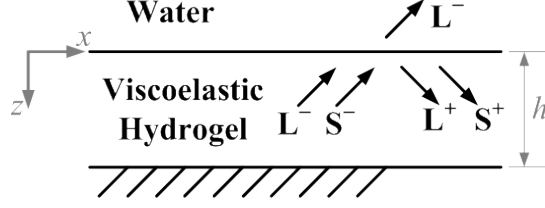


Figure 3.1: Geometry of the layered model. Symbols L and S represent compressional and shear waves. Positive and negative superscripts are used to indicate forward and backward (in z -direction) propagating partial waves.

It can be shown that the solution to Eqn. 3.1 in a plate is a linear superposition of a scalar potential ϕ and a vector potential $\vec{\psi}$, which are associated with compressional and shear waves, respectively:

$$\vec{u} = \nabla\phi + \nabla \times \vec{\psi} \quad (3.4)$$

where, under plane strain conditions ($u_y = 0, \partial/\partial y = 0$), the components of the displacement are $\vec{u} = (u_x, 0, u_z)$ and those of the vector potential are $\vec{\psi} = (\psi_x, \psi_y, \psi_z) = (0, \psi, 0)$. The potential functions can be expressed as the amplitudes and the phases of the partial waves, such as [84, 86, 87]

$$\phi = A_{L+}e^{i(k_x x + k_z^L z - \omega t)} + A_{L-}e^{i(k_x x - k_z^L z - \omega t)} \quad (3.5)$$

$$\psi = A_{S+}e^{i(k_x x + k_z^S z - \omega t)} + A_{S-}e^{i(k_x x - k_z^S z - \omega t)} \quad (3.6)$$

where $A_{L\pm}$ and $A_{S\pm}$ are complex amplitude coefficients with the letters L and S distinguishing partial longitudinal and shear waves and the \pm sign distinguishing downward (positive) and upward (negative) traveling directions of the partial bulk waves as illustrated in Fig. 3.1.

$k_z^{L,S}$ are the complex wave numbers in the vertical (z) direction which satisfy the following relationship:

$$\pm k_z^L = \pm \sqrt{\frac{\omega^2}{\alpha_L^2} - k_x^2} \quad (3.7)$$

$$\pm k_z^S = \pm \sqrt{\frac{\omega^2}{\alpha_S^2} - k_x^2} \quad (3.8)$$

where α_L and α_S are complex compressional and shear wave speeds, which are related to the material properties by the following relationships:

$$\alpha_L^2 = \frac{\bar{\lambda} + 2\bar{\mu}}{\rho} \quad (3.9)$$

$$\alpha_S^2 = \frac{\bar{\mu}}{\rho} \quad (3.10)$$

The real parts of α_L and α_S yield the bulk compressional and shear wave speeds, c_L and c_S , and their imaginary values are the attenuation coefficients of the bulk waves.

The local stress tensor is given by the Lamé constitutive relations:

$$\sigma_{zz} = \bar{\lambda}(\epsilon_{xx} + \epsilon_{zz}) + 2\bar{\mu}\epsilon_{zz} \quad (3.11)$$

$$\sigma_{xz} = 2\bar{\mu}\epsilon_{xz} \quad (3.12)$$

where

$$\epsilon_{xx} = \frac{\partial u_x}{\partial x} \quad (3.13)$$

$$\epsilon_{zz} = \frac{\partial u_z}{\partial z} \quad (3.14)$$

and

$$\epsilon_{xz} = \frac{1}{2} \left(\frac{\partial u_x}{\partial z} + \frac{\partial u_z}{\partial x} \right) \quad (3.15)$$

From Eqn. 3.4 to 3.15, the components of the local displacement and stress tensor can be expressed in the matrix form:

$$\begin{bmatrix} u_x \\ u_z \\ \sigma_{zz} \\ \sigma_{xz} \end{bmatrix} = i\mathbf{D} \begin{bmatrix} A_{L+} \\ A_{L-} \\ A_{S+} \\ A_{S-} \end{bmatrix} e^{i(k_x x - \omega t)} \quad (3.16)$$

where

$$\mathbf{D} = \begin{bmatrix} k_x e^{ik_z^L z} & k_x e^{-ik_z^L z} & -k_z^S e^{ik_z^S z} & k_z^S e^{-ik_z^S z} \\ k_z^L e^{ik_z^L z} & -k_z^L e^{-ik_z^L z} & k_x e^{ik_z^S z} & k_x e^{-ik_z^S z} \\ i\rho(\omega^2 - 2\alpha_S^2 k_x^2) e^{ik_z^L z} & i\rho(\omega^2 - 2\alpha_S^2 k_x^2) e^{-ik_z^L z} & 2i\rho k_x k_z^S \alpha_S^2 e^{ik_z^S z} & -2i\rho k_x k_z^S \alpha_S^2 e^{-ik_z^S z} \\ 2i\rho k_x k_z^L \alpha_S^2 e^{ik_z^L z} & -2i\rho k_x k_z^L \alpha_S^2 e^{-ik_z^L z} & -i\rho(\omega^2 - 2\alpha_S^2 k_x^2) e^{ik_z^S z} & -i\rho(\omega^2 - 2\alpha_S^2 k_x^2) e^{-ik_z^S z} \end{bmatrix} \quad (3.17)$$

The local displacement vector in the water layer can be expressed in terms of a potential function ϕ^W by the relationship:

$$\vec{u}^W = \nabla \phi^W \quad (3.18)$$

which is a special case of Eqn. 3.4 where the vector potential $\vec{\psi}$, related to the shear partial waves, vanishes.

The scalar potential in Eqn. 3.18 must satisfy the wave equation

$$\nabla^2 \phi^W + (k^W)^2 \phi^W = 0 \quad (3.19)$$

where $(k^W)^2 = k_x^2 + (k_z^W)^2$ is the wavenumber of the compressional wave in the water layer which comprises the components k_x and k_z^W in x - and z -directions and has the relation with the compressional wave speed $k^W = \omega/c^W$ as $c^W = 1481$ m/s in water. The water layer is treated as a half-space without wave sources. As such, only partial waves travelling in the negative z -direction exist, as illustrated in Fig. 3.1. In addition, we seek guided elastic wave solutions in the soft plate that travel at the water-plate interface as interface waves [63, 88], so the scalar potential can be expressed with the amplitude A_{L-}^W and the wavenumber k_x by

$$\phi^W = \left(A_{L-}^W e^{-ik_z^W z} \right) e^{i(k_x x - \omega t)} \quad (3.20)$$

From Eqn. 3.11, 3.13, 3.14, 3.18 and 3.20, the displacement and the pressure (equivalent to the normal stresses in solids) in the vertical direction in the water layer, u_z^W and p , can be derived

$$u_z^W = -i \left(k_z^W e^{-ik_z^W z} \right) A_{L-}^W e^{i(k_x x - \omega t)} \quad (3.21)$$

$$p = i \left(i \rho^W \omega^2 e^{-ik_z^W z} \right) A_{L-}^W e^{i(k_x x - \omega t)} \quad (3.22)$$

Since the water layer was assumed to be an inviscid liquid that does not support the propagation of shear waves, the shear stress in the water layer is zero, $\sigma_{xz}^W = 0$.

Five boundary conditions are needed to solve for the unknown coefficients for the potential functions in the soft plate and water layers. The boundary conditions include

(1) zero displacement at the bottom surface of the soft plate, $u_x|_{z=h} = u_z|_{z=h} = 0$, due to the rigid glass substratum

(2) continuity of the vertical displacements between the soft plate and the water layer,
 $u_z|_{z=0} = u_z^W|_{z=0}$

(3) continuity of the normal traction in the soft plate and the pressure in the water,
 $\sigma_{zz}|_{z=0} = p|_{z=0}$

(4) zero shear traction at the interface between the soft plate and the water layer,
 $\sigma_{xz}|_{z=0} = 0$

Applying these conditions leads to five equations for the potential function coefficients, which are expressed below in the matrix form [84, 89]:

$$\begin{bmatrix} k_x e^{ik_z^L h} & k_x e^{-ik_z^L h} & -k_z^S e^{ik_z^S h} & k_z^S e^{-ik_z^S h} & 0 \\ k_z^L e^{ik_z^L h} & -k_z^L e^{-ik_z^L h} & k_x e^{ik_z^S h} & k_x e^{-ik_z^S h} & 0 \\ i\rho(\omega^2 - 2\alpha_S^2 k_x^2) & i\rho(\omega^2 - 2\alpha_S^2 k_x^2) & 2i\rho k_x k_z^S \alpha_S^2 & -2i\rho k_x k_z^S \alpha_S^2 & -i\rho^W \omega^2 \\ 2i\rho k_x k_z^L \alpha_S^2 & -2i\rho k_x k_z^L \alpha_S^2 & -i\rho(\omega^2 - 2\alpha_S^2 k_x^2) & -i\rho(\omega^2 - 2\alpha_S^2 k_x^2) & 0 \\ k_z^L & -k_z^L & k_x & k_x & k_z^W \end{bmatrix} \begin{bmatrix} A_{L+} \\ A_{L-} \\ A_{S+} \\ A_{S-} \\ A_{L-}^W \end{bmatrix} = \mathbf{0} \quad (3.23)$$

or

$$\mathbf{S}\mathbf{A} = \mathbf{0} \quad (3.24)$$

To obtain non-trivial solutions for \mathbf{A} from Eqn. 3.24, the determinant of the coefficient matrix \mathbf{S} must equal to zero:

$$\det(\mathbf{S}) = 0 \quad (3.25)$$

which is the characteristic equation of the layered model. Solving the characteristic equation yields infinite solution pairs of angular frequency and complex wavenumber (ω, k_x) that represent the dispersion relation of the guided elastic waves in the water-loaded viscoelastic layer. The phase velocity (c) of the elastic wave propagating along the x -direction is obtained from the relation between the angular frequency ω and the real part of the complex wavenumber $\text{Re}\{k_x\} = k_x^R$, defined by $c = \omega/k_x^R$. Since the matrix \mathbf{S} is complex, Eqn. 3.25 is solved by searching the combinations of (ω, k_x) where the determinant of \mathbf{S} has zero magnitude, $|\det(\mathbf{S})| = 0$. Note that it may be difficult to achieve absolute zero in numerical calculation; therefore, in practice, the solutions are determined instead by locating local minima in the (ω, k_x) space.

3.2.2. Model Simulation

In this section, we present a set of dispersion curves predicted by the model for the guided elastic waves in the layered structure under different boundary conditions and mechanical properties as shown in Fig. 3.2. Each dispersion curve represents a unique elastic wave mode associated with a group of the solutions (ω, k_x) of Eqn. 3.25. Although there are an infinite number of dispersion curves for the model since the frequency can go to infinity, we only plotted the curves within the frequency range of 0–3000 Hz. First, we calculated the dispersion curves for a purely elastic plate with the mechanical properties and geometry

being the compressional wave speed $c_L = 1481$ m/s, the shear wave speed $c_S = 3$ m/s, zero complex viscosities $\eta_\lambda = \eta_\mu = 0$, and the layer thickness $h = 10$ mm. The compressional wave speed in the gel was assumed to be the same as that found in water because of the low concentration of agar in the gel phantoms. The large ratio of the compressional to the shear wave speeds corresponds to a Poisson's ratio of 0.5.

Fig. 3.2a shows the results from the stress-free and clamped boundary conditions imposed on the top and the bottom surfaces of the agarose layer, in which the water layer in Fig. 3.1 was replaced by a vacuum. Except for the non-dispersive mode with a frequency-independent phase velocity c_S , corresponding to the bulk shear wave propagation, each dispersion curve has a cut-off frequency (f_c) below which the associated elastic wave mode does not propagate. The cut-off frequencies occur at values of [85]

$$f_c = \frac{2n - 1}{4h} c_S, \quad n = 1, 2, 3, \dots \quad (3.26)$$

where the phase velocity tends to approach infinity. An implication of the infinite phase velocity at the cut-off frequency is that all points on the free surface of the layer vibrate in phase, leading to a shear-thickness resonance. We note that the phase velocities of all dispersive modes have decreasing trends with frequency and asymptotically approach the bulk shear wave speed c_S , except for the first mode. The asymptotic value of the first mode is the Rayleigh wave velocity of the layer, $c_R = 2.87$ m/s. The ratio $c_R/c_S = 0.96$ agrees with the theoretical prediction for a material that has a Poisson's ratio of 0.5 [63, 88]. The penetration depth of the Rayleigh wave is approximately one wavelength, over which the energy of the wave attenuates to $1/e$ of its maximum value at the layer surface. As such, the elastic mode reaches the asymptotic value and propagates as a pure surface wave without interference from the energy reflected from the bottom surface. As an example, consider an

agarose gel phantom with a thickness of 10 mm. When the frequency is larger than 500 Hz, the wavelength is 5.7 mm, which is smaller than the thickness of the agarose gel layer.

When the agarose gel layer is loaded with water on the top surface, the water loading decreases the Rayleigh wave velocity to the Scholte wave velocity $c_{Sch} = 2.52$ m/s, as shown in Fig. 3.2b. The Scholte wave propagates at the interface between the gel and the water layers whose elastic energy is attenuated along the transverse direction as part of the energy couples into the water layer. The ratio of $c_{Sch}/c_S = 0.84$ from our numerical calculation agrees well with analytical predictions [63, 88].

Fig. 3.2c shows the dispersion curves predicted by the model for a water-loaded viscoelastic layer of agarose gel. In this calculation, the material properties and the plate geometry remained the same as those used to obtain the results shown in Fig. 3.2a and 3.2b, with the sole exception that the complex shear viscosity was changed to $\eta_\mu = 0.15$ Pa-s. One significant difference between the dispersion curves in Fig. 3.2b and 3.2c is the increasing bulk shear and Scholte wave velocities in the high-frequency region due to the effect of viscosity, which is of particular interest in this study. Measurement of the dispersive phase velocity over this region can support characterization of the shear modulus and complex shear viscosity of the agarose gel sample. The dispersion curves also depend on the layer thickness, as shown in Fig. 3.2d, where the layer thickness is changed to 1 mm with the same material properties as in Fig. 3.2c. Comparing Fig. 3.2d to Fig. 3.2c, the most significant difference is that only three elastic modes are supported in the 1 mm thick layer, which correspond to the lowest interface wave, the bulk shear wave, and the second guided wave modes. The lowest mode in Fig. 3.2d has a higher cut-off frequency since this frequency is inversely proportional to the layer thickness.

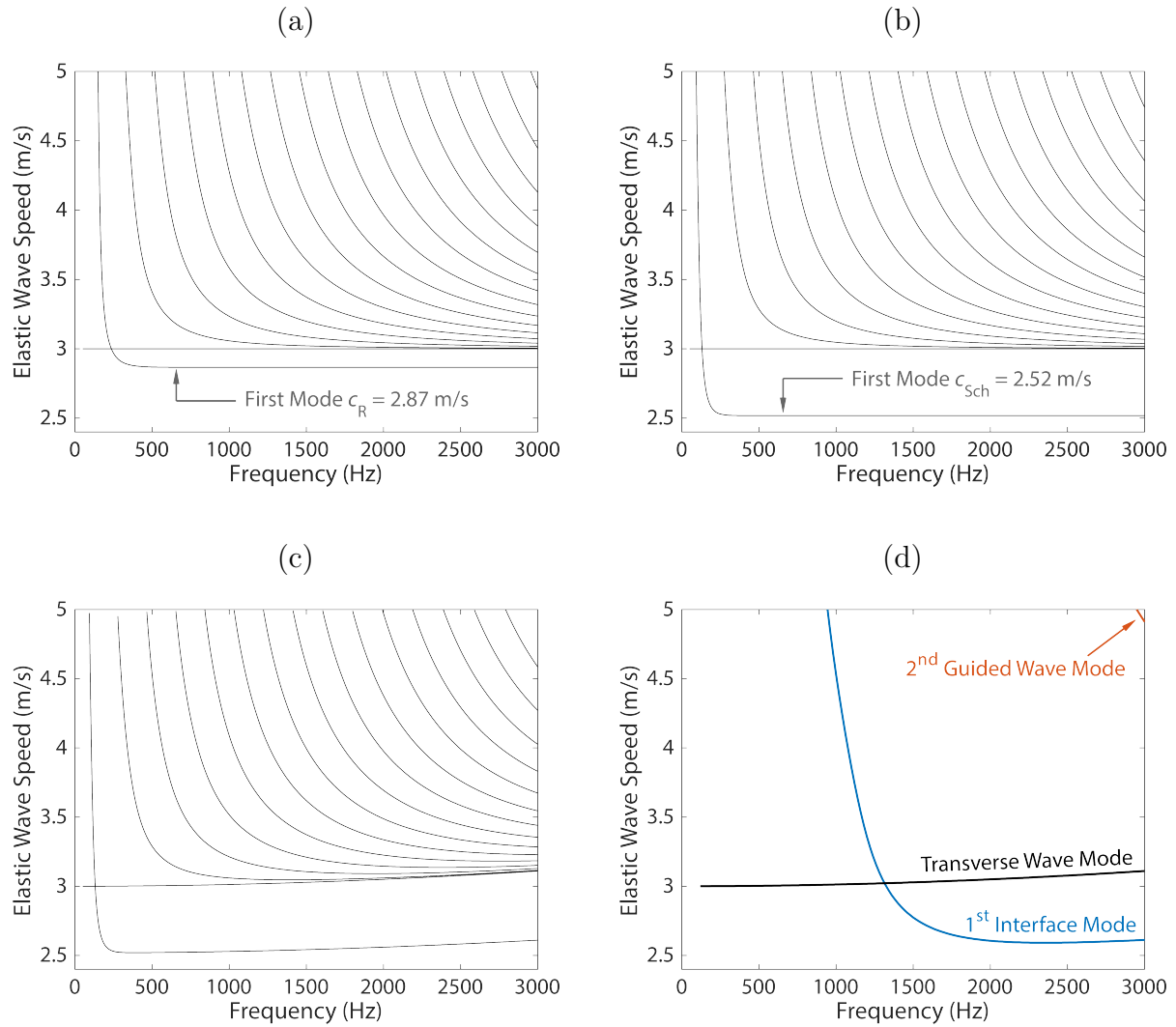


Figure 3.2: Dispersion curves for (a) a pure-elastic layer with free-clamped boundary conditions, (b) a pure-elastic plate with liquid loading on the top surface and clamped boundary conditions at the bottom surface, and (c) and (d) a viscoelastic layer with liquid loading and clamped boundary conditions. The layer thickness is $h = 10$ mm for (a), (b), and (c), and $h = 1$ mm for (d).

3.3. Experimental Validation against Agarose Gel Phantoms

3.3.1. Sample Preparation

Soft agarose (Fisher Bioreagents, BP1423-500, PA, USA) gel phantoms with 1.0% and 2.0% weight-to-volume (w/v) concentrations were prepared by mixing one and two grams of agarose powder, respectively, with a 100 mL solution made from 94 mL of nano-purified water and 6 mL of 5.0% w/v skim milk (Becton, Dickinson and Company, 232100, MD, USA). Milk was used to enhance optical scattering in the agarose samples and to improve the OCT image contrast of the sample morphology. The detailed protocol used to obtain samples with consistent mechanical properties and boundary flatness is listed below:

- (1) Pour 94 mL nano-purified water and 6 mL 5.0% w/v skim milk solution into a 250 mL Pyrex glass bottle.
- (2) Add certain weight of agarose powders to the solution according to the target concentration. Prevent any powder from attaching to the inner bottle wall above the solution surface.
- (3) Apply the cap to the bottle and boil the solution using a microwave oven. Cap must not be fully sealed to allow pressure release when the solution is being boiled. Turn off the microwave immediately once bubbles start forming due to vicious boiling.
- (4) Remove the bottle from the microwave oven and gently shake it to mix the undissolved powder.
- (5) Reheat the solution for a thorough boiling and mixture.
- (6) After reheating the solution, completely seal the cap to prevent any moisture loss. The bottle is then shaken for 10 seconds to uniformly dissolve the agar.
- (7) Cool off the bottle at room temperature for 20 minutes. Tilt and rotate the bottle so that the condensed water can go back into solution.

- (8) Pour the solution in the final container, cover the container to eliminate moisture loss, and leave them at room temperature for 90 minutes until the agarose gels are fully solidified.
- (9) Place the agarose gels in the water bath until the experiments are implemented to prevent moisture loss.
- (10) Wait 8 hours before performing any experiment to allow complete development of the cross-linking in the gels.

Fig. 3.3 shows representative OCT (Fig. 3.3a) and OCE (Fig. 3.3b) images obtained in the 2.0% w/v agarose gel phantom with a thickness of 10 mm. The sample was loaded with a water layer over the top surface. The excitation frequency for the wave fringes in Fig. 3.3b was 1.4 kHz. The OCT and OCE images were acquired over a lateral distance of 9 mm. The sample was tilted by 10 degrees relative to the vertical optical axis of the microscope objective to eliminate strong direct reflection of the probe light from the air-water and the water-agarose interfaces since that kind of light reflection would create multiple interferences in the interferometer of the OCT, leading artifacts in the images. The bright band in the OCT image is due to the strong contrast of the refractive index at the interface between air and water. In addition, the OCT image shows limited contrast in the agarose gel layer, suggesting that the sample is homogeneous without apparent structural features such as voids or cracks.

On the other hand, the OCE image shows a periodic distribution of the phase difference $\Delta\phi$ alternating between the minimum $-\pi$ and the maximum π radians along the lateral direction, which is associated with the periodic displacement of the elastic wave. The phase values were plotted within a smaller span $[-\pi/2, \pi/2]$ to enhance the color contrast. The spatial frequency ($\nu = 1/\Lambda$, where Λ is the wavelength) of the elastic wave was obtained by implementing a spatial fast Fourier transform from the data along the white dotted line, and

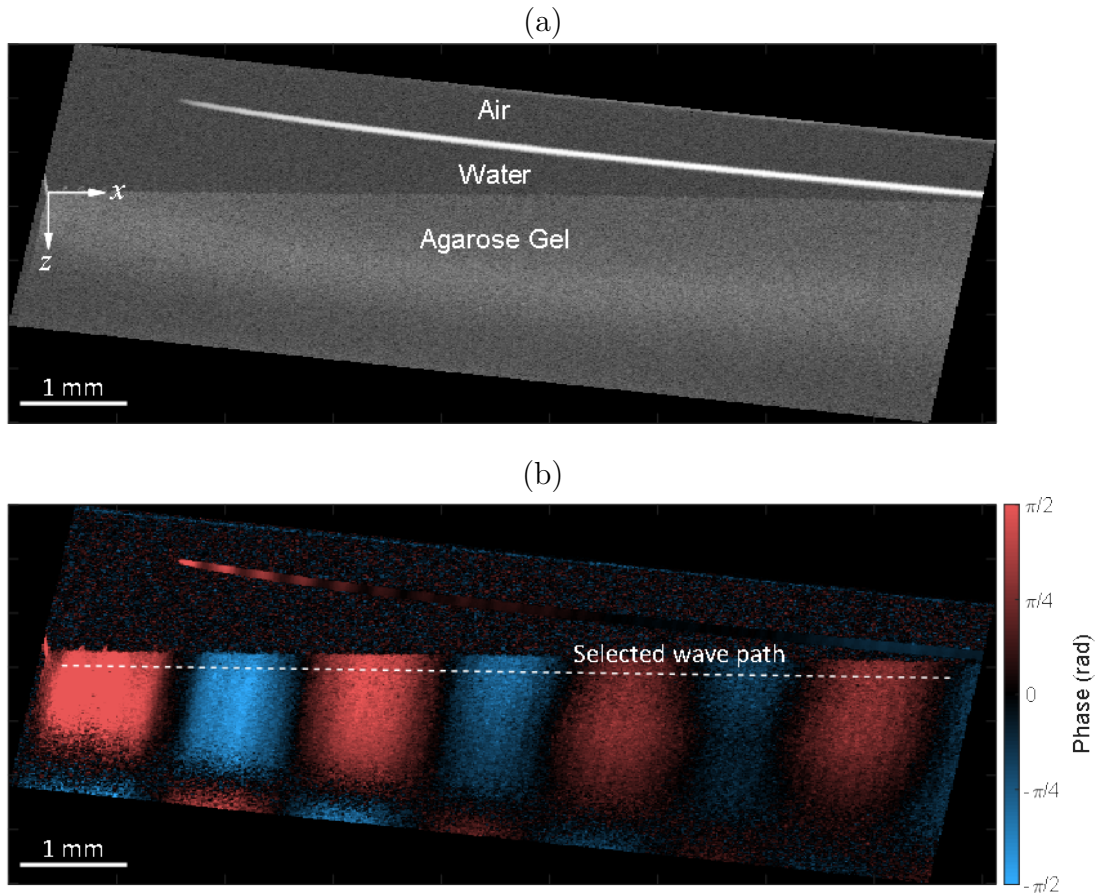


Figure 3.3: (a) OCT image of a 2.0% agarose gel phantom. The thickness of the water layer was reduced in this figure for visualization purposes. The experiments were conducted with a water layer of >2 mm thickness. (b) OCE image showing the distribution of phase difference $\Delta\phi$ for 1.4 kHz elastic waves in the sample. The pixel sizes along the x - and z -directions are 4 and 2 μm .

the phase velocity c of the elastic wave was determined based on the relationship $c = f\Lambda$, where f is the excitation frequency. The measurement was repeated at different excitation frequencies to collect the frequency-dependent phase velocity, the dispersion curve, for the excited elastic waves in the sample. The dispersion curve of an agarose gel plate is a function of the plate thickness and material properties, which were used to determine the shear modulus and the shear viscosity through the inverse analysis based on the model presented in the previous section.

3.3.2. Experimental Results of OCE Measurements

Fig. 3.4 shows experimental dispersion curves obtained for the 1.0% and 2.0% agarose gel phantoms of two thicknesses, 10 mm and 1 mm. The bandwidth of the measured dispersion curves was limited to 5 kHz due to the low signal-to-noise ratio of the OCE images, which stemmed from attenuation of the excited waves above this frequency. Each dispersion curve in Fig. 3.4 represents the average of nine measurements of the phase velocity versus frequency obtained at random positions in the sample. The error bars represent the standard deviation of these nine measurements. For all the experimental dispersion curves, the coefficient of variation (COV), defined as the ratio of standard deviation to the average value of the phase velocity, is less than 2.5%, suggesting homogeneity of the sample elastic properties. The dispersion curves for the 1 mm thick samples have a relatively constant wave speed within the high frequency range. The wavelength of the excited waves in the 1.0% agarose sample, for example, decreased from 1.29 mm to 0.38 mm in the frequency range of 1.2 to 4 kHz, which suggests that the excited wave changed from a guided wave at lower frequencies to a Scholte wave at higher frequencies. On the other hand, for the 10 mm thick samples, the Scholte wave mode was supported over the frequency bandwidth of the measurement since the wavelength was smaller than the sample thickness. As observed in the numerically-calculated dispersion curves, the phase velocity of the wave modes obtained in the 10 mm samples increased markedly with frequency due to the complex shear viscosity of the samples. In addition, the average phase velocity increased with the agarose concentration in the gel, as expected.

The dispersion curves in Fig. 3.4b show a decreasing trend in the low-frequency range, indicating that the measured mode belongs to the lowest elastic mode illustrated in Fig. 3.2. This is a reasonable observation since the Scholte wave was the predominant propagation mode near the interface [88, 90]. Fig. 3.5 shows the comparison of numerical calculations

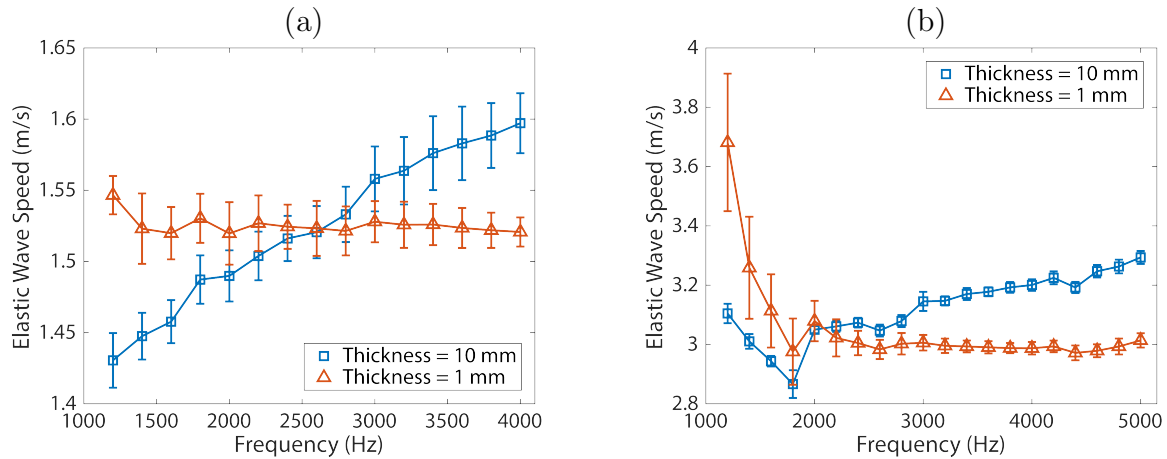


Figure 3.4: Measured guided elastic wave dispersion curves in agarose gel phantoms with (a) 1.0% and (b) 2.0% agarose concentrations, for different sample thicknesses.

of the dispersion curve for the first mode in the layered model to the experimental data. The shear modulus and complex shear viscosity were used as free fitting parameters in the numerical model for samples of 10 mm thickness, while shear modulus was the only free fitting parameter for samples of 1 mm thickness owing to the limited dispersion observed in these experiments. Good agreement was found between the experimental and numerical results, except for the larger errors observed within the low frequency range in Fig. 3.5c and 3.5d, which were due to the lack of sufficient periodic cycles of the waves within the OCE field of view to estimate the wavelength through fast Fourier transform. The shortest wavelength below 2 kHz in Fig. 3.5c and 3.5d was 1.65 mm; this is equivalent to less than six cycles within the total sampling distance in the OCE image, which limited the accuracy of the wavelength estimation. The best-fit material properties for the samples are listed in Table 3.1. The shear modulus and viscosity increase, as expected, with the concentration of agarose in the gel. The shear moduli measured from samples of 1 and 10 mm were similar at 1.0% and indistinguishable at 2.0%, and the values agree well with those reported in the literature [61, 77]. This finding validates the use of the layered model to determine the mechanical properties of viscoelastic materials.

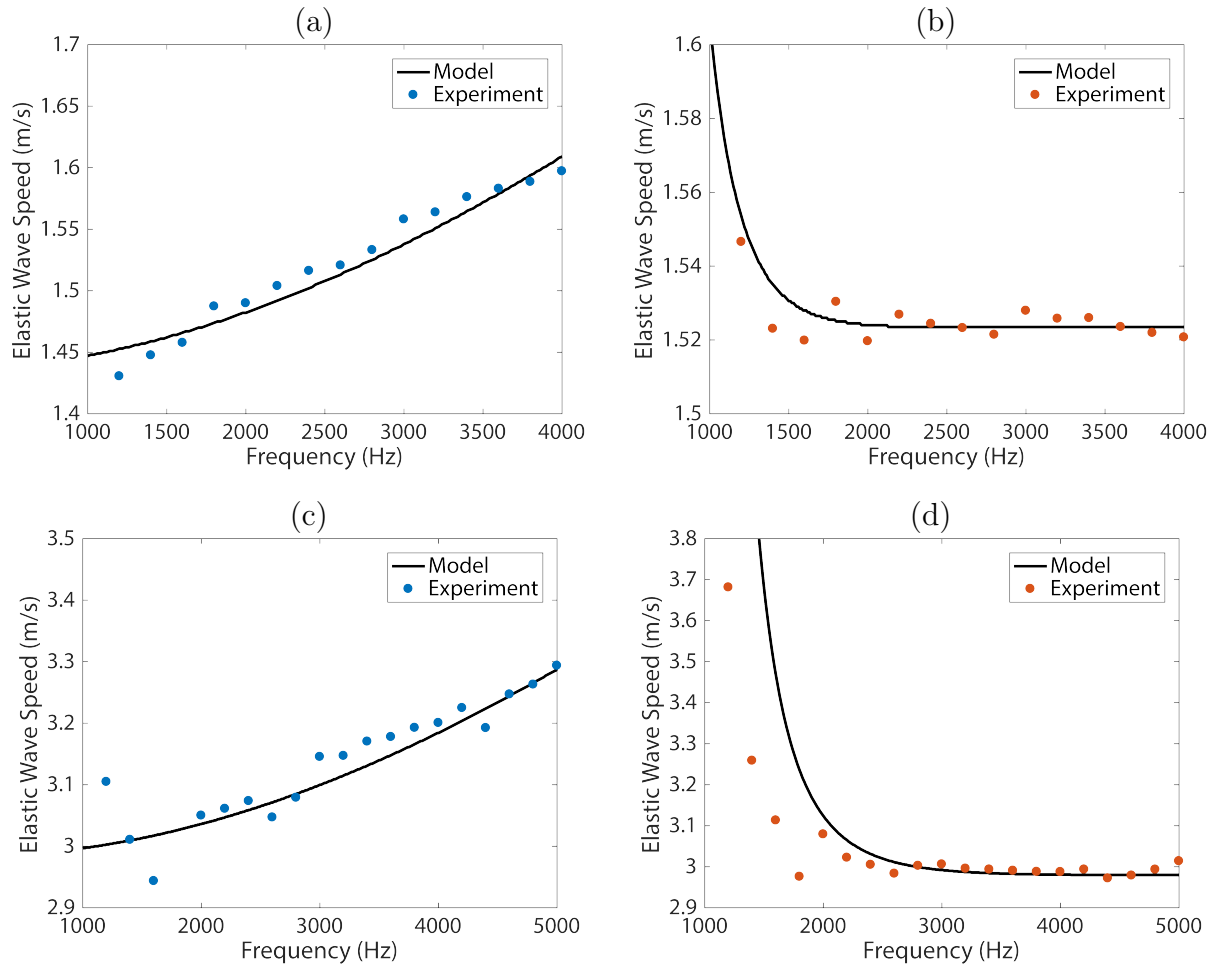


Figure 3.5: Comparison of the measured dispersion data and the calculated dispersion curve of the guided elastic wave in gel samples with 1.0% (a and b), and 2.0% (c and d) agarose concentrations. Sample thickness = 10 mm in (a) and (c), and 1 mm in (b) and (d). Model parameters are listed in Table 3.1

Table 3.1: Properties for the agarose gel phantoms estimated by the model.

Sample	(a)	(b)	(c)	(d)
Agarose gel concentration (w/v)	1.0%	1.0%	2.0%	2.0%
Thickness (mm)	10	1	10	1
Shear wave speed (m/s)	1.71	1.81	3.55	3.55
Shear modulus (kPa)	2.9	3.2	12.6	12.6
Complex shear viscosity (Pa-s)	0.07	—	0.22	—

3.3.3. Rheometer Measurements

A group of independent measurements using a Rheometer (Anton Paar MCR 302) was performed to obtain the complex shear modulus and viscosity in the 1 mm and 10 mm thick 2.0% agarose gel samples. The Rheometer experiments were conducted with the parallel plates configuration which used an upper rotating plate (diameter = 15 mm) that was in contact with sample's top surface to apply a torsional shear load on the sample. The sample was placed on a fixed lower plate, and its responses to the shear load were recorded to calculate the complex shear modulus and viscosity. The plates were operated under the Frequency Sweep Mode which recorded the complex shear modulus and viscosity at various angular frequencies of the rotating plate from 1 rad/s to 100 rad/s at a constant shear strain = 0.03%. The results of the shear modulus and viscosity are plotted in Fig. 3.6a and 3.6b, respectively. Each data point and error bar correspond to the mean value and the standard deviation from repeated measurements on three separate samples. From Fig. 3.6a, the averaged shear moduli for 1 mm and 10 mm thick samples over the angular frequency range from 1 rad/s to 10 rad/s, where the data points remain relatively constant, are 12.6

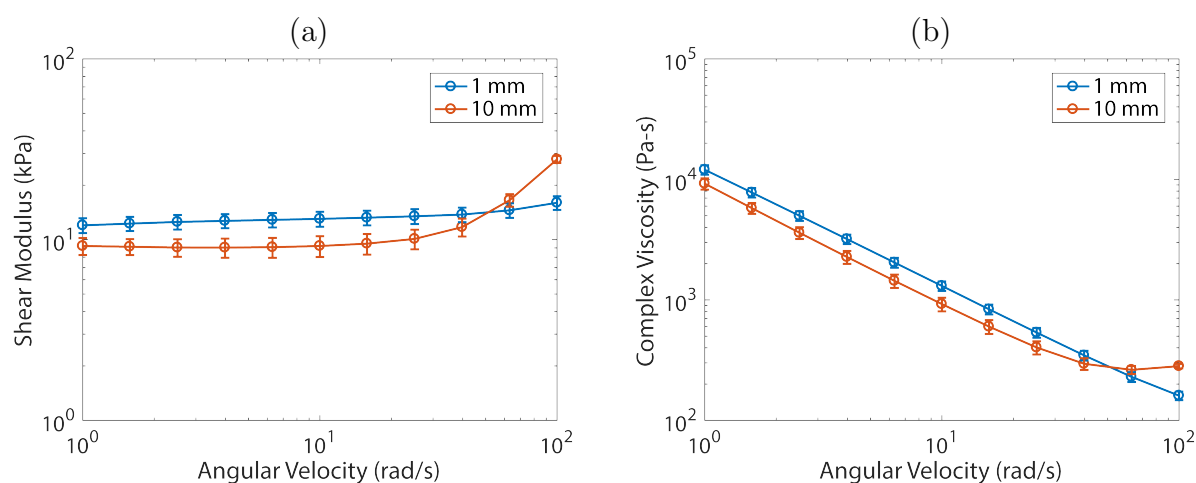


Figure 3.6: The results of Rheometer measurements: (a) shear modulus and (b) complex viscosity.

kPa and 9.1 kPa. The value 12.6 kPa of the 1 mm sample has extremely excellent agreement with our OCE measurements listed in Table 3.1, and the value 9.1 kPa of the 10 mm sample is within the same order of magnitude. This suggests that the OCE technique has high accuracy on estimating the shear moduli of soft materials. The results in Fig. 3.6b show that 1 mm and 10 mm thick agarose gels have comparable viscosities for angular frequency less than 40 rad/s. Beyond this frequency, the viscosity of the 10 mm sample is noticeably larger than that of the 1 mm sample. We remark that the lowest angular frequency of our OCE measurements on agarose samples was 6283 rad/s (1 kHz), which is significantly higher than the frequency range of the rheometer measurements. Nevertheless, the rheometer measurements suggest that the 10 mm thick sample has a larger viscosity compared to the 1 mm thick sample of the same composition, as observed in our OCE measurements.

3.4. Viscoelastic Characterization of Planar Biofilms

3.4.1. Sample Preparation

A series of heterotrophic biofilm samples was developed for the method's proof-of-concept using a Rotating Annular Reactor (RAR, Model 1320, Biosurface Technologies, Bozeman, MT, USA). The RAR was operated in batch mode for 24 hours after inoculation to allow the attachment of biomass to the coupons. After 24 hours, synthetic wastewater was fed into the RAR at a dilution rate of 5 d^{-1} . The system was inoculated with 25 mL of activated sludge from a local water reclamation plant (Hanover Park, IL, USA) and operated at 30 rpm and at a room temperature of 20–23°C. The reactor was constantly aerated and fed synthetic wastewater for 30 days in order to develop a thick mixed-culture bacterial biofilm, analogous to environmental biofilms commonly employed for contaminant removal in wastewater treatment biofilm reactors. The biofilm was predominantly composed of aerobic heterotrophs and growth was achieved on rectangular polycarbonate coupons designed with a specially

angled edge to match the slot inside the reactor and allow them to stay in place during long duration experiments (width 12.7 mm and length 150 mm; Biosurface Technologies, Bozeman, MT, USA). Additional details of biofilm growth and reactor operation and monitoring are available in a recent publication from our collaboration research group at Northwestern University [64].

3.4.2. OCE Measurements and Inverse Modeling

After 30 days of growth, the mixed-culture bacterial biofilm reached a thickness of ~ 2.5 mm with a variation of ~ 250 μm over a 4 mm lateral extent due to surface roughness, as shown in the OCT image (Fig. 3.7a) that illustrates the sample morphology. The OCE image obtained at an excitation frequency of 660 Hz and the dispersion curves from the numerical simulation and experimental measurements are shown in Fig. 3.7b and 3.7c, respectively. In order to more precisely calculate the speed of the elastic wave travelling along the curved surface, a cubic function was fitted to the curved region of the biofilm surface to approximate the propagation path of the elastic waves. The amplitudes at discrete intervals along the path were extracted, and the fast Fourier transform was applied to the data to obtain the spatial frequency (or inverse wavelength) of the elastic waves. The maximal excitation frequency in the measurement was limited to 1 kHz due to attenuation of elastic waves in the sample. Unlike the agarose gel sample, the OCT image of the biofilm shows internal structural variations due to the presence of pores (dark bands), which also results in the low phase amplitude of the elastic waves in the OCE image. This finding aligns with other observations that pores and structural heterogeneity are common in biofilms [91, 92].

The bright white bands in the OCT image indicate the boundary of the biofilm with air, and the propagation mode illustrated in the OCE image is a Rayleigh surface wave. The use of the Rayleigh wave measurement is particularly advantageous in this case since the

penetration depths of the wave, 1.2 mm at 550 Hz and 0.76 mm at 1 kHz, were less than the sample thickness and thus less sensitive to sample thickness variations. The dispersion curve for the measured data in Fig. 3.7c shows a 15% increase in phase velocity within the frequency bandwidth of the measurement. The measured dispersion curve was fitted by the numerical model using the biofilm shear modulus and viscosity as free fitting parameters. The best-fit shear modulus and complex shear viscosity are 429 Pa and 0.06 Pa-s. These estimated properties represent the average bulk viscoelastic properties of the biofilm, and they are within the broad range of reported values for the viscoelastic properties of biofilms (shear modulus = 10^{-1} to 10^5 Pa and viscosity = 10^{-1} to 10^{10} Pa-s) [93]. The broad range reflects both the diversity of different types of biofilms used in other studies and additional differences resulting from the inconsistencies and disadvantages of the characterization methods used. We highlight that most of the rheological techniques employed for property characterization are destructive or involve large disturbances in sample geometry when testing, which inevitably causes changes of the sample morphology and properties. In contrast, our novel technique has a nondestructive nature that prevents any structural change and allows the estimation of viscoelastic properties in the intact forms of the samples, which makes it more advantageous compared to other techniques.

We conclude that in our inverse modeling analysis, we assumed the bulk modulus of the biofilm to be equal to the bulk modulus of water due to the high ratio of water content (> 90%) in the sample. Overall, this novel approach provides a nondestructive, direct, local and *in situ* option to interrogate the mechanical properties in these types of systems. Further work that refines the layered model is needed to address the heterogeneous spatial distribution of the shear modulus in the sample, as suggested in Fig. 3.7b.

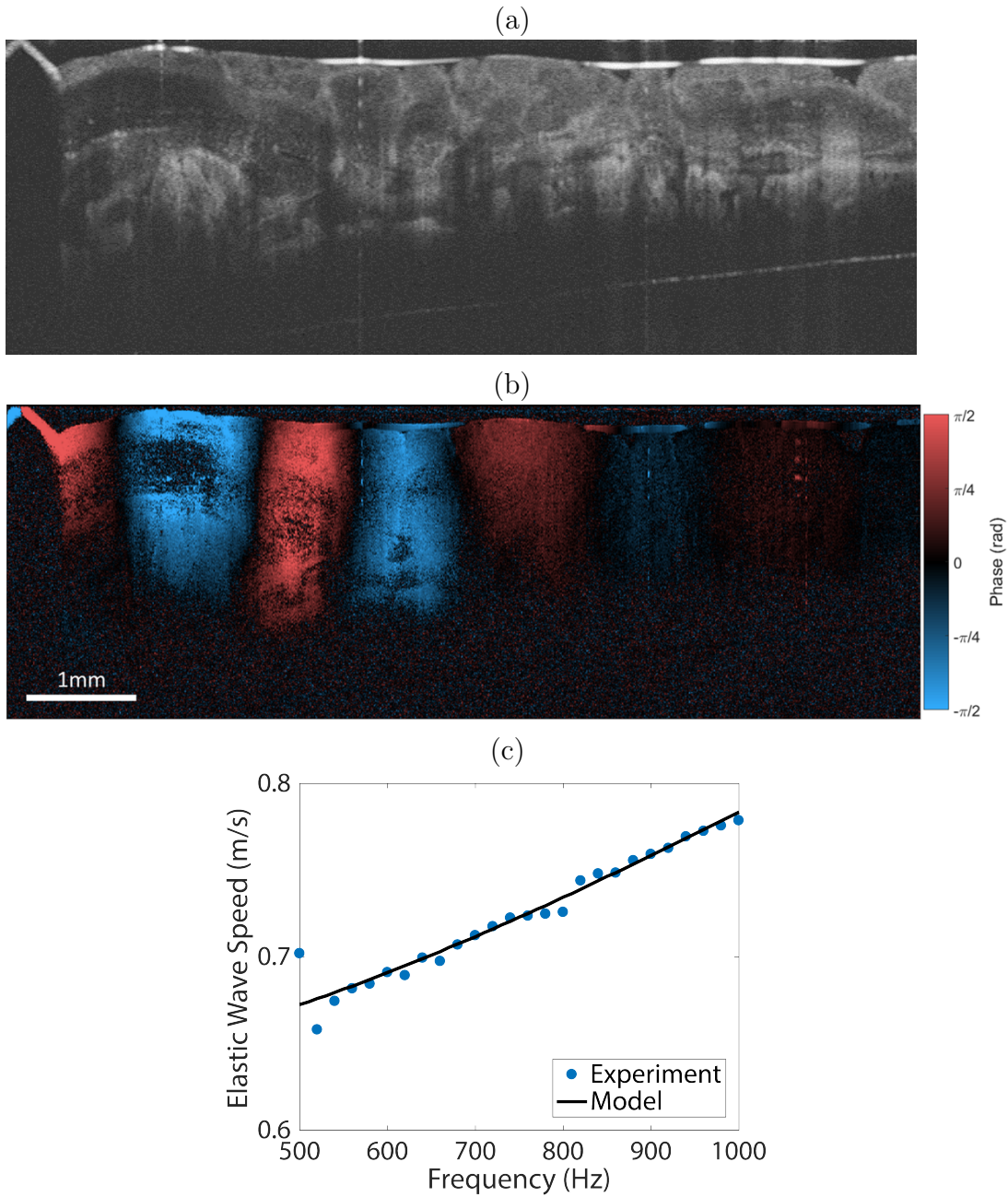


Figure 3.7: (a) OCT image of a mixed-culture bacterial biofilm, (b) OCE image showing the distribution of the phase difference $\Delta\phi$ for the elastic wave at 660 Hz in the sample, and (c) dispersion curves calculated by the model (shear modulus 429 Pa and complex shear viscosity 0.06 Pa-s) and the dispersion data recorded in the experiment.

3.5. Concluding Remarks

In this chapter, we developed a method combining OCE measurements and inverse modeling to characterize the mechanical properties of soft viscoelastic materials and bacterial biofilms. OCE was employed to obtain the dispersion curve—the frequency-dependent phase velocity—of the acoustic wave traveling in a biofilm supported by a rigid substrate. This is the first work to present wave propagation in biofilms, discover the frequency-dependent wave velocity, and interpret the dispersive wave velocity using a theoretical model to estimate the mechanical properties. The theoretical model predicted the dispersion curves of guided elastic wave modes by solving the elastodynamic wave equation for a layered viscoelastic plate with a rigid substratum at the bottom and a semi-infinite water/vacuum layer on the top. Dispersion in these materials depends on the mechanical properties, the geometry of the plate, and the presence or absence of water on the surface of the viscoelastic material. The model was validated by estimating the shear moduli and complex shear viscosities from the OCE measurements of phase velocities in the 10 mm and 1 mm thick agarose gel plates with 1.0% and 2.0% agarose concentrations. The estimation of the agarose gel properties agrees well with those reported in the literature and with our rheometer measurements. These results suggest that the wave propagation observed in the OCE measurements of the agarose gel plates belongs to the lowest elastic mode traveling near the top boundary of the plate. The influence of the plate geometry is crucial since the guided waves interact with the bottom boundary when the acoustic wavelength is larger than the plate thickness. We then used this approach to measure the shear modulus and complex shear viscosity in a bacterial biofilm, and we obtained reasonable results that are within the range reported in the literature. Since there is no “gold standard” measurement for mechanical properties in soft materials and biofilms, our nondestructive technique provides a novel approach for characterizing these properties without affecting the original status of the samples. Furthermore, this framework

enhances our understanding of elastic wave propagation in soft viscoelastic materials and provides the first proof-of-concept of OCE application to quantify the mechanical properties of biofilms that are critically important in diverse environments and applications.

CHAPTER 4

Mechanical Characterization of Spherical Hydrogels

The content in this chapter is adapted from our previous publication: **Hong-Cin Liou**, Fabrizio Sabba, Aaron I. Packman, Alex Rosenthal, George Wells, and Oluwaseyi Balogun, “Towards mechanical characterization of granular biofilms by optical coherence elastography measurements of circumferential elastic waves,” *Soft Matter* **15**, pp. 5562–5573, (2019).

4.1. Introduction

In Chapter 3, the approach that relies on OCE measurements of elastic wave propagation was shown to be suitable for characterizing the shear modulus and complex shear viscosity of a mixed-culture biofilm with plate-like geometry. While the plate-like biofilm was explored to demonstrate the feasibility of mechanical characterization in environmental biofilms using OCE, broadening the application of this technique to granular biofilms is challenging due to their curved geometries and depth-dependent properties that significantly complicate the elastic wave propagation.

In this chapter, we present the OCE measurements of elastic wave propagation in a granular biofilm and a theoretical model that is capable of predicting the dispersion (frequency-dependent wave speed) of circumferential elastic waves in a cylindrical viscoelastic solid. The model can approximate the propagation of elastic waves along a circular contour of fixed radius in a spherical sample and is used for inverse analysis to estimate the viscoelastic properties from OCE measurements of elastic wave propagation. The inverse analysis approach was validated on alginate spheres with two different concentrations, from

which their shear moduli and complex shear viscosities were obtained. We chose alginate as a model system for the OCE measurements because it is commonly present in granular biofilm EPS [15, 28, 94]. The combination of the modeling and experimentation approaches reported in this chapter presents a promising framework towards nondestructive characterization of viscoelastic properties in practical environmental biofilms with curved geometries.

4.2. Circumferential Interface Wave Model

4.2.1. Model Derivation

In this section, a theoretical model for calculating the frequency-dependent phase velocity of circumferential elastic waves in a viscoelastic solid with curved geometry is presented. This model was used to quantify the shear modulus and complex shear viscosity of the alginate gel samples through inverse analysis from experimental measurements. To reduce modeling complexity, a one-layered cylindrical geometry illustrated in Fig. 4.1 was adopted. The inner and outer radii of the layer are labeled as a and b , respectively. The cylinder has a hollowed space inside and is surrounded by an inviscid water half-space ($r > b$) that does not support shear stresses. The purpose of the hollowed space will be discussed later when the boundary conditions are applied. All material properties in this structure are homogeneous and isotropic. It has been shown that the waveform supported on the surface of a homogeneous and isotropic sphere is toroidal [95, 96]. The propagation of a toroidal wave can be monitored by probing only on the meridian (the big circle) that is normal to the wavefront. As such, the toroidal wave propagation can be approximated by the circumferential wave that travels on the surface of a cylinder with the same curvature of the meridian. Therefore, the cylindrical configuration of this model structure is valid and provides a simple approach for modeling the key features of the wave that is of particular

interest in this chapter: (1) a circumferential wave that travels along a circular contour, and (2) an interface wave that propagates at the interface between the solid and the water.

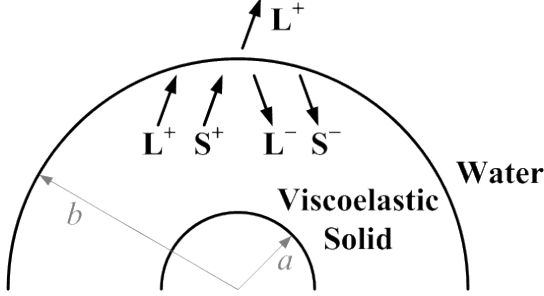


Figure 4.1: Geometry of the model cylinder for circumferential elastic waves. Symbols L and S represent longitudinal and shear waves. Positive and negative superscripts represent outward and inward propagating partial waves. a and b are the inner and outer radii of the viscoelastic solid layer.

The elastodynamic wave equation formulated in cylindrical coordinates for harmonic wave propagation in a homogeneous, isotropic, and viscoelastic solid has the same expression as Eqn. 3.1, but the components of the displacement vector \vec{u} and the differential operator ∇ are converted to the cylindrical coordinates, such as

$$\vec{u} = u_r \hat{e}_r + u_\theta \hat{e}_\theta + u_z \hat{e}_z \quad (4.1)$$

which comprises the components u_r , u_θ , and u_z along r -, θ -, and z -directions with unit vectors \hat{e}_r , \hat{e}_θ , and \hat{e}_z , and

$$\nabla = \hat{e}_r \frac{\partial}{\partial r} + \hat{e}_\theta \frac{1}{r} \frac{\partial}{\partial \theta} + \hat{e}_z \frac{\partial}{\partial z} \quad (4.2)$$

Note that the constitution relation of the material is independent of the coordinate system since the material is considered to be homogeneous and isotropic; therefore Eqn. 3.2 and 3.3 are also applicable in this section.

As shown in Eqn. 3.4, the solution \vec{u} to Eqn. 3.1 is a linear superposition of the contributions from longitudinal and shear waves, where, under cylindrical coordinates, the vector potential $\vec{\psi} = (\psi_r, \psi_\theta, \psi_z)$. To consider only the plane circumferential interface waves, plane strain conditions are imposed on the displacements and stresses such that (1) the displacement component in the z -direction vanishes ($u_z = 0$), and (2) gradients along the

z -direction are zero ($\partial/\partial z = 0$). From the first condition, the first two components of $\vec{\psi}$ must equal to zero ($\psi_r = \psi_\theta = 0$), yielding $\vec{\psi} = (0, 0, \psi)$. From the second condition, the third term of the differential operator in Eqn. 4.2 vanishes.

Substituting Eqn. 3.4 into Eqn. 3.1, with the conversion of components into cylindrical coordinate system listed in Eqn. 4.1 and 4.2, leads to the Helmholtz equations for the scalar and vector potentials:

$$\left(\frac{\partial^2}{\partial r^2} + \frac{1}{r} \frac{\partial}{\partial r} + \frac{1}{r^2} \frac{\partial^2}{\partial \theta^2} \right) \phi + \frac{\omega^2}{\alpha_L^2} \phi = 0 \quad (4.3)$$

$$\left(\frac{\partial^2}{\partial r^2} + \frac{1}{r} \frac{\partial}{\partial r} + \frac{1}{r^2} \frac{\partial^2}{\partial \theta^2} \right) \psi + \frac{\omega^2}{\alpha_L^2} \psi = 0 \quad (4.4)$$

where α_L and α_S are complex compressional and shear wave speeds that are related to the material properties by the relationships in Eqn. 3.9 and 3.10.

Following related work in the literature [97, 98], the scalar and vector potential functions corresponding to circumferential interface waves in the solid cylinder are defined as

$$\phi = \Phi(r) e^{i(kb\theta - \omega t)} \quad (4.5)$$

$$\psi = \Psi(r) e^{i(kb\theta - \omega t)} \quad (4.6)$$

where $\Phi(r)$ and $\Psi(r)$ represent the complex amplitudes along the radial (r) direction; k is the complex wavenumber whose real part $\text{Re}\{k\} = k^R$ is related to the wavelength Λ by $k^R = 2\pi/\Lambda$ and imaginary part represents the wave attenuation.

From Eqn. 4.3 to 4.6, we obtain the following differential equations that $\Phi(r)$ and $\Psi(r)$ must satisfy:

$$\frac{d^2 \Phi}{dr^2} + \frac{1}{r} \frac{d\Phi}{dr} + \left(k_L^2 - \frac{k^2 b^2}{r^2} \right) \Phi = 0 \quad (4.7)$$

$$\frac{d^2 \Psi}{dr^2} + \frac{1}{r} \frac{d\Psi}{dr} + \left(k_S^2 - \frac{k^2 b^2}{r^2} \right) \Psi = 0 \quad (4.8)$$

where $k_L = \omega/\alpha_L$ and $k_S = \omega/\alpha_S$ are complex wavenumbers for the bulk compressional and shear waves.

Eqn. 4.7 and 4.8 are Bessel differential equations whose general solutions are linear superpositions of Bessel functions as expressed below:

$$\Phi(r) = A_1 J_\nu(k_L r) + A_2 Y_\nu(k_L r) \quad (4.9)$$

$$\Psi(r) = A_3 J_\nu(k_S r) + A_4 Y_\nu(k_S r) \quad (4.10)$$

where $A_1, A_2, A_3,$ and A_4 are unknown coefficients, $J_\nu(x)$ and $Y_\nu(x)$ are Bessel functions of the first kind and second kind, and $\nu = kb$ is the order of the Bessel functions.

In cylindrical coordinates, the components of the particle displacement and the stress tensor have the relationships with the scalar and vector potentials as below:

$$u_r = \frac{\partial \phi}{\partial r} + \frac{1}{r} \frac{\partial \psi}{\partial \theta} \quad (4.11)$$

$$u_\theta = \frac{1}{r} \frac{\partial \phi}{\partial \theta} - \frac{\partial \psi}{\partial r} \quad (4.12)$$

$$\sigma_{rr} = (\bar{\lambda} + 2\bar{\mu}) \frac{\partial^2 \phi}{\partial r^2} + \bar{\lambda} \left(\frac{1}{r} \frac{\partial \phi}{\partial r} + \frac{1}{r^2} \frac{\partial^2 \phi}{\partial \theta^2} \right) + 2\bar{\mu} \left(\frac{1}{r} \frac{\partial^2 \psi}{\partial r \partial \theta} - \frac{1}{r^2} \frac{\partial \psi}{\partial \theta} \right) \quad (4.13)$$

$$\sigma_{r\theta} = \bar{\mu} \left(\frac{2}{r} \frac{\partial^2 \phi}{\partial r \partial \theta} - \frac{2}{r^2} \frac{\partial \phi}{\partial \theta} - \frac{\partial^2 \psi}{\partial r^2} + \frac{1}{r} \frac{\partial \psi}{\partial r} + \frac{1}{r^2} \frac{\partial^2 \psi}{\partial \theta^2} \right) \quad (4.14)$$

By substituting Eqn. 4.5 and 4.6 into Eqn. 4.11–4.14, using the expressions for $\Phi(r)$ and $\Psi(r)$ in Eqn. 4.9 and 4.10, the components of the particle displacement and the stress tensor can be expressed in terms of the unknown coefficients and combined as the following matrix set:

$$\begin{bmatrix} u_r \\ u_\theta \\ \sigma_{rr} \\ \sigma_{r\theta} \end{bmatrix} = \begin{bmatrix} D_{11} & D_{12} & D_{13} & D_{14} \\ D_{21} & D_{22} & D_{23} & D_{24} \\ D_{31} & D_{32} & D_{33} & D_{34} \\ D_{41} & D_{42} & D_{43} & D_{44} \end{bmatrix} \begin{bmatrix} A_1 \\ A_2 \\ A_3 \\ A_4 \end{bmatrix} e^{i(kb\theta - \omega t)} \quad (4.15)$$

The details of the matrix elements D_{mn} ($m, n = 1, 2, 3, 4$) in Eqn. 4.15 are listed below:

$$D_{11} = k_L J_\nu^{L'} \quad (4.16)$$

$$D_{12} = k_L Y_\nu^{L'} \quad (4.17)$$

$$D_{13} = i \frac{\nu}{r} J_\nu^S \quad (4.18)$$

$$D_{14} = i \frac{\nu}{r} Y_\nu^S \quad (4.19)$$

$$D_{21} = i \frac{\nu}{r} J_\nu^L \quad (4.20)$$

$$D_{22} = i \frac{\nu}{r} Y_\nu^L \quad (4.21)$$

$$D_{23} = -k_S J_\nu^{S'} \quad (4.22)$$

$$D_{24} = -k_S Y_\nu^{S'} \quad (4.23)$$

$$D_{31} = (\bar{\lambda} + 2\bar{\mu}) k_L^2 J_\nu^{L''} + \bar{\lambda} \frac{1}{r} k_L J_\nu^{L'} - \bar{\lambda} \frac{\nu^2}{r^2} J_\nu^L \quad (4.24)$$

$$D_{32} = (\bar{\lambda} + 2\bar{\mu}) k_L^2 Y_\nu^{L''} + \bar{\lambda} \frac{1}{r} k_L Y_\nu^{L'} - \bar{\lambda} \frac{\nu^2}{r^2} Y_\nu^L \quad (4.25)$$

$$D_{33} = 2i\bar{\mu} \frac{\nu}{r} k_S J_\nu^{S'} - 2i\bar{\mu} \frac{\nu}{r^2} J_\nu^S \quad (4.26)$$

$$D_{34} = 2i\bar{\mu} \frac{\nu}{r} k_S Y_\nu^{S'} - 2i\bar{\mu} \frac{\nu}{r^2} Y_\nu^S \quad (4.27)$$

$$D_{41} = 2i\bar{\mu} \frac{\nu}{r} k_L J_\nu^{L'} - 2i\bar{\mu} \frac{\nu}{r^2} J_\nu^L \quad (4.28)$$

$$D_{42} = 2i\bar{\mu} \frac{\nu}{r} k_L Y_\nu^{L'} - 2i\bar{\mu} \frac{\nu}{r^2} Y_\nu^L \quad (4.29)$$

$$D_{43} = -\bar{\mu} k_S^2 J_\nu^{S''} + \bar{\mu} \frac{1}{r} k_S J_\nu^{S'} - \bar{\mu} \frac{\nu^2}{r^2} J_\nu^S \quad (4.30)$$

$$D_{44} = -\bar{\mu} k_S^2 Y_\nu^{S''} + \bar{\mu} \frac{1}{r} k_S Y_\nu^{S'} - \bar{\mu} \frac{\nu^2}{r^2} Y_\nu^S \quad (4.31)$$

as

$$B_\nu^\beta = B_\nu(k_\beta r), \quad B = J \text{ or } Y, \quad \beta = L \text{ or } S \quad (4.32)$$

and

$$B_\nu^{\beta'} = \frac{d}{d(k_\beta r)} [B_\nu(k_\beta r)], \quad B_\nu^{\beta''} = \frac{d^2}{d(k_\beta r)^2} [B_\nu(k_\beta r)] \quad (4.33)$$

The displacement and pressure in the surrounding water half-space are formulated in terms of a scalar potential function ϕ^W as in Eqn. 3.18. We specifically focused on the solution of the interface waves that are simultaneously coupled in the solid and the water half-space. We formulated this by matching the phase of the scalar potential in the water to that in the solid, such as

$$\phi^W = \Phi^W(r) e^{i(kb\theta - \omega t)} \quad (4.34)$$

where the complex amplitude $\phi^W(r)$ must satisfy the Bessel differential equation

$$\frac{d^2 \Phi^W}{dr^2} + \frac{1}{r} \frac{d\Phi^W}{dr} + \left(k_W^2 - \frac{k^2 b^2}{r^2} \right) \Phi^W = 0 \quad (4.35)$$

that is obtained by substituting Eqn. 4.34 into Eqn. 4.3. In Eqn. 4.35, $k_W = \omega/\alpha_L^W$ is the wavenumber of the compressional wave as $\alpha_L^W = 1481$ m/s is the wave speed in water. Because the water half-space is assumed to be inviscid, α_L^W is a real number without the imaginary part. Moreover, the water half-space has no excitation source, as such, only the partial waves traveling outward in the radial direction exist in the water, and the solution of Eqn. 4.35 is represented by the Hankel function of the first kind, given by

$$\Phi^W(r) = W_0 H_\nu^{(1)}(k_W r) \quad (4.36)$$

where unknown coefficient W_0 will be determined by the boundary conditions at the solid-water interface.

From Eqn. 4.11, 4.13, 4.34, and 4.36, the displacement and the pressure (equivalent to the normal stresses in the solid) along the radial direction in the water half-space are

derived as functions of the unknown coefficient W_0 :

$$u_r^W = \left(k_W H_\nu^{(1)'} \right) W_0 e^{i(kb\theta - \omega t)} \quad (4.37)$$

$$\begin{aligned} p &= \left(\lambda^W k_W^2 H_\nu^{(1)''} + \lambda^W \frac{1}{r} k_W H_\nu^{(1)'} - \lambda^W \frac{\nu^2}{r^2} H_\nu^{(1)} \right) W_0 e^{i(kb\theta - \omega t)} \\ &= P(r) W_0 e^{i(kb\theta - \omega t)} \end{aligned} \quad (4.38)$$

where

$$H_\nu^{(1)} = H_\nu^{(1)}(k_W r), \quad H_\nu^{(1)'} = \frac{d}{d(k_W r)} [H_\nu^{(1)}(k_W r)], \quad H_\nu^{(1)''} = \frac{d^2}{d(k_W r)^2} [H_\nu^{(1)}(k_W r)] \quad (4.39)$$

In Eqn. 4.38, λ^W is the Lamé first parameter for the water half-space that is related to the compressional wave speed α_L^W and the water density ρ^W by $\lambda^W = \rho^W (\alpha_L^W)^2$.

To determine the five unknown coefficients associated with the potential functions in the solid and water, five boundary conditions are required, and this is why the model has a hollowed space in the center so that we can prescribe the inner boundary ($r = a$) to be rigid. As such, the boundary conditions are

- (1) continuity of the displacement along radial direction at the water-sphere interface,

$$u_r|_{r=b} = u_r^W|_{r=b}$$

- (2) continuity of the normal traction in the solid and pressure in the water at the

$$\text{water-solid interface, } \sigma_{rr}|_{r=b} = p|_{r=b}$$

- (3) zero shear traction at the water-solid interface, $\sigma_{r\theta}|_{r=b} = 0$

- (4) zero radial displacement at the inner boundary, $u_r|_{r=a} = 0$

- (5) zero circumferential displacement at the inner boundary, $u_\theta|_{r=a} = 0$

Applying these boundary conditions leads to five equations for the coefficients as shown in the matrix form below:

$$\begin{bmatrix}
D_{11}|_{r=b} & D_{12}|_{r=b} & D_{13}|_{r=b} & D_{14}|_{r=b} & -k_W H_\nu^{(1)'}|_{r=b} \\
D_{31}|_{r=b} & D_{32}|_{r=b} & D_{33}|_{r=b} & D_{34}|_{r=b} & -P(r)|_{r=b} \\
D_{41}|_{r=b} & D_{42}|_{r=b} & D_{43}|_{r=b} & D_{44}|_{r=b} & 0 \\
D_{11}|_{r=a} & D_{12}|_{r=a} & D_{13}|_{r=a} & D_{14}|_{r=a} & 0 \\
D_{21}|_{r=a} & D_{22}|_{r=a} & D_{23}|_{r=a} & D_{24}|_{r=a} & 0
\end{bmatrix}
\begin{bmatrix}
A_1 \\
A_2 \\
A_3 \\
A_4 \\
W_0
\end{bmatrix}
= \mathbf{0} \quad (4.40)$$

or

$$\mathbf{SA} = \mathbf{0} \quad (4.41)$$

which has the same form as Eqn. 3.24 and leads to the characteristic equation in Eqn. 3.25 for non-trivial solutions of unknown coefficients in matrix \mathbf{A} . Solving the characteristic equation yields infinite solution pairs of angular frequency and complex wavenumber (ω, k) that represent the dispersion relation of the plane circumferential interface wave in the water-loaded cylindrical solid. The phase velocity (c) of the interface wave is obtained from the relation between the angular frequency ω and the real part of the complex wavenumber $\text{Re}\{k\} = k^R$, defined by $c = \omega/k^R$.

Note that we can let the hollowed cylindrical model approach to a solid cylinder by assigning a very small value for a . Further discussion regarding the effect of the value a on the circumferential wave can be found in Section 4.2.4.

4.2.2. Numerical Methods for Bessel Functions with Complex Orders

In Eqn. 4.9 and 4.10, the general solutions of the scalar and vector potential functions are linear superpositions of Bessel functions with a complex order $\nu = kb$. A numerical challenge arises with the Bessel functions that have complex orders since they are not supported in MATLAB. To resolve this challenge, this section provides the details of mathematical properties that enable the calculation of approximated values for Bessel functions of this kind.

According to Eqn. (9.1.20) in *Handbook of Mathematical Functions with Formulas, Graphs, and Mathematical Tables* (Abramowitz and Stegun, 10th printing, 1972) [99], the Bessel function of the first kind has the expression:

$$J_\nu(z) = \frac{2 \left(\frac{1}{2}z\right)^\nu}{\sqrt{\pi} \cdot \Gamma\left(\nu + \frac{1}{2}\right)} \int_0^1 (1-t^2)^{\nu-\frac{1}{2}} \cos(zt) dt, \quad \Re(\nu) > -\frac{1}{2} \quad (4.42)$$

where ν and z are the order and the argument, respectively, of the Bessel function J , and $\Gamma(x)$ is the Gamma function.

The recurrence relation given by Eqn. (9.1.27) in [99] can be used to extend the order of the Bessel function to the whole complex plane that is not covered in Eqn. 4.42; that is, for $\Re(\nu) \leq -1/2$, use

$$J_{\nu-1}(z) + J_{\nu+1}(z) = \frac{2\nu}{z} J_\nu(z) \quad (4.43)$$

In addition, the Bessel function of the second kind $Y_\nu(z)$ is also required in our theoretical model, which has the relationship with the first kind given by Eqn. (9.1.2) in [99]:

$$Y_\nu(z) = \frac{J_\nu(z) \cos(\nu\pi) - J_{-\nu}(z)}{\sin(\nu\pi)} \quad (4.44)$$

Note that the Gamma function in Eqn. 4.42 has a complex argument $\nu+1/2$; therefore, the value of Gamma function must be determined through the definition of integral form,

which is Eqn. (6.1.1) in [99]:

$$\Gamma(x) = \int_0^{\infty} t^{x-1} e^{-t} dt, \quad \Re(x) > 0 \quad (4.45)$$

Eqn. 4.45 can be calculated using the Upper Incomplete Gamma Function `igamma` provided in MATLAB function library; however, the calculation speed of this approximation might be slow. An alternative method with enhanced calculation speed to acquire the approximated values of the Gamma function with complex argument can be found in an algorithm library created by Paul Godfrey (<http://my.fit.edu/~gabdo/paulbio.html>).

Similar to the Bessel functions, the recurrence relation of the Gamma function given by Eqn. (6.1.15) in [99] can be used to extend the argument of the Gamma function to the whole complex plane that is not covered in Eqn. 4.45; that is, for $\Re(\nu) \leq 0$, use

$$\Gamma(x + 1) = x\Gamma(x) \quad (4.46)$$

With Eqn. 4.42 to 4.46, the Hankel function of the first kind that represents the waves propagating along the positive r -direction can be obtained by the relationship with the Bessel functions:

$$H_{\nu}^{(1)}(z) = J_{\nu}(z) + iY_{\nu}(z) \quad (4.47)$$

Hence, all required functions are defined.

To validate the two aforementioned approximations of Gamma function—Upper Incomplete Gamma Function `igamma` in MATLAB function library and the program created by Godfrey—Bessel functions $J_{\nu}(z)$ and $Y_{\nu}(z)$ with different complex orders ν and real arguments z were calculated and compared to the values reported in [98] (pp. 148). The comparison is demonstrated in Table 4.1, and the results show both approximations have at least 10 digits of precision compared to the reference.

Table 4.1: Numerical values of Bessel functions $J_\nu(z)$ and $Y_\nu(z)$ calculated by three different algorithms. Red-colored numbers indicate the consistent digits with the reference.

$J_\nu(z)$ with $\nu = 30 + 50i$			
z	Reference	MATLAB <code>igamma</code>	Godfrey
70	$-5.93644837574622 \times 10^{23}$ $-6.21989546226278 \times 10^{23}i$	$-5.93644837574486 \times 10^{23}$ $-6.21989546226806 \times 10^{23}i$	$-5.93644837574481 \times 10^{23}$ $-6.21989546226825 \times 10^{23}i$
31	$9.38713109974277 \times 10^{15}$ $-2.04157148369613 \times 10^{15}i$	$9.38713109974298 \times 10^{15}$ $-2.04157148369613 \times 10^{15}i$	$9.38713109974313 \times 10^{15}$ $-2.04157148369597 \times 10^{15}i$
30	$-1.95359736621662 \times 10^{15}$ $-3.54953866450241 \times 10^{15}i$	$-1.95359736621663 \times 10^{15}$ $-3.54953866450250 \times 10^{15}i$	$-1.95359736621659 \times 10^{15}$ $-3.54953866450258 \times 10^{15}i$
10	-102.750648203869 $+21.6604279770704i$	-102.750648203871 $+21.6604279770701i$	-102.750648203873 $+21.6604279770684i$
$Y_\nu(z)$ with $\nu = 30 + 50i$			
z	Reference	MATLAB <code>igamma</code>	Godfrey
70	$-6.21989546226278 \times 10^{23}$ $+5.93644837574622 \times 10^{23}i$	$-6.21989546226806 \times 10^{23}$ $+5.93644837574486 \times 10^{23}i$	$-6.21989546226825 \times 10^{23}$ $+5.93644837574481 \times 10^{23}i$
31	$-2.04157148369613 \times 10^{15}$ $-9.38713109974277 \times 10^{15}i$	$-2.04157148369613 \times 10^{15}$ $-9.38713109974298 \times 10^{15}i$	$-2.04157148369597 \times 10^{15}$ $-9.38713109974313 \times 10^{15}i$
30	$-3.54953866450241 \times 10^{15}$ $+1.95359736621662 \times 10^{15}i$	$-3.54953866450250 \times 10^{15}$ $+1.95359736621663 \times 10^{15}i$	$-3.54953866450258 \times 10^{15}$ $+1.95359736621659 \times 10^{15}i$
10	21.6604626085221 $+102.750609923256i$	21.6604626098798 $+102.750609922708i$	21.6604626098782 $+102.750609922709i$

4.2.3. Verification of the Numerical Program

The theoretical model presented in Section 4.2.1 was implemented numerically in a commercial software MATLAB (Release R2016b, MathWorks) to calculate the dispersion curves for the circumferential elastic waves. The model was validated against a thin, pure-elastic curved plate with a small thickness to inner radius ratio $(b - a)/a = 0.05$, which has a low curvature and resembles a flat plate. The plate has the same parameters and boundary conditions as those reported by Liu and Qu (1998) [97]: $a = 20$ mm, $b = a/0.95$, $\alpha_L = 5660$ m/s, $\alpha_S = 3200$ m/s, and traction-free boundary conditions at the inner and outer boundaries ($r = a$ and b), which corresponds to four boundary conditions:

- (1) zero normal traction at the inner surface ($r = a$), $\sigma_{rr}|_{r=a} = 0$
- (2) zero normal traction at the outer surface ($r = b$), $\sigma_{rr}|_{r=b} = 0$
- (3) zero shear traction at the inner surface, $\sigma_{r\theta}|_{r=a} = 0$
- (4) zero shear traction at the outer surface, $\sigma_{r\theta}|_{r=b} = 0$

Due to the difference of the boundary conditions, the \mathbf{S} matrix in the characteristic equation for this case becomes

$$\mathbf{S} = \begin{bmatrix} D_{31}|_{r=a} & D_{32}|_{r=a} & D_{33}|_{r=a} & D_{34}|_{r=a} \\ D_{31}|_{r=b} & D_{32}|_{r=b} & D_{33}|_{r=b} & D_{34}|_{r=b} \\ D_{41}|_{r=a} & D_{42}|_{r=a} & D_{43}|_{r=a} & D_{44}|_{r=a} \\ D_{41}|_{r=b} & D_{42}|_{r=b} & D_{43}|_{r=b} & D_{44}|_{r=b} \end{bmatrix} \quad (4.48)$$

The dispersion curves for the thin curved plate were calculated by our MATLAB program, and the results are presented in Fig. 4.2 by plotting the normalized angular frequency $\bar{\omega} = \omega(b-a)/\alpha_S$ against the normalized wavenumber $\bar{k} = k(b-a)$, which is the same as the Fig. 2(c) in [97].

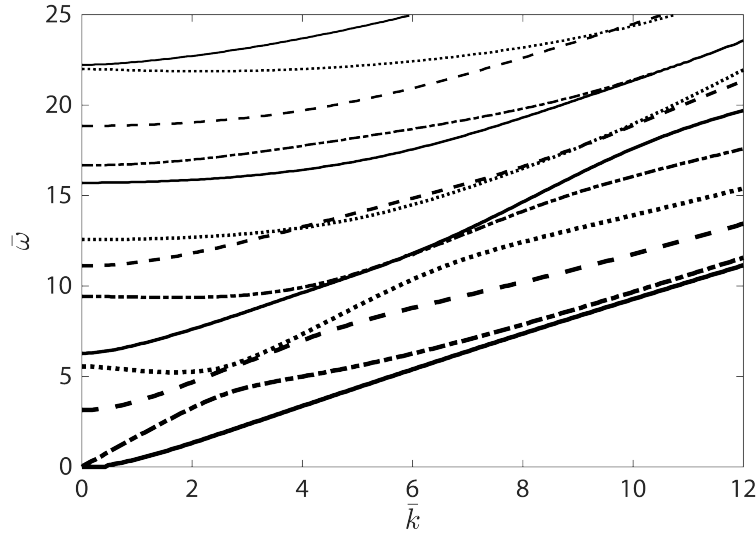


Figure 4.2: Validation of the theoretical model and the numerical calculation. Replicate of dispersion curves from Liu and Qu (1998) [97].

From Fig. 4.2, we observe that the dispersion curves for the thin curved plate resemble the antisymmetric and symmetric guided wave modes in a thin flat plate—(1) the phase velocities of the two lowest modes are strongly frequency-dependent at low frequencies, but become non-dispersive at high frequencies, approaching the Rayleigh wave velocity; (2) the higher order modes originate at cut-off frequencies defined by $\bar{\omega}_c = (\alpha_L/\alpha_S)n\pi$ or $\bar{\omega}_c = n\pi$ ($n = 1, 2, 3, \dots$) for longitudinal or shear thickness resonance modes, respectively. These resemblances, which are expected due to the flatness of the thin curved plate, provide the validation for the circumferential elastic wave model. In addition, the dispersion curves shown in Fig. 4.2 are identical to those calculated by Liu and Qu (1998) [97], which verifies the correctness of our MATLAB program. Note that the axis parameters for Fig. 4.2 were chosen to be the same as those used by Liu and Qu for easy and direct comparison. For the other dispersion curves presented in this paper, the phase velocity is plotted as a function of frequency. The dispersion curve of phase velocity is directly relevant to the OCE measurements and will be used for inverse analysis to quantify the viscoelastic properties.

4.2.4. Model Simulation

The dispersion curve for the lowest order mode is examined to understand the penetration depth of the circumferential interface wave and how its phase velocity is affected by the viscoelastic properties and the outer boundary curvature of the water-loaded model cylinder. The model material was assumed to be a homogeneous, isotropic biofilm with the density $\rho = 1000 \text{ kg/m}^3$, longitudinal wave speed $\alpha_L = 1481 \text{ m/s}$, and shear wave speed $\alpha_S = 2 \text{ m/s}$. ρ and α_L were chosen to be the same as water due to the high ratio of water content (over 90%) in biofilms. The boundary condition of the inner boundary ($r = a$) was assumed to be rigid.

The penetration depth of the circumferential elastic wave is investigated by fixing the outer radius $b = 2$ mm and changing the inner radius a of the cylinder. Fig. 4.3a shows a series of dispersion curves for three different inner radii $a = 0.1$ mm, 0.5 mm and 1 mm. The dispersion curves are plotted with the phase velocity c and frequency f on the ordinate and abscissa axes, respectively, for convenience. All the dispersion curves in the figure originate from higher phase velocities at low frequencies and decrease monotonically with frequency. The differences between the dispersion curves at low frequencies result from the cut-off frequencies of the modes for these cases since the cut-off frequency increases with reduced thickness. The overall decreasing trends of the dispersion curves imply that the penetration depths, which have positive correlation with the wavelengths Λ (determined by $\Lambda = c/f$), also decrease with frequency for these three cases. Take the case $a = 1$ mm for example, below 2700 Hz, the dispersion curve has higher phase velocity than the other two cases since the penetration depth is still larger than or comparable to the thickness between the two boundaries ($b - a = 1$ mm) so that the wave propagates as a guided wave that interacts with both boundaries of the cylinder. Above 2700 Hz, the penetration depth becomes smaller than all three thicknesses considered so that three dispersion curves collapse on top of each other, indicating the wave propagates as an interface wave whose energy is confined near the solid-water interface. At the transition frequency 2700 Hz, we may conclude that the penetration depth of the interface wave is 1 mm, while the wavelength, calculated from the phase velocity 2.75 m/s, is 1.02 mm, which confirms the common rule-of-thumb that the penetration depth of the interface wave is approximately equal to one wavelength. This attribute of the interface wave may be suitable for depth profiling of the viscoelastic properties in a graded sample through the measurements of the frequency-dependent wave speeds.

The calculated dispersion curves for water-loaded pure-elastic and viscoelastic cylinders are compared in Fig. 4.3b. For these calculations, the complex viscosity was changed from $\eta_\mu = 0$ for the pure-elastic case to $\eta_\mu = 0.1$ Pa-s for the viscoelastic case. The inner and outer radii of the cylinder are $a = 0.1$ μm and $b = 2$ mm. For the pure-elastic cylinder, the phase velocity of the interface wave decreases monotonically with frequency. On the other hand, the viscoelastic cylinder has similar decreasing phase velocity at low frequencies but shows a flattened trend from 2500 Hz and a slight increase beyond 3500 Hz. This is because the complex shear modulus of the viscoelastic cylinder increases linearly with frequency by the factor of the shear viscosity as defined in Eqn. 3.3. The increase in the phase velocity of the interface wave at high frequencies is directly related to the viscoelastic properties of the material and will be explored in this chapter to characterize the complex shear moduli of the curved alginate gel samples.

Finally, the influence of the radius of curvature on the phase velocity of the interface wave in the water-loaded viscoelastic cylinder is presented in Fig. 4.3c. Three different outer radii ($b = 1.5$ mm, 2 mm, 2.5 mm) were used in the calculations, while the inner radius was fixed to $a = 0.1$ μm . The shear viscosity is the same as the viscoelastic case in Fig. 4.3b ($\eta_\mu = 0.1$ Pa-s). The dispersion curves in Fig. 4.3c show a clear dependence of the phase velocity on the radius of curvature of the solid-water interface—the phase velocity decreases with the radius of curvature. In addition, all the dispersion curves reach a minimal velocity and increase with frequency, which results from the escalating complex shear modulus with frequency by the factor of shear viscosity as observed in Fig. 4.3b. The results suggest that the curvature of the interface plays an important role in the frequency-dependent phase velocity of the interface wave. We will accommodate the curvature effect in the analyses of the experimental results presented in the next section.

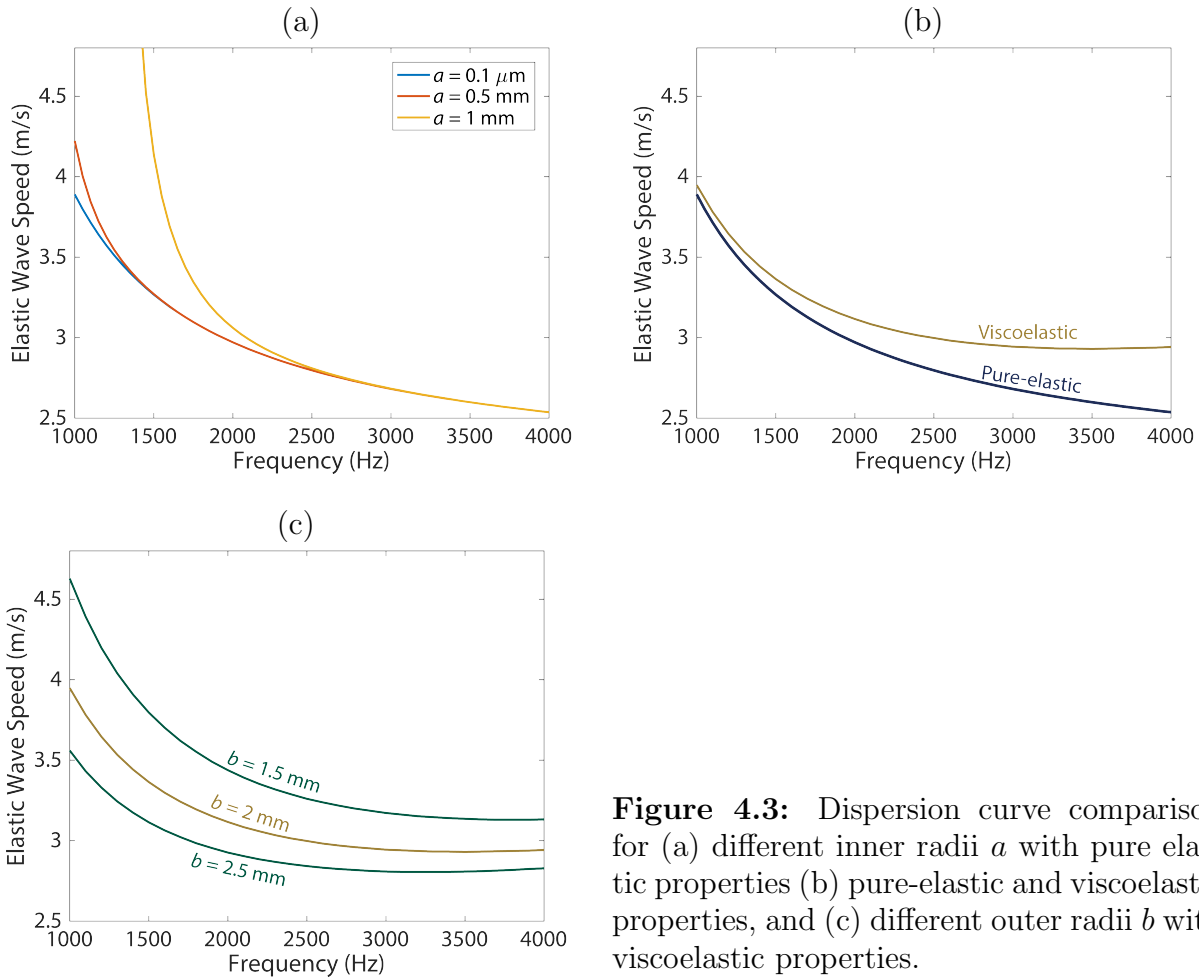


Figure 4.3: Dispersion curve comparison for (a) different inner radii a with pure elastic properties (b) pure-elastic and viscoelastic properties, and (c) different outer radii b with viscoelastic properties.

4.3. Viscoelastic Characterization of Alginate Gel Spheres

4.3.1. Sample Preparation

Spherical alginate (Acros Organics, NJ, USA) samples with 0.8% and 1.2% weight-to-volume (w/v) concentrations were prepared. Mixtures of the two different concentrations were obtained by mixing 0.8 and 1.2 grams of alginate powder, respectively, with a 100 mL solution made from 70 mL of nano-purified water and 30 mL of 5.0% w/v skim milk (Becton, Dickinson and Company 232100, MD, USA). The skim milk was used to increase the optical scattering from the transparent alginate spheres and enhance the OCT image contrast. The alginate solution was stirred in a capped 250 mL Pyrex bottle using a magnetic stir bar with

a stir plate (operated at ~ 400 rpm and heated at 100°C) for one hour. Subsequently, the mixture was removed from the stir plate and held at ambient temperature for ~ 30 minutes to remove entrained air bubbles. Alginate spheres were formed by dripping the mixture into a cross-linking agent made from 25% w/v potassium nitrate and 2% w/v calcium chloride (adapted from Chang and Tseng [100]). The mixture was ejected slowly from a 5 mL Pipet tip held horizontally and 10 cm above the surface of the cross-linking agent. Slow ejection speeds were used to ensure that the weight of the droplet was balanced by surface tension, and the droplet hung near the edge of the Pipet tip. During the ejection process, the size of the droplet increased until a critical volume was reached, and, as the weight exceeded the surface tension, the droplet detached from the Pipet tip and fell into the cross-linking agent. The droplet's spherical shape was formed by surface tension during its free-fall into the cross-linking agent. The spherical droplets solidified in the agent after curing for approximately 30 minutes. OCE experiments were conducted on the cured alginate spheres after 72 hours to ensure that the agent fully diffused through each of them. The process for preparing the alginate spheres is highly repeatable, and the diameters of the spheres fall within the range of 3–5 mm.

4.3.2. OCE Measurements and Inverse Modeling

Fig. 4.4 shows representative OCT and OCE images for a 0.8% alginate sphere with a diameter of 4 mm submerged in water. During the experiments, the height of the water layer was kept at least 2 mm higher than the top of the sphere, so that the effect of the water surface on the circumferential interface waves was negligible. The OCT image shows very limited intensity variation within the sample, indicating structural homogeneity and the integrity (no voids or cracks) of the sample. The local intensity in the OCT image decreases with depth below the sample surface due to attenuation of the OCT light source.

The penetration depth of the OCT light beam depends on the wavelength of the light source and the optical properties of the sample. The OCE image shows periodic oscillation of the optical phase difference $\Delta\phi$ associated with the periodic displacement profile of the elastic wave excited by the actuator at 1600 Hz. The displacement profile follows the curvature of the sample surface, as expected for a circumferential interface wave. The amplitude of the fringes decreases with the circumferential distance from the source due to damping in the viscoelastic solid.

To determine the phase velocity of the circumferential wave, which equals to the product of the excitation frequency and the wavelength, the wavelength was obtained from the fringes in the OCE image by following three steps:

- (1) the contour of the sample surface in the OCT image was identified
- (2) a circular arc was fitted to the contour to determine the approximate radius of curvature and the propagation path (white dotted line in Fig. 4.4b)
- (3) the spatial OCE data along the propagation path was processed by fast Fourier transform to obtain the amplitude spectrum from which the spatial frequency ($1/\bar{\Lambda}$, $\bar{\Lambda}$ is the wavelength) of the wave was determined

For convenience, the curve fitting in step (2) was performed in the cylindrical (r - θ) coordinates system instead of the normal Cartesian (x - y) system so that the wavelength $\bar{\Lambda}$ has the unit of radians rather than meters, and the phase velocity of the interface wave c was calculated using the relationship $c = fb\bar{\Lambda}$ where f is the excitation frequency and b is the radius of curvature.

The measurements of the frequency-dependent elastic wave speed were conducted on alginate spheres with 0.8% and 1.2% alginate concentration. For each concentration, the measurements were repeated on three samples of similar sizes. The experimental results obtained from the six samples are shown in Fig. 4.5. Comparing the overall range of the

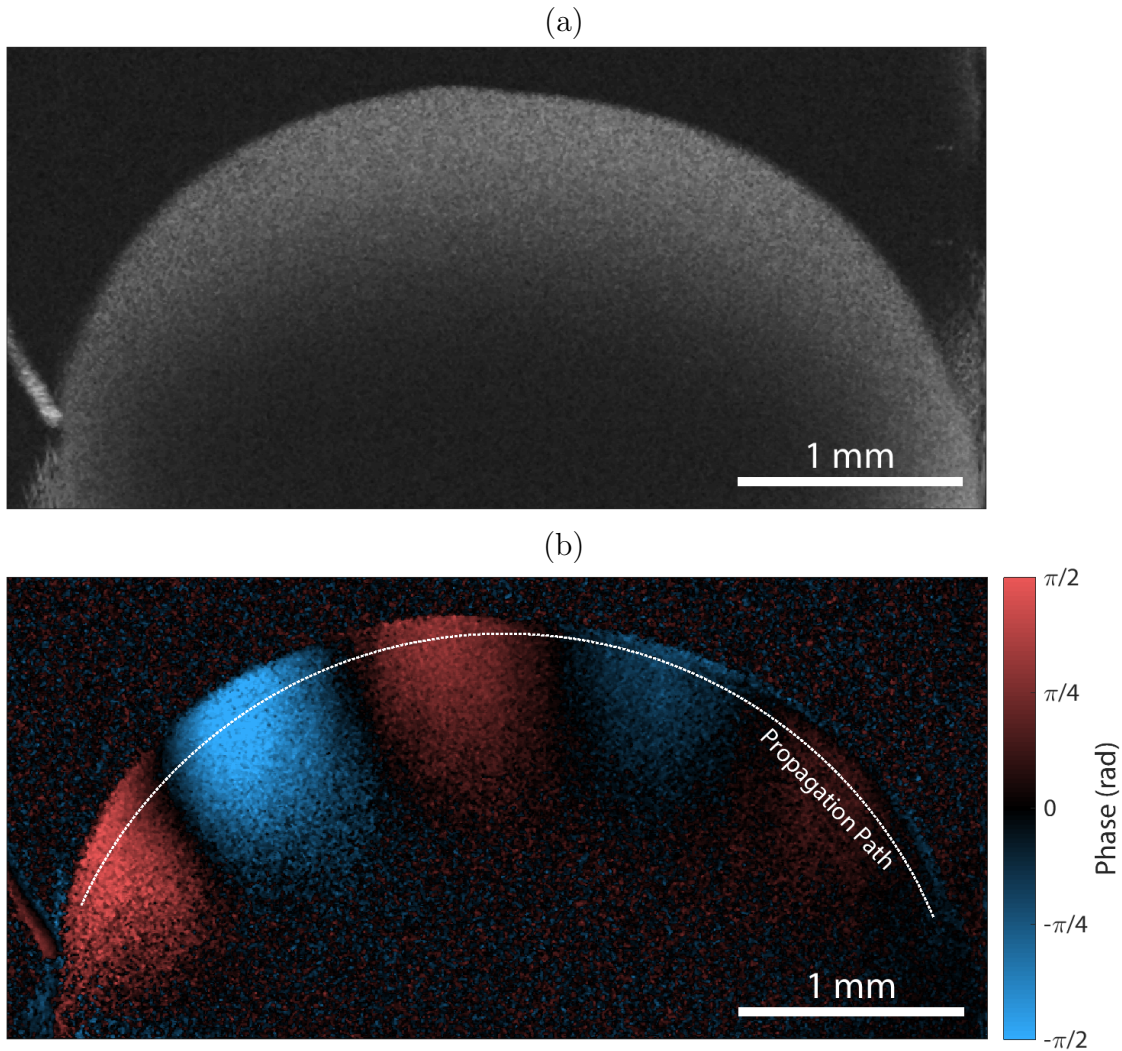


Figure 4.4: (a) OCT image and (b) OCE image showing circumferential interface wave propagation in an alginate gel sphere. An animated GIF file can be found in the supplementary information.

experimentally measured wave speeds from the 0.8% and 1.2% alginate spheres, as expected, the 1.2% alginate spheres yield higher wave speeds. In addition, for all the samples, the wave speeds slightly increase or remain relatively constant at high frequencies. This suggests that the dispersion curves are clearly different from the pure-elastic case, where the phase velocity decreases with frequency, as shown in Fig. 4.3b; therefore, the shear viscosity needs to be

considered when employing the theoretical model to predict the dispersion curves and obtain the best fits for the experimental data.

The best-fit dispersion curves are presented by the solid lines in Fig. 4.5, which show good agreement with the experimental data. The curves were calculated by using the shear modulus and the complex shear viscosity as free fitting parameters in the numerical model. The best-fit viscoelastic properties and other parameters used for calculating the dispersion curves are listed in Table 4.2. The average shear moduli and complex shear viscosities from the measurements on samples with the same concentration are shown in Fig. 4.6a and 4.6b, respectively. For every data point in Fig. 4.6, the circular dot indicates the average of three samples, and the error bar represents the standard deviation. The coefficient of variation (COV), defined by the ratio of the standard deviation to the average value, of each data point is presented in Table 4.3. The COV values suggest small variations of shear moduli and complex shear viscosities from sample to sample with the same alginate concentration, and the stronger sensitivity of the dispersion curves to the shear modulus versus the complex shear viscosity. We remark that the shear moduli are of the same order of magnitude as rheometry estimates [19, 101]. Furthermore, the shear moduli and the complex shear viscosities of the 0.8% samples are within the same order of magnitude of those found in a mixed-culture biofilm as reported in Chapter 3, which verifies a commonly accepted analogy between the alginate and bacterial biofilms in terms of mechanical properties.

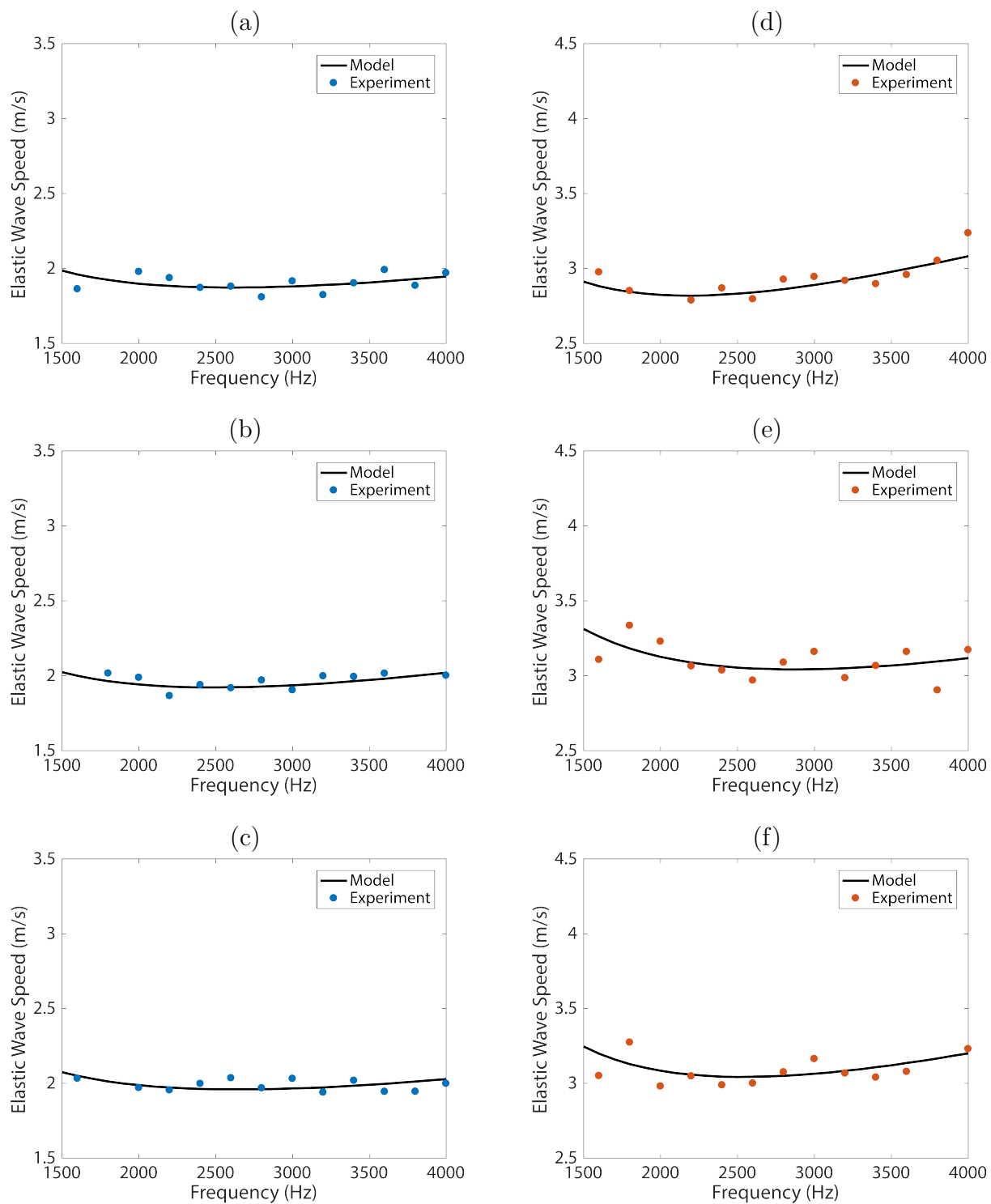


Figure 4.5: Experimentally measured elastic wave speeds in alginate gel samples and the best-fit dispersion curves calculated by the theoretical model. Each figure corresponds to an individual sample with the alginate concentration 0.8% (a–c) and 1.2% (d–f).

Table 4.2: Model inputs and estimated properties for alginate gel samples.

Sample	(a)	(b)	(c)	(d)	(e)	(f)
Alginate concentration (w/v)	0.8%	0.8%	0.8%	1.2%	1.2%	1.2%
Inner radius a (μm)	0.1	0.1	0.1	0.1	0.1	0.1
Outer radius b (mm)	1.84	1.77	2.17	2.18	2.39	2.02
Shear modulus (kPa)	1.69	1.69	1.96	3.10	4.20	3.61
Complex shear viscosity (Pa-s)	0.055	0.06	0.06	0.14	0.13	0.14

The calculations for alginate spheres in Fig. 4.5 were carried out by using a small value for the inner radius a to eliminate the effect from the inner boundary. This inevitably leads to a limitation that the energy carried by the circumferential interface waves must be distributed within the span $[a, b]$. As such, the model is unable to capture low frequency interface waves that have penetration depths longer than or comparable to the radius of the sphere. On the other hand, for high frequency interface waves, this limitation does not hinder the accuracy of the frequency-dependent phase velocity since the penetration depths of the waves at high frequencies are short so that the effect from the inner boundary is negligible. Therefore, the frequency range 1.6–4 kHz was selected for experimental measurements to limit the penetration depths. For example, the wave speed at 1.6 kHz in Fig. 4.5e is 3.11 m/s and the corresponding wavelength is 1.94 mm, which is smaller than the radius of the alginate sphere. In addition, this frequency range provides (1) good signal-to-noise ratio of the OCE images, which deteriorates with frequency due to wave attenuation; (2) sufficient number of fringe cycles in the OCE images to enhance the accuracy of the estimated wavelengths and wave speeds of the circumferential waves. A minimum of three fringe cycles is required to achieve the estimate precision of 0.02 m/s. In the example of Fig. 4.5e mentioned above, the circumference length of ~ 7 mm contains more than three spatial periods of the circumferential wave at 1.6 kHz, which is beyond the requirement of fringe number to reach desired estimate accuracy.

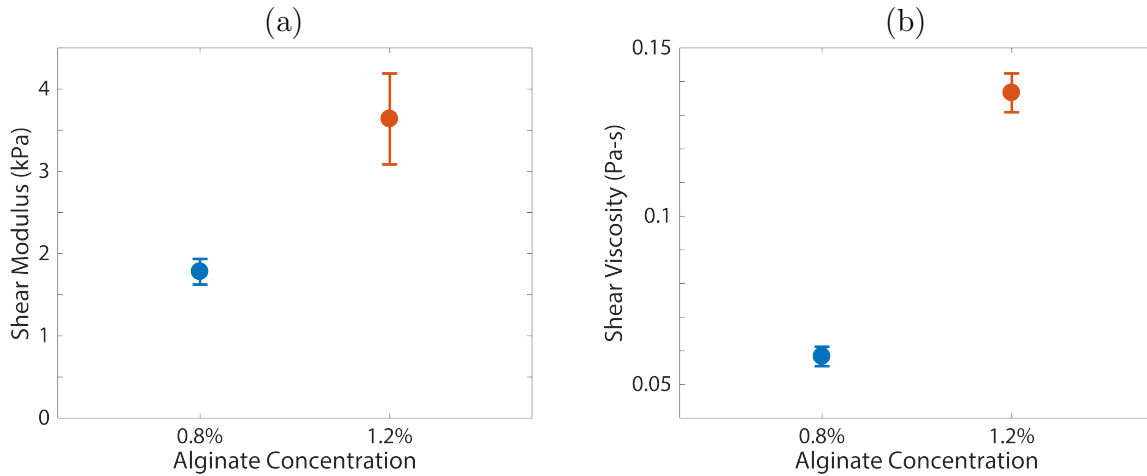


Figure 4.6: Mean values (circles) and standard deviations (error bars) for (a) shear moduli and (b) shear viscosities estimated for alginate gel samples.

Table 4.3: Mean values and variations of shear moduli and shear viscosities for alginate gel samples.

Sample properties		
Alginate concentration (w/v)	0.8%	1.2%
Mean shear modulus (kPa)	1.78	3.64
COV of shear modulus	8.76%	15.2%
Mean complex shear viscosity (Pa-s)	0.058	0.137
COV of complex shear viscosity	4.95%	4.22%

4.4. Concluding Remarks

In this chapter, we developed a metrology approach that combines the OCE measurements with a theoretical model capable of predicting the dispersion relation of circumferential interface waves in soft viscoelastic samples with curved geometries. Although the approach is similar to what was detailed in Chapter 3, the different model geometry—from normal plate to curved cylinder—changed the wave propagation from a Rayleigh/Scholte wave to a circumferential wave, which made the modeling process challenging, especially when accounting for viscoelastic material properties.

The OCE technique was used to obtain the geometry- and frequency-dependent phase velocities of the circumferential interface wave propagating in alginate spheres surrounded by water. The numerical model was based on the elastodynamic wave equation, from which the frequency-dependent phase velocities of elastic waves in a water-loaded curved sample were predicted using the information of sample geometry, material properties, and the boundary conditions. Our numerical calculations suggest that the circumferential interface wave is highly dependent on sample geometry and composition. The numerical model was fitted to the OCE data to estimate the shear moduli and complex shear viscosities of the alginate spheres. This framework was used to characterize the shear moduli and complex shear viscosities of alginate spheres with two different concentrations (0.8% and 1.2% w/v). The estimated properties are in good agreement with reported values in the literature.

The work presented in the chapter laid a solid foundation for modeling the dispersion relation of the circumferential interface waves in curved structures with uniform single composition. We will raise the complexity of this model in the next chapter, adding one more material layer in the cylindrical structure, to more closely approximate the compositional layering and the wave propagation behavior in granular biofilms acquired directly from wastewater processing reactor. This ultimately leads the framework developed in this study to an important application of viscoelastic property characterization on practical biofilm samples.

CHAPTER 5

Mechanical Characterization of Granular Biofilms

The content in this chapter is adapted from a manuscript that will be submitted for publication: **Hong-Cin Liou**, Fabrizio Sabba, Aaron I. Packman, George Wells, and Oluwaseyi Balogun, “Mechanical characterization and local property probing of granular biofilms by optical coherence elastography measurements.”

5.1. Introduction

In Chapter 4, a circumferential interface wave model was presented. The model was used to predict the dispersion relation of the waves traveling along the interface between the water half-space and the curved structures with uniform single composition. The framework combining the model and the OCE measurements of the circumferential interface waves was validated against the alginate gel spheres with two concentrations (0.8% and 1.2% w/v) for estimating their shear moduli and shear viscosities, which shows a good agreement with reported values in the literature.

From literature [7, 8, 17], it is known that granular biofilms have layered structure with different compositions in each layer. In order to more precisely model the wave propagation in granular biofilms, which ultimately leads to a more accurate estimation of granular biofilms’ viscoelastic properties, the circumferential interface wave model presented in the last chapter needs to be modified; otherwise, its single composition assumption would inevitably give rise to errors.

In this chapter, we introduce a modified circumferential interface wave model with one more material layer in the cylindrical structure. In this two-layered model, the layer

thicknesses and the property of each layer need to be considered for calculating the theoretical dispersion curves; therefore, we developed a local wave speed probing approach to acquire the information required by the two-layered model. The local wave speed probing approach was investigated through numerical simulation tool PZFlex and validated against an artificial heterogeneous agarose gel phantom. The approach was then applied to a granular biofilm section for estimating the property contrast between the layers. This property contrast estimation was verified by two kinds of artificial alginate gel spheres that simulate the composition variation in different granular biofilm layers. Finally, all the findings were input into the two-layered model for interpreting the dispersion data recorded by the OCE measurements through inverse modeling, estimating the shear modulus and viscosity of the granular biofilm sample. The framework detailed in this chapter assembles all fundamental components developed in previous chapters and leads to the most valuable and crucial application in this study for characterizing the viscoelastic properties of practical granular biofilms.

5.2. Layered Circumferential Interface Wave Modeling

In this section, we present an analytical model for predicting the frequency-dependent phase velocity of the circumferential waves travelling in a two-layered curved structure. The model will be used to quantitatively estimate the shear modulus and viscosity of the granular biofilms through inverse analysis from the experimental data.

5.2.1. Model Derivation

Fig. 5.1 shows the configuration of the two-layered model which introduces one more material layer compared to the model in Chapter 4 with only single composition. This model adds one

more level of complexity in terms of the composition heterogeneity for modeling. The two-layered model comprises an inner core with the radius $r = a$, an outer layer between $r = a$ and $r = b$, and an inviscid water half-space beyond $r = b$. The water half-space is present to simulate the native aqueous solution where the granular biofilm samples were submerged during the experiments. All materials in this model structure were assumed homogeneous and isotropic.

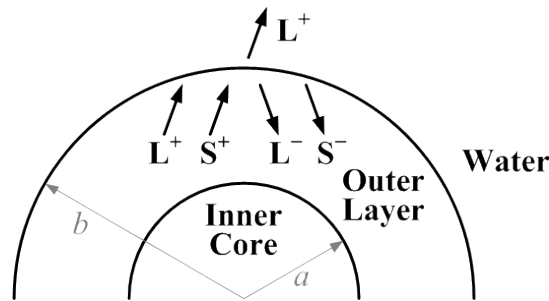


Figure 5.1: Two-layered cylindrical model for circumferential interface wave.

In Chapter 4, we have discussed that the elastic wave travelling along the circumference of the cylinder has frequency-dependent wave speed (the dispersion curve), and the dependency of the wave speed on the frequency is resulted from structure's radius of curvature and material viscosity. In addition, for the two-layered model discussed in this section, if the wavelength of the circumferential wave is larger than or comparable to the thickness of the outer layer, the partial waves—longitudinal and shear waves—propagating outward and inward in the structure would create interference within the layers, yielding guided circumferential wave whose wave speed would also depend on the frequency. Here we present our modeling approach that accounts for these three factors to predict the dispersion curves.

In Chapter 3 and 4, we detailed the derivation steps to obtain the dispersion curves from the governing equation and the Kelvin-Voigt viscoelastic material constitution. These steps include

- (1) solving the governing equation (the elastodynamic wave equation) by using the potential functions associated with the partial waves

- (2) expressing the components of displacements and stresses by the unknown amplitudes and acoustic phases of the partial waves
- (3) applying boundary conditions to obtain characteristic equation
- (4) numerically solving the characteristic equation for the dispersion relation

Although the derivation approach remains the same for the two-layered cylindrical model, there are several differences resulted from the additional layer and material property. The first is the constitutive equations—the complex Lamé constant and shear modulus—defined by Eqn. 3.2 and 3.3. For the complex Lamé constant, since the granular biofilms contain a very high percentage of water content ($> 90\%$), Eqn. 3.2 remains the same and applicable for both the inner core and the outer layer. The complex shear modulus in Eqn. 3.3, however, is different for the two layers, which can be distinguished by

$$\bar{\mu}^A(\omega) = \mu^A + i\eta_\mu^A\omega \quad (5.1)$$

$$\bar{\mu}^B(\omega) = \mu^B + i\eta_\mu^B\omega \quad (5.2)$$

where $\bar{\mu}$ is the complex shear modulus, μ is the shear modulus for a pure-elastic material, η_μ is the shear viscosity, ω is the angular frequency, and the superscripts A and B represent the inner core and the outer layer, respectively.

Due to the additional shear modulus, the longitudinal wave speeds α_L , shear wave speeds α_S , and the associated wavenumbers k_L and k_S for the two layers also need to be defined separately:

$$\alpha_L^A = \sqrt{\frac{\bar{\lambda} + 2\bar{\mu}^A}{\rho}} \quad (5.3)$$

$$\alpha_S^A = \sqrt{\frac{\bar{\mu}^A}{\rho}} \quad (5.4)$$

$$\alpha_L^B = \sqrt{\frac{\bar{\lambda} + 2\bar{\mu}^B}{\rho}} \quad (5.5)$$

$$\alpha_S^B = \sqrt{\frac{\bar{\mu}^B}{\rho}} \quad (5.6)$$

$$k_L^A = \omega/\alpha_L^A \quad (5.7)$$

$$k_S^A = \omega/\alpha_S^A \quad (5.8)$$

$$k_L^B = \omega/\alpha_L^B \quad (5.9)$$

$$k_S^B = \omega/\alpha_S^B \quad (5.10)$$

as $\bar{\lambda}$ is the complex Lamé constant; ρ is the material density, which was assumed to be the same as water (1000 kg/m³) for both layers because of the high percentage of water content in the granular biofilms.

All these differences lead to two matrix sets when expressing the displacement and stress components in each layer separately:

$$\begin{bmatrix} u_r^A \\ u_\theta^A \\ \sigma_{rr}^A \\ \sigma_{r\theta}^A \end{bmatrix} = \mathbf{D}_{4 \times 4}^A \begin{bmatrix} A_1 \\ A_2 \\ A_3 \\ A_4 \end{bmatrix} e^{i(kb\theta - \omega t)} = \begin{bmatrix} D_{11}^A & D_{12}^A & D_{13}^A & D_{14}^A \\ D_{21}^A & D_{22}^A & D_{23}^A & D_{24}^A \\ D_{31}^A & D_{32}^A & D_{33}^A & D_{34}^A \\ D_{41}^A & D_{42}^A & D_{43}^A & D_{44}^A \end{bmatrix} \begin{bmatrix} A_1 \\ A_2 \\ A_3 \\ A_4 \end{bmatrix} e^{i(kb\theta - \omega t)} \quad (5.11)$$

$$\begin{bmatrix} u_r^B \\ u_\theta^B \\ \sigma_{rr}^B \\ \sigma_{r\theta}^B \end{bmatrix} = \mathbf{D}_{4 \times 4}^B \begin{bmatrix} B_1 \\ B_2 \\ B_3 \\ B_4 \end{bmatrix} e^{i(kb\theta - \omega t)} = \begin{bmatrix} D_{11}^B & D_{12}^B & D_{13}^B & D_{14}^B \\ D_{21}^B & D_{22}^B & D_{23}^B & D_{24}^B \\ D_{31}^B & D_{32}^B & D_{33}^B & D_{34}^B \\ D_{41}^B & D_{42}^B & D_{43}^B & D_{44}^B \end{bmatrix} \begin{bmatrix} B_1 \\ B_2 \\ B_3 \\ B_4 \end{bmatrix} e^{i(kb\theta - \omega t)} \quad (5.12)$$

where u_r and u_θ are the displacement along the radial (r) and circumferential (θ) directions, respectively, σ_{rr} is the normal stress, $\sigma_{r\theta}$ is the shear stress, k is the complex wavenumber for the circumferential wave whose real part $k_R = \text{Re}\{k\}$ has the relationship with the

wavelength Λ given by $k_R = 2\pi/\Lambda$, t is the time variable, and A_n and B_n ($n = 1, 2, 3, 4$) are unknown amplitudes of the partial waves in separate layers.

The details of the elements in matrices $\mathbf{D}_{4 \times 4}^A$ and $\mathbf{D}_{4 \times 4}^B$ are listed below:

$$D_{11}^M = k_L^M \frac{d}{d(\xi_L^M)} [J_\nu(\xi_L^M)] \quad (5.13)$$

$$D_{12}^M = k_L^M \frac{d}{d(\xi_L^M)} [Y_\nu(\xi_L^M)] \quad (5.14)$$

$$D_{13}^M = i \frac{\nu}{r} J_\nu(\xi_S^M) \quad (5.15)$$

$$D_{14}^M = i \frac{\nu}{r} Y_\nu(\xi_S^M) \quad (5.16)$$

$$D_{21}^M = i \frac{\nu}{r} J_\nu(\xi_L^M) \quad (5.17)$$

$$D_{22}^M = i \frac{\nu}{r} Y_\nu(\xi_L^M) \quad (5.18)$$

$$D_{23}^M = -k_S^M \frac{d}{d(\xi_S^M)} [J_\nu(\xi_S^M)] \quad (5.19)$$

$$D_{24}^M = -k_S^M \frac{d}{d(\xi_S^M)} [Y_\nu(\xi_S^M)] \quad (5.20)$$

$$D_{31}^M = (\bar{\lambda} + 2\bar{\mu}^M) (k_L^M)^2 \frac{d^2}{d(\xi_L^M)^2} [J_\nu(\xi_L^M)] + \bar{\lambda} \frac{1}{r} k_L^M \frac{d}{d(\xi_L^M)} [J_\nu(\xi_L^M)] - \bar{\lambda} \frac{\nu^2}{r^2} J_\nu(\xi_L^M) \quad (5.21)$$

$$D_{32}^M = (\bar{\lambda} + 2\bar{\mu}^M) (k_L^M)^2 \frac{d^2}{d(\xi_L^M)^2} [Y_\nu(\xi_L^M)] + \bar{\lambda} \frac{1}{r} k_L^M \frac{d}{d(\xi_L^M)} [Y_\nu(\xi_L^M)] - \bar{\lambda} \frac{\nu^2}{r^2} Y_\nu(\xi_L^M) \quad (5.22)$$

$$D_{33}^M = 2i\bar{\mu}^M \frac{\nu}{r} k_S^M \frac{d}{d(\xi_S^M)} [J_\nu(\xi_S^M)] - 2i\bar{\mu}^M \frac{\nu}{r^2} J_\nu(\xi_S^M) \quad (5.23)$$

$$D_{34}^M = 2i\bar{\mu}^M \frac{\nu}{r} k_S^M \frac{d}{d(\xi_S^M)} [Y_\nu(\xi_S^M)] - 2i\bar{\mu}^M \frac{\nu}{r^2} Y_\nu(\xi_S^M) \quad (5.24)$$

$$D_{41}^M = 2i\bar{\mu}^M \frac{\nu}{r} k_L^M \frac{d}{d(\xi_L^M)} [J_\nu(\xi_L^M)] - 2i\bar{\mu}^M \frac{\nu}{r^2} J_\nu(\xi_L^M) \quad (5.25)$$

$$D_{42}^M = 2i\bar{\mu}^M \frac{\nu}{r} k_L^M \frac{d}{d(\xi_L^M)} [Y_\nu(\xi_L^M)] - 2i\bar{\mu}^M \frac{\nu}{r^2} Y_\nu(\xi_L^M) \quad (5.26)$$

$$D_{43}^M = -\bar{\mu}^M (k_S^M)^2 \frac{d^2}{d(\xi_S^M)^2} [J_\nu(\xi_S^M)] + \bar{\mu}^M \frac{1}{r} k_S^M \frac{d}{d(\xi_S^M)} [J_\nu(\xi_S^M)] - \bar{\mu}^M \frac{\nu^2}{r^2} J_\nu(\xi_S^M) \quad (5.27)$$

$$D_{44}^M = -\bar{\mu}^M (k_S^M)^2 \frac{d^2}{d(\xi_S^M)^2} [Y_\nu(\xi_S^M)] + \bar{\mu} \frac{1}{r} k_S^M \frac{d}{d(\xi_S^M)} [Y_\nu(\xi_S^M)] - \bar{\mu} \frac{\nu^2}{r^2} Y_\nu(\xi_S^M) \quad (5.28)$$

where

$$\nu = kb, \quad \xi_\beta^M = k_\beta^M r, \quad M = A \text{ or } B, \quad \beta = L \text{ or } S \quad (5.29)$$

The additional material layer increases the number of the unknown amplitudes to nine in total, including the W_0 in Eqn. 4.40 that is associated with the potential function in the water half-space. This means nine boundary conditions are required to determine all unknown amplitudes. There are seven continuity conditions that automatically exist in the structure, which are

(1) continuity of the displacement along the radial direction at the layer interface,

$$u_r^A|_{r=a} = u_r^B|_{r=a}$$

(2) continuity of the displacement along the tangential direction at the layer interface,

$$u_\theta^A|_{r=a} = u_\theta^B|_{r=a}$$

(3) continuity of the normal stress at the layer interface, $\sigma_{rr}^A|_{r=a} = \sigma_{rr}^B|_{r=a}$

(4) continuity of the shear stress at the layer interface, $\sigma_{r\theta}^A|_{r=a} = \sigma_{r\theta}^B|_{r=a}$

(5) continuity of the displacement along the radial direction at the water interface,

$$u_r^B|_{r=b} = u_r^W|_{r=b}$$

(6) continuity of the normal traction in the outer layer and the pressure in the water

$$\text{at the water interface, } \sigma_{rr}^B|_{r=b} = p|_{r=b}$$

(7) the shear traction in the outer layer vanishes at the water interface, $\sigma_{r\theta}^B|_{r=b} = 0$

To meet the mathematical requirement of solving for the nine unknowns, the model configuration was modified to add two more boundary conditions. As shown in Fig. 5.2, a tiny hole with an infinitesimal radius $r = e$ is introduced at the center of the cylinder. The presence of this hole, assuming a rigid condition on the hole boundary, creates two more boundary conditions:

(8) zero radial displacement at the hole boundary, $u_r^A|_{r=e} = 0$

(9) zero circumferential displacement at the hole boundary, $u_\theta^A|_{r=e} = 0$

These boundary conditions lead to nine equations for the unknown amplitudes, which can be combined in the matrix form as follow:

$$\begin{bmatrix} D_{11}^A|_{r=a} & D_{12}^A|_{r=a} & D_{13}^A|_{r=a} & D_{14}^A|_{r=a} & -D_{11}^B|_{r=a} & -D_{12}^B|_{r=a} & -D_{13}^B|_{r=a} & -D_{14}^B|_{r=a} & 0 \\ D_{21}^A|_{r=a} & D_{22}^A|_{r=a} & D_{23}^A|_{r=a} & D_{24}^A|_{r=a} & -D_{21}^B|_{r=a} & -D_{22}^B|_{r=a} & -D_{23}^B|_{r=a} & -D_{24}^B|_{r=a} & 0 \\ D_{31}^A|_{r=a} & D_{32}^A|_{r=a} & D_{33}^A|_{r=a} & D_{34}^A|_{r=a} & -D_{31}^B|_{r=a} & -D_{32}^B|_{r=a} & -D_{33}^B|_{r=a} & -D_{34}^B|_{r=a} & 0 \\ D_{41}^A|_{r=a} & D_{42}^A|_{r=a} & D_{43}^A|_{r=a} & D_{44}^A|_{r=a} & -D_{41}^B|_{r=a} & -D_{42}^B|_{r=a} & -D_{43}^B|_{r=a} & -D_{44}^B|_{r=a} & 0 \\ 0 & 0 & 0 & 0 & D_{11}^B|_{r=b} & D_{12}^B|_{r=b} & D_{13}^B|_{r=b} & D_{14}^B|_{r=b} & -k_W H_\nu^{(1)'}|_{r=b} \\ 0 & 0 & 0 & 0 & D_{31}^B|_{r=b} & D_{32}^B|_{r=b} & D_{33}^B|_{r=b} & D_{34}^B|_{r=b} & -P(r)|_{r=b} \\ 0 & 0 & 0 & 0 & D_{41}^B|_{r=b} & D_{42}^B|_{r=b} & D_{43}^B|_{r=b} & D_{44}^B|_{r=b} & 0 \\ D_{11}^A|_{r=e} & D_{12}^A|_{r=e} & D_{13}^A|_{r=e} & D_{14}^A|_{r=e} & 0 & 0 & 0 & 0 & 0 \\ D_{21}^A|_{r=e} & D_{22}^A|_{r=e} & D_{23}^A|_{r=e} & D_{24}^A|_{r=e} & 0 & 0 & 0 & 0 & 0 \end{bmatrix} \begin{bmatrix} A_1 \\ A_2 \\ A_3 \\ A_4 \\ B_1 \\ B_2 \\ B_3 \\ B_4 \\ W_0 \end{bmatrix} = \mathbf{0} \quad (5.30)$$

or

$$\mathbf{SA} = \mathbf{0} \quad (5.31)$$

where k_W is the compressional wavenumber in the water half-space, and the details of $H_\nu^{(1)'}$ and $P(r)$ are provided in Eqn. 4.38 and 4.39. Eqn. 5.31 has the same form as Eqn. 3.24 and 4.41, leading to the characteristic equation in Eqn. 3.25 for non-trivial solutions of unknown coefficients in matrix \mathbf{A} . The dispersion relation of the circumferential interface wave in the two-layered cylindrical structure is obtained using the same procedure in Chapter 4.

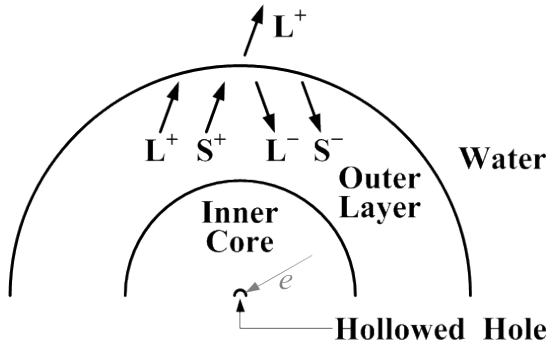


Figure 5.2: Modified two-layered cylindrical model.

5.2.2. Model Simulation

For circumferential waves travel in the two-layered cylindrical model, three important factors will influence the wave propagation. These factors are

- (1) the radius of curvature of the sample surface
- (2) the radius ratio of the two layers
- (3) the property contrast between the two layers

Since the effect resulted from the factor (1) had been discussed in Chapter 4, we will focus on exploring factors (2) and (3) in this section by assigning (a) a fixed radius of curvature for the surface of the cylindrical model ($b = 2$ mm) and (b) a fixed material property for the outer layer to investigate how the radius ratio and the property contrast of the two layers affect the frequency-dependent wave speed of the circumferential wave. The material properties used for the outer layer are density $\rho = 1000$ kg/m³, longitudinal wave speed $\alpha_L^B = 1480$ m/s, and shear wave speed $\alpha_S^B = 2$ m/s. The density and longitudinal wave speed were chosen to be the same as water due to the high ratio of water content in the biofilms, which also applies to those of the inner core. Note that we only used pure-elastic properties without considering the viscosity in this investigation. The radius e for the tiny hole at the center was chosen to be 1 μ m, which is much smaller than other characteristic lengths in the structure, to eliminate its effect.

Fig. 5.3 shows seven dispersion curves of the lowest order modes calculated by fixing the material properties of the inner core and changing the radius a . The properties used for the inner core are density $\rho = 1000$ kg/m³, longitudinal wave speed $\alpha_L^A = 1480$ m/s, and shear wave speed $\alpha_S^A = 1$ m/s. The curves at the top and the bottom correspond to the extreme cases where the structure only has single composition with the properties of the outer layer or inner core, respectively. The rest of the curves corresponds to different a as indicated.

All the dispersion curves in the figure share the similar trend where their phase velocities are higher at low frequencies and decrease monotonically with frequency. The difference between the dispersion curves at low frequencies results from the cut-off frequencies of the modes for these cases since the cut-off frequency is dependent on the layer thickness and the material property. Another distinct difference of the curves is that the wave speed decreases with the size of the inner core. However, the four dispersion curves from the top ($a \leq 1$ mm) converge to each other at the high frequency range (≥ 3000 Hz), and the reason for these four curves to be different from the other three is the penetration depth of the circumferential wave. It is known from Chapter 4 that the circumferential wave has a certain penetration depth that is approximately equal to the wavelength. At 3000 Hz, the wave speed of the top four curves converges to 2.68 m/s, leading to the wavelength (and the penetration depth) of 0.89 mm which is comparable but smaller than the thickness of the outer layer. Therefore, above this frequency, the circumferential wave only has very limited interaction with the interface ($r = a$) and the appearance of the inner core does not affect the circumferential wave propagation. At frequencies below 3000 Hz, the convergence occurs faster for the $a = 0.5$ mm and 0.75 mm cases than the $a = 1$ mm one because the penetration depth for the former two becomes smaller than the outer layer thickness at lower frequencies.

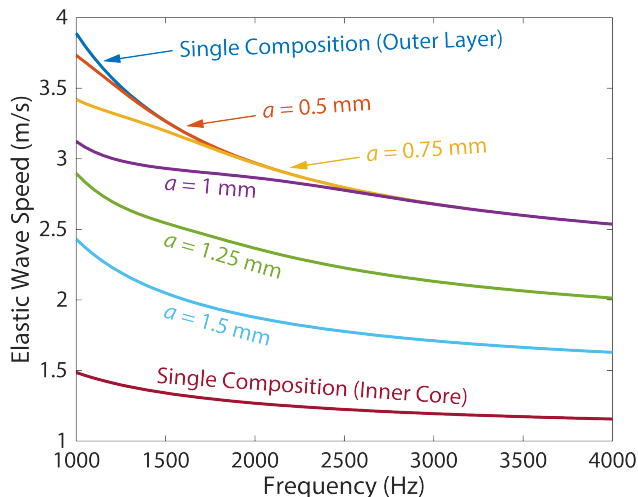


Figure 5.3: Comparison of dispersion curves for different inner core sizes.

On the other hand, when the inner core size is above $a = 1.25$ mm, its influence on the circumferential wave propagation is intrinsic across the frequency range of interest. The wave speed further decreases with the inner core size and approaches the limit where the whole structure comprises only one single composition of the inner core.

Fig. 5.4 shows three dispersion curves of the lowest order modes calculated by fixing the size of the inner core ($a = 1$ mm) but changing its shear wave speed from 1 m/s, 2 m/s, to 4 m/s. Note that the purple and blue curves in Fig. 5.4 have the same geometry, compositions, and material properties as those two in Fig. 5.3. For the blue curve, the shear wave speeds of both layers are equally 2 m/s, which reduces the composition to only one that belongs to the outer layer. Because of the penetration depth of the circumferential wave, the three curves converge to the same curve at 3000 Hz. In addition, at the frequency range below 3000 Hz, the wave speed is dependent on the material property of the inner core—the speed is higher when the inner core has a higher shear wave speed. All these observations suggest that the outer layer thickness, the penetration depth, and the contrast of the material properties between the two layers are crucial factors for the circumferential wave propagation in this layered structure.

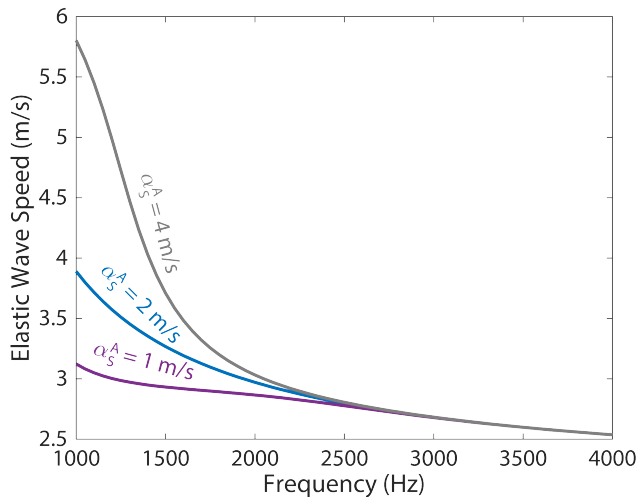


Figure 5.4: Comparison of dispersion curves for different shear wave speeds of the inner core.

5.3. Local Wave Speed Probing

The two-layered model gives rise to the need to acquire the information about the property contrast of the two layers when applying the model to predict theoretical dispersion curves and estimate the viscoelastic properties of granular biofilms. To address the need, we developed a new approach to estimate the local elastic wave speed from OCE measurements, which would provide the required information for the model input. In this section, we first used a numerical simulation tool to investigate the resolution of this new approach. Then, we applied this approach on an artificial agarose gel phantom which has a layered structure that represents the property heterogeneity. Finally, we used this approach on a granular biofilm section to estimate the property contrast along the depth. The estimated values will be validated in Section 5.4 and used in the inverse modeling for the viscoelastic characterization of granular biofilms.

5.3.1. Numerical Simulation

The purpose of the numerical simulations is to demonstrate the approach of probing local wave speed and investigate its spatial resolution. The simulations were conducted in a finite element analysis software PZFlex (Release 2015, now OnScale). The software solves the linear elastodynamic equation numerically to calculate the full-field dynamic responses along with the time steps in the given model region. Fig. 5.5 shows the configuration of the numerical model. The plane-strain assumption was applied to this two-dimensional model to simulate the plane wave source we used in the experiments. The width and height of the model are both 20 mm. The boundary conditions are traction-free at the top, symmetric on the left, and absorbing on the right and at the bottom. The symmetric boundary condition was used to reduce the size of the model and the absorbing ones were used to eliminate the reflections of the waves when they arrive at the boundaries. In this model setting, we may

treat the simulation box as a semi-infinite medium by ignoring the numerical noise occurring at the absorbing boundaries. The source of the waves indicated by the red arrow in Fig. 5.5 was applied to the top-left corner of the model box. The source has an infinitesimal width along the x -direction and the time history of its amplitude is a continuous single-frequency sinusoidal signal, which altogether leads to an ideal harmonic line source. We used three different frequencies (1 kHz, 2.1 kHz, and 4 kHz) in this section. Since the simulation box is semi-infinite, upon excitation from the source, bulk longitudinal, bulk shear, and surface waves are generated. The model is composed of two material regions with a tilted interface between them. Both regions have the same density (1000 kg/m^3) and longitudinal wave speed (158.5 m/s). The density was chosen to be the same as water since all samples in this study contain very high ratio of water content ($> 90\%$), and the longitudinal wave speed was chosen to reduce the calculation time compared to that of water (1480 m/s) yet still keep a good approximation for the Poisson's ratio of soft materials ($\nu = 0.5$). The only difference of the two regions in the simulation box is the shear wave speeds where the left has 2 m/s and the right has 3.5 m/s , which corresponds to 1.91 m/s and 3.34 m/s for the Rayleigh wave speeds in the two regions, respectively. The tilted interface was designed to simulate a more gradual change in composition along the wave propagation path—which is expected in most practical biofilms—compared to an upright interface. The vertical component of the local particle velocity on the surface were recorded at different time steps, and the results were plotted as acoustic B-scans (Fig. 5.6a, 5.6c, and 5.6e).

In Fig. 5.6a, 5.6c, and 5.6e, the horizontal axis represents the space along the lateral (x) direction and the vertical axis represents the time. The colormap varying from blue, black, and yellow was used to present the contour of local vertical velocity, where these three colors correspond to the minimum, zero, and the maximum, respectively. As the continuous elastic wave travels with time, the wave phases propagate away from the source toward the

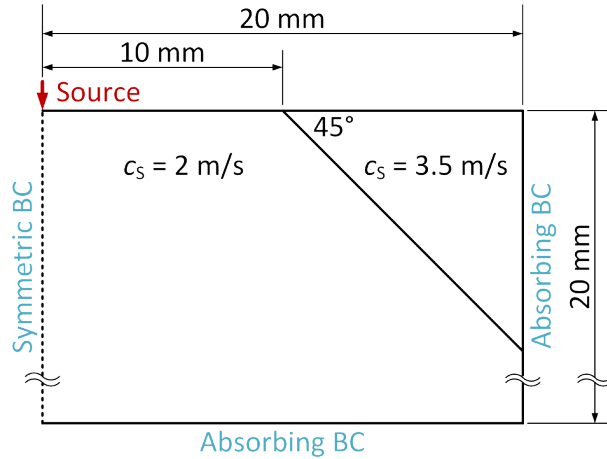


Figure 5.5: Model configuration of the numerical simulation.

positive x -direction, leading to the tilted fringes aligned in the acoustic B-scans. The angles of the tilted fringes depend on how fast the wave moves; therefore, the local wave speeds can be estimated from the local slopes of the fringes.

We chose to trace the wave phases by locating where the local vertical velocities are zero and marked the locations with white circular dots as shown in the B-scans. The local slopes were estimated by the linear regression of every five adjacent white dots on the same track, and the center of the five was used to represent the location of the estimated local wave speed. The results are presented in Fig. 5.6b, 5.6d, and 5.6f for the three frequencies, respectively. In these three figures, the local wave speeds share common trends in different regions:

- (1) they are lower in the left region and higher in the right
- (2) they show slight fluctuation in the region that is close to the source
- (3) they reach a relatively stable region between the source and the interface
- (4) before the interface, they have another region showing little fluctuation due to the reflection from the interface
- (5) after the interface, they rise due to the material property change
- (6) they approach and maintain at the higher value

The fluctuation ranges of the wave speed are 1.214 m/s, 1.175 m/s, and 1.175 m/s in region (2) for 1 kHz, 2.1 kHz, and 4 kHz, respectively, and those in region (4) are 0.339 m/s, 0.289 m/s, and 0.293 m/s. The fluctuation is larger for 1 kHz and indistinguishable between 2.1 kHz and 4 kHz. The fluctuation ranges in region (2) are larger than in region (4) since there is more coupling from the shear wave to the surface wave near the source. The coupling from the longitudinal wave can be ignored here since the simulation only monitor the local vertical velocity on the surface, but the particle movement induced by the longitudinal wave would only be horizontal. In addition, since the interference is caused by the shear wave, the width of the fluctuation region is dependent on the shear wavelength, resulting in a longer zone for the lower frequencies.

Beyond the differences in region (2) and (4), we remark that the length of the wave speed transition in (5) is very important in this study since this length represents the resolution of this approach to probe the local property change. In the ideal case where the resolution is infinitesimal, the wave speed variation would be a step function at the interface. However, the simulation shows that the wave speed has a buffering zone with a certain length where the wave speed gradually approaches the higher value after the interface. As such, we apply a buffering function to quantify the length of the transition zone and use the length constant to represent the mechanical resolution of this local property probing approach.

The buffering function is an analogy to the voltage retardation in an RC circuit when subjected to a step input, which is defined for the local wave speed c as

$$c = \begin{cases} c_1, & x < x_0 = 10 \text{ mm} \\ c_2 - (c_2 - c_1)e^{-(x-x_0)/L}, & x \geq x_0 = 10 \text{ mm} \end{cases} \quad (5.32)$$

where c_1 is the surface wave speed before the interface and c_2 is that after; x is the lateral position; L is the length constant which corresponds to the distance for the wave speed to gain 63.2% of the wave speed difference ($c_2 - c_1$). By fitting the buffering function to Fig. 5.6b, 5.6d, and 5.6f as indicated by the orange curves, the length constants of the three frequencies were obtained and plotted in Fig. 5.7 along with the surface wavelengths of the left and right regions (Λ_1 and Λ_2 , respectively) for comparison. The inset of Fig. 5.7 shows the ratios of the length constants referenced to the wavelengths in the left and right region (L/Λ_1 and L/Λ_2 , respectively). The inset shows that the ratio L/Λ_1 equals to 60.7% and L/Λ_2 equals to 34.7% in average. This result provides a quantitative scaling value of the mechanical resolution for the approach of local property probing, which is $\sim 60\%$ of the elastic wavelength.

5.3.2. Local Wave Speed Probing on a Layered Agarose Gel Phantom

To validate the approach of estimating the local wave speed by tracking acoustic phase movement, we applied this approach on an artificial soft hydrogel sample with spatial material property variation. The hydrogel sample is composed of three layers along the lateral direction as shown in Fig. 5.8a. Each layer was made from agarose gel with different agarose concentrations—1.0% w/v, 1.25% w/v, and 1.5% w/v—from left to right, respectively. In the lateral direction (x -direction) of Fig. 5.8a, the middle layer has 2 mm of width and the widths of the other two layers are over 10 mm. In the out-of-plane direction (y -direction) and the vertical direction (z -direction), the thickness and the height of the sample are 30 mm and 10 mm, respectively.

The layered agarose sample were made by pouring heated agarose solution in a mold with the sequence from 1.5%, 1.25% to 1.0% of agarose concentrations. The solutions were prepared following the protocol detailed in Chapter 3. The boiled solution of the first layer

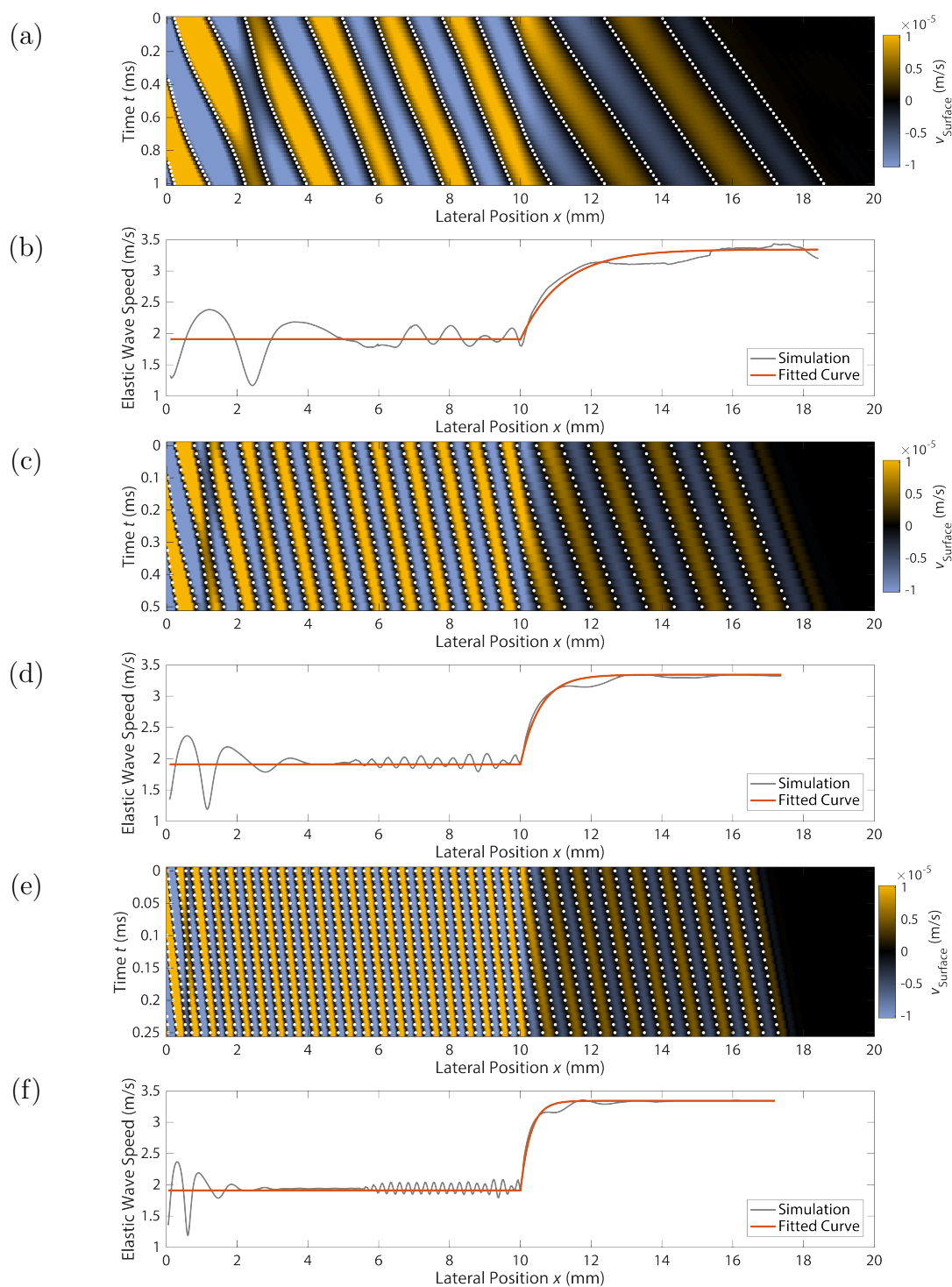


Figure 5.6: (a), (c), and (e) Acoustic B-scans for the surface wave propagation in numerical simulations. (b), (d), and (f) Local wave speed estimation from the acoustic B-scans. Excitation frequency = 1 kHz (a and b), 2.1 kHz (c and d), and 4 kHz (e and f).

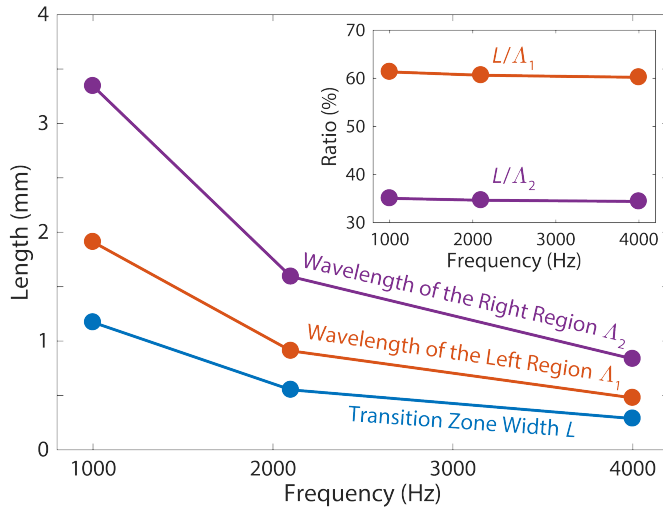


Figure 5.7: Mechanical resolution (L) of the local wave speed probing approach and the comparison to the wavelengths in the left and right regions (Λ_1 and Λ_2 , respectively). The inset shows the ratio of L/Λ_1 and L/Λ_2 .

(1.5%) was poured in the mold and sat still in the ambient temperature (22°C) for 20 minutes to cool down and solidify. The solution of the second layer (1.25%) was then poured on top of the first layer right after it was boiled in the microwave oven. The temperature of the solution was still over 90°C so that it would melt the top region of the first layer and formed a strong bondage at the interface between the two layers. After waiting for another 20 minutes for the second layer to cool down and solidify in the ambient temperature, the third layer was made by repeating the same procedure for the second layer. The interfaces observed in Fig. 5.8a are not perpendicular to the sample surface due to the surface tension between the agarose solution and the mold wall. These angled interfaces share the same advantage stated in the previous section that they created a gradual property change along the propagation path of the elastic waves, which is a good approximation of the property variation in real biofilms.

We excited and recorded the single-frequency (2.1 kHz) continuous wave propagation in the agarose sample. The razor blade was placed at the left in Fig. 5.8a. The blade edge is parallel to the y -direction to serve as a line source generating the elastic waves. The sample was slightly tilted to avoid normal incident of the OCT laser light toward the sample surface, which would reflect too much light back into the OCT objective and create artifact

and noise in the OCT image. The dark fringes close to the source in Fig. 5.8a are due to large amplitudes of the local displacement. The large displacement causes the optical phase difference $\Delta\phi$ resolved by the interferometer in the OCT to return to zero due to phase wrapping. These artifacts only appear within the region close to the source and gradually decay with distance since the wave amplitude attenuates when traveling.

The OCE image is shown in Fig. 5.8b. 21 OCE images were recorded at different time delays t from $t = 0$ to 0.5 ms. Note that within the 4 mm region from the left in Fig. 5.8b, the fringes have more alteration than the region beyond 4 mm, but some of the alteration is not due to the polarity of the local displacement. For example, as indicated by the white arrows in Fig. 5.8b, both the red region and the surrounding blue fringe should have the same displacement polarity (downward displacement). However, when large displacement amplitudes occur and cause the optical phase difference to go over the $[-\pi, \pi]$ limit in the OCT interferometry, the phase wrapping phenomenon would appear and flip the sign of the optical phase, changing the color from blue to red. Since the displacement amplitudes are larger in the region close to the source, the phase wrapping is more phenomenal before $x = 4$ mm, while no phase wrapping is observed in the right half of Fig. 5.8b.

The acoustic phase values—the values represented by the red-blue color contour in OCE images—were extracted along the wave path indicated by the white dotted line in Fig. 5.8b. These values from different time delays were stacked in different rows to create an acoustic B-scan as shown in Fig. 5.8c, and the local wave speed can be estimated by calculating the local slopes of the tilted fringes, same as the approach used in the previous section. When identifying the locations of zero local displacements for local wave speed estimation, the beginning and the end points of the tracks were manually located to avoid those phase-wrapped regions. The tracks are indicated by the white circular dots in Fig. 5.8c. The estimation results are shown in Fig. 5.8d with two orange dashed lines indicating the

cross points of the wave path and the interfaces in Fig. 5.8a (marked by the orange arrows). Fig. 5.8d clearly shows the local wave speed increases from layer to layer with increasing agarose concentration, and the start points of the wave speed jumps are perfectly consistent with the layer interfaces (orange dashed lines). This experimental result validates that this approach is capable of resolving the property variation in the sample along the direction of wave propagation, which may provide necessary information required by the two-layered theoretical model to estimate the viscoelasticity of the granular biofilms with radially varying properties.

5.3.3. Local Wave Speed Probing on a Granular Biofilm Section

In the theoretical model section (Section 5.2), we stated that three important factors will influence the wave propagation in the two-layered cylindrical structure, namely, (1) the radius of curvature of the sample surface, (2) the radius ratio of the two layers, and (3) the property contrast between the two layers. Although the radius of curvature can be estimated nondestructively by the OCT image, the information of the rest two factors can only be acquired by testing the sections of granular biofilms. In this section, we used the normal camera image from the OCT microscope to estimate the size ratio of the outer layer and the inner core in a granular biofilm from a sectioned granular biofilm. Then, we used the approach detailed in previous sections to probe local elastic property, resolving the property change along the radial direction of the biofilm sample.

The granular biofilm tested in this section was obtained from a full-scale AquaNereda Aerobic Granular Sludge (AGS) Reactor (Aqua-Aerobic Systems, Inc., Rockford, IL, USA). Fig. 5.9a shows the camera image of the granular biofilm section captured by the OCT microscope. The granular biofilm section was cut to have a thickness of approximately 1 mm. The red arrow is the scanning path of the OCT and OCE images in Fig. 5.9b and 5.9c.

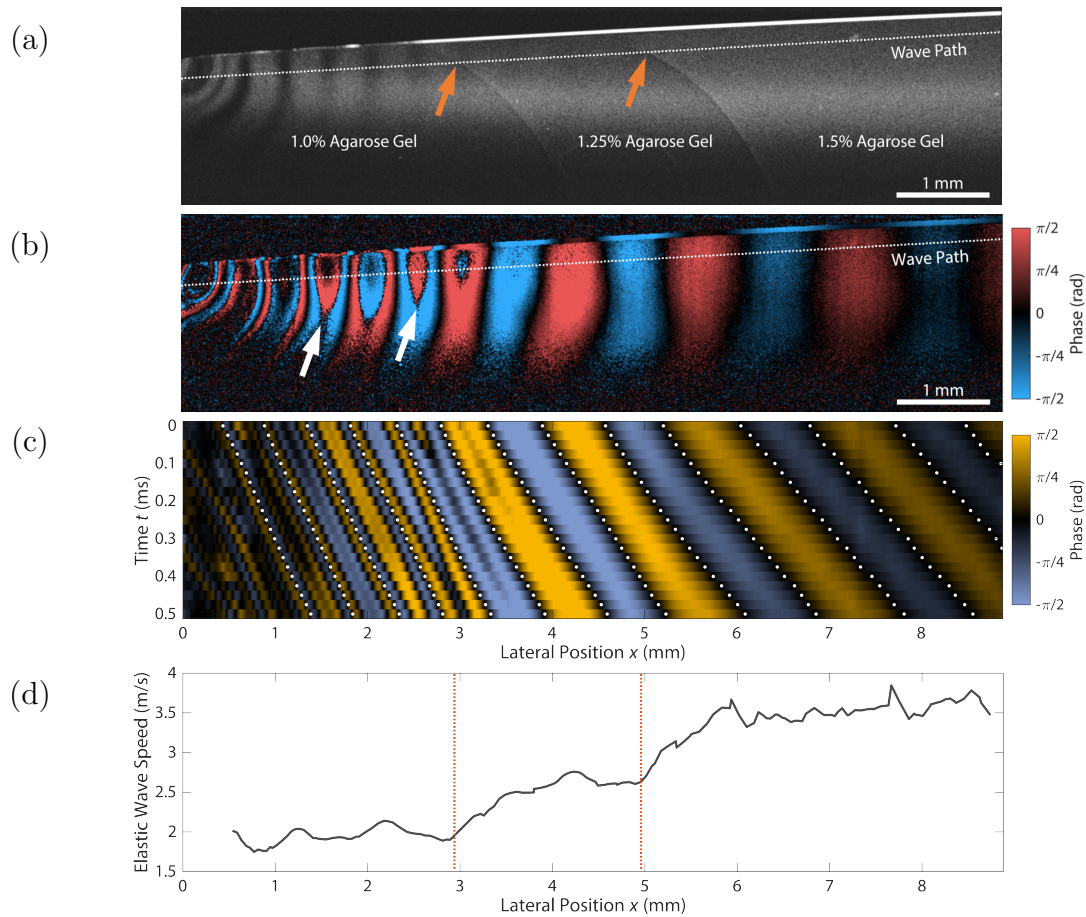


Figure 5.8: Measurement of local wave speed probing on the layered agarose gel phantom. (a) OCT image showing the three layers. (b) OCE image recorded at 2.1 kHz showing the distribution of optical phase difference $\Delta\phi$. (c) Acoustic B-scan created by extracting $\Delta\phi$ from the white dashed line in (b) at different time delay. (d) Local wave speed estimated from the local slopes of the white dotted tracks in (c).

A distinct boundary is present in Fig. 5.9a to separate the outer layer and the inner core, and the radius of the inner core is approximately 50% of the total sphere radius. The orange dashed lines in Fig. 5.9a serve as spatial markers of the locations where the scanning path (red arrow) intersects with the layer boundary and the sphere center. Note that the layer boundary is not seen in the OCT image (Fig. 5.9b). Since the gray-scale intensity in an OCT image is corresponding to the refractive index contrast in the sample, we may conclude

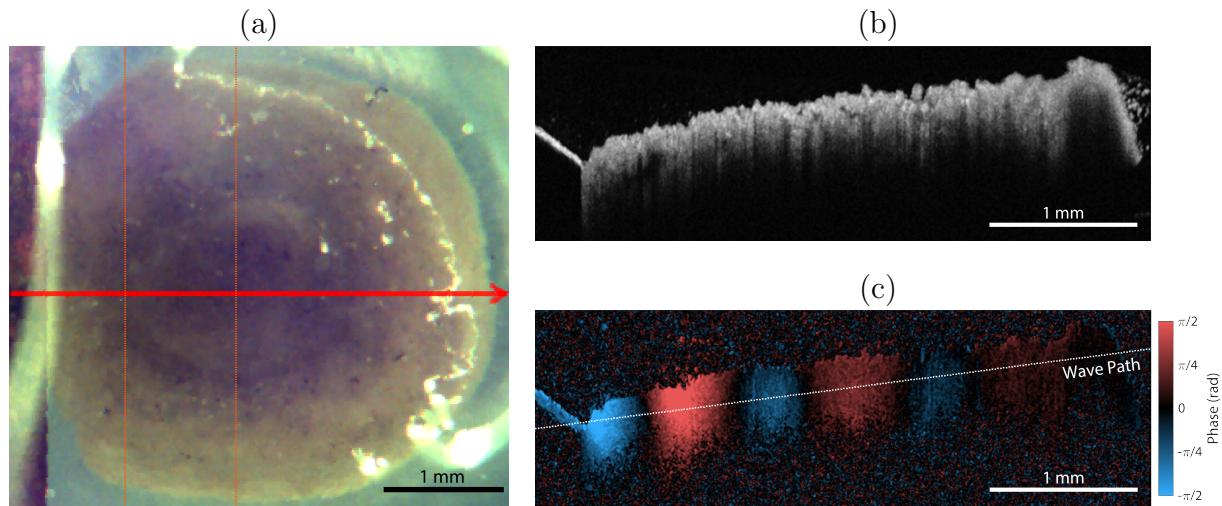


Figure 5.9: Images of the granular biofilm section recorded by the OCT microscope. (a) Camera image. (b) OCT image. (c) OCE image with wave excitation at 3.2 kHz.

that the layering in the granular biofilm only shows distinct color variation but an extreme property difference with a resolvable refractive index contrast.

The OCE image in Fig. 5.9c shows the displacement distribution of the elastic wave with excitation frequency at 3.2 kHz. From the figure, the elastic wavelength is comparable to the sample thickness; therefore, the wave propagates as a guided wave in this sample. Because the section was cut at the equator of the biofilm sphere, we can assume that property variation along the thickness is negligible and the change of the local wave speed would only be attributed to the lateral property variation.

25 OCE images were recorded at different time delay t from $t = 0$ to 0.3 ms. The displacement distribution extracted along the wave path (white dotted line) in Fig. 5.9c at each time delay was stacked in the acoustic B-scan (Fig. 5.10a). Note that because of the wave attenuation with propagation distance, the signal-to-noise ratio deteriorates dramatically after $x > 3$ mm. Therefore, the white circular dots that indicate the acoustic phase tracking in Fig. 5.10a were only marked until $x = 3$ mm. The estimation result for the local wave speed is presented in Fig. 5.10b. The orange dashed lines are the spatial

references associated with those in Fig. 5.9a. The local wave speed in Fig. 5.10b shows general symmetry with respect to the center of the biofilm sphere (second dashed line), and the local minimum at the first dashed line closely coincides with the layer boundary. These findings follow our expectation on the structure symmetry and the dependency of the local property on the morphology features, which validates the use of the two-layered model for predicting the wave propagation in granular biofilms.

To estimate the property contrast between the outer layer and inner core, we calculated the averaged wave speeds to be 4.57 m/s and 3.5 m/s for the outer layer and the inner core, respectively. This result shows the inner core has a slower wave speed and is approximately 76.6% referenced the outer layer. The lower wave speed of the inner core may be attributed to the higher biomass concentration in the mixture composed of both the bacterial cells and EPS, which will be verified by the experimental data presented in the next section.

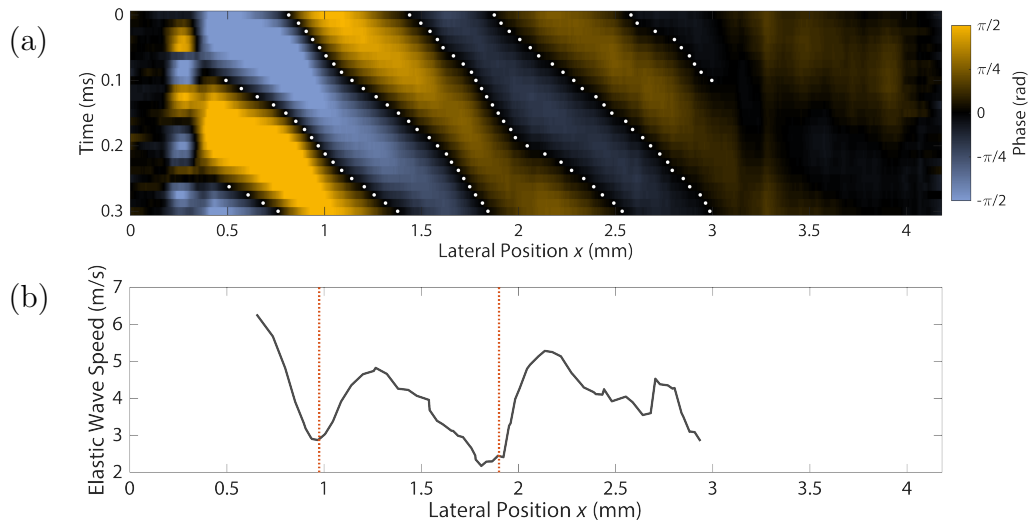


Figure 5.10: Measurement of local wave speed probing on the granular biofilm section. (a) Acoustic B-scan created by extracting $\Delta\phi$ from the white dashed line in Fig. 5.9c at different time delay. (b) Local wave speed estimated from the local slopes of the white dotted tracks in (a).

5.4. Viscoelastic Characterization of Alginate Gel Spheres with Biomass

The local probing experiment on the granular biofilm section suggested that the core of the granular biofilm has a lower shear wave speed (and hence a lower shear modulus). This may be attributed to the compositional difference between the two layers as the outer layer is dominantly composed of EPS and the inner core contains more microbial mass, according to the compositional model [7, 8, 17]. To validate this, we made two kinds of artificial granular biofilms and characterized their viscoelastic properties. The first kind of samples was pure alginate spheres to simulate the biofilm samples that only have the EPS layer (the outer layer), and the second kind was made of the same alginate concentration with an additional biomass content (the inner core). We followed the same protocol listed in Chapter 4 to prepare the samples. The alginate concentration was 1.2% w/v for both kinds, which is the same as the samples characterized in Chapter 4. The only difference to prepare the second kind samples is adding 15 mL of activated sludge when we made the 1.2% w/v alginate solution by stirring the mixture of 1.2 grams alginate powder, 30 ml 5.0% w/v skim milk solution, and 70 ml water. Primary settling effluent from the Terrance J. O'Brien wastewater treatment plant (Skokie, IL, USA) were used as source of suspended bacteria. The concentrations of Total Solids (TS), Total Suspended Solids (TSS) and Total Dissolved Solids (TDS) were determined according to *American Public Health Association Standard Methods for Examination of Water and Wastewater* (APHA 1992), and were found to be 963.5, 355.5 and 608 mg/L, respectively. 10 mL of biomass were centrifuged at 10,000 RPM for 5 minutes, concentrated down to 5 mL, and added to 45 mL of 1.2% alginate solution, leading to the final solids concentration of 192.8 mg/L. The viscoelastic properties of the samples were characterized through the same approach that we developed in Chapter 4; that is, recording OCE measurements at different frequencies, calculating the circumferential wave

speed for the experimental dispersion data, and estimating the shear modulus and viscosity by inverse modeling.

Fig. 5.11a and 5.11b show the OCT and OCE images of a sphere sample composed of alginate gel and biomass. The sample was submerged in water to simulate the granular biofilms submerged in their native aqueous solution. The white speckles in the OCT image are the biomass aggregates uniformly distributed in the sample. The OCE image was recorded with the excitation frequency at 1600 Hz. The white dotted line indicates the path where the displacement distribution of the circumferential wave was extracted for wavelength and wave speed estimation. By repeating the OCE image recording at different frequencies, the frequency-dependent wave speed was obtained.

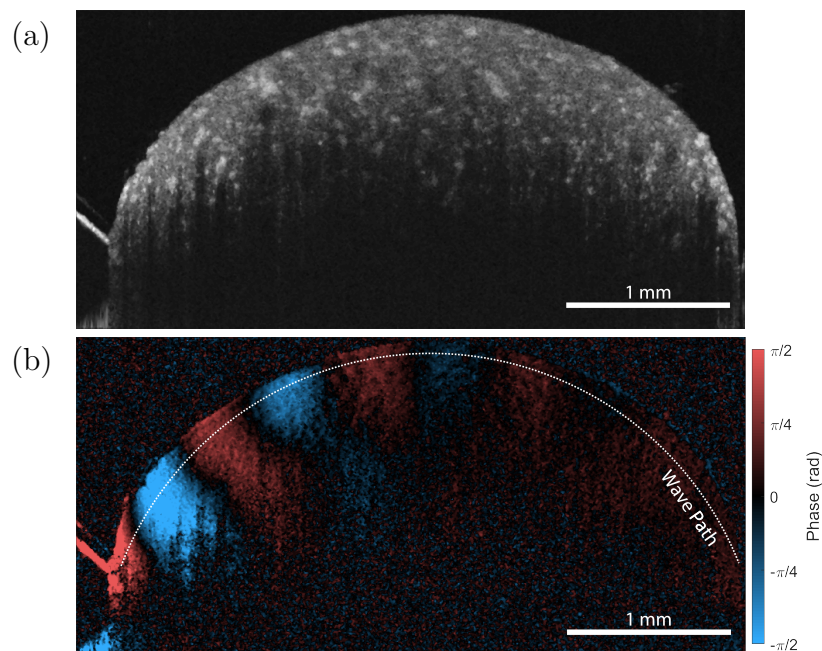


Figure 5.11: (a) OCT image and (b) OCE image for the artificial alginate gel sphere with biomass.

Fig. 5.12a to 5.12d show the frequency-dependent wave speeds estimated from the OCE measurements (circular dots) and the best-fit curves calculated by the theoretical model (black curve). Since the artificial samples discussed in this section only contained

one composition, the model used for their characterization was the single layer model. The result obtained from one pure alginate sphere sample is presented in Fig. 5.12a, and those from three alginate-with-biomass samples are presented in Fig. 5.12b, 5.12c, and 5.12d. We only conducted one measurement on the pure alginate sample here because the same measurements were made in Chapter 4, and the result in Fig. 5.12a is highly similar to what had been reported before, suggesting very good repeatability of this kind of samples. The result from this pure alginate sample also provides the comparison reference for the samples with biomass.

The three figures from the alginate-with-biomass samples share very similar trend and wave speed range. The experimental data of all three samples have their local minima of the wave speed and the wave speeds increase with frequency. Also, compared to the wave speed range in Fig. 5.12a, these three samples have lower wave speeds. According to our previous study, the speed increase with frequency suggests that the viscosity needs to be considered in the characterization with inverse modeling, and the lower speeds verify our expectation from the local probing measurement on the sectioned granular biofilm.

The data of the shear wave speed, shear modulus, and shear viscosity quantified from Fig. 5.12a to 5.12d are listed in Table 5.1 and visualized in Fig. 5.12e. Fig. 5.12e was plotted with shear viscosity against shear modulus. The circle on the right in the figure corresponds to the pure alginate sphere sample and the three circles on the left are the alginate-with-biomass samples. The figure shows that the former kind has higher shear modulus and viscosity than the latter kind. Moreover, based on the data in Table 5.1, we calculated the ratio of the shear wave speeds between the two kinds (1.3 m/s and 1.75 m/s) is 74.3%, referencing the pure alginate sample, and the ratio of shear viscosities is 53.8% (0.07 Pa-s to 0.13 Pa-s). We highlight that the ratio of the shear wave speeds is very similar to what we estimated on the sectioned biofilm. This means that the property difference observed in our

artificial samples would be representative for the difference between the outer layer and the inner core in the real granular biofilms. Hence, in the next section where we implemented the viscoelastic characterization of a granular biofilm through OCE measurements, the ratios will be used to determine the layer properties in the two-layered model for the inverse modeling.

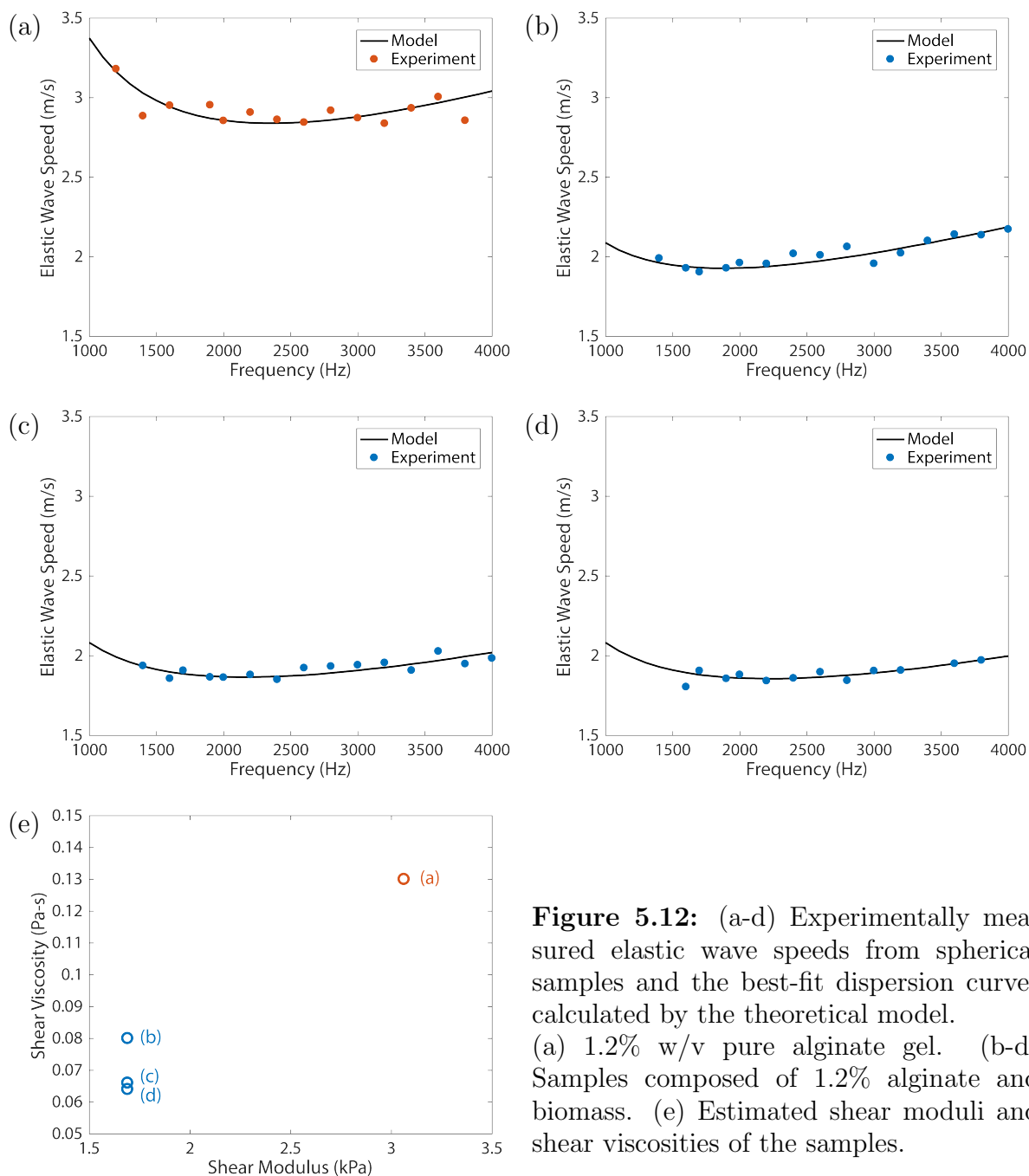


Figure 5.12: (a-d) Experimentally measured elastic wave speeds from spherical samples and the best-fit dispersion curves calculated by the theoretical model. (a) 1.2% w/v pure alginate gel. (b-d) Samples composed of 1.2% alginate and biomass. (e) Estimated shear moduli and shear viscosities of the samples.

Table 5.1: Model inputs and estimated properties for samples in Fig. 5.12.

Sample	(a)	(b)	(c)	(d)
Outer radius b (mm)	1.94	2.33	2.25	2.24
Density (kg/m ³)	1000	1000	1000	1000
Longitudinal wave speed (m/s)	1480	1480	1480	1480
Shear wave speed (m/s)	1.75	1.30	1.30	1.30
Shear modulus (kPa)	3.06	1.69	1.69	1.69
Complex shear viscosity (Pa-s)	0.13	0.08	0.066	0.064

5.5. Viscoelastic Characterization of a Granular Biofilm

The OCT image of the granular biofilm in Fig. 5.13a shows the curved geometry of the granular biofilm which is very close to a sphere. The floating speckles present near the biofilm surface are filament. The sample was submerged in its native aqueous solution from the AGS reactor to create a testing environment similar to the reactor. The intensity of the OCT image decays with depth due to the limited penetration depth of the OCT probe light. The penetration depth, indicated by the bright band underneath the sample surface, is approximately 0.5 mm and remains constant over the lateral extent. Within this bright band, we don't observe distinct structural features, which follows the compositional model that the material in the same layer would be relatively uniform.

Fig. 5.13b shows the OCE image recorded at 3400 Hz. Same as the previous OCE images, the white dotted line indicates the wave path where the displacement distribution was extracted to estimate the wavelength and the wave speed (1.62 mm and 5.5 m/s, respectively). The OCE measurements were repeated to obtain the frequency-dependent wave speed as shown in Fig. 5.13c. The ranges of the excitation frequency (up to 5600 Hz) and the measured wave speed for the granular biofilm are higher than the hydrogel samples due to its higher stiffness and stronger dynamic response at high frequencies. The black curve in Fig. 5.13c is the best-fit dispersion curve calculated by the theoretical model. The input parameters for this calculation are listed in Table 5.2. The results yield that the shear

modulus and viscosity of the outer layer is 8.41 kPa and 0.375 Pa-s, respectively, which are higher than but of the same order of magnitude with the pure alginate sphere, confirming that alginate has similar mechanical properties with the biofilms.

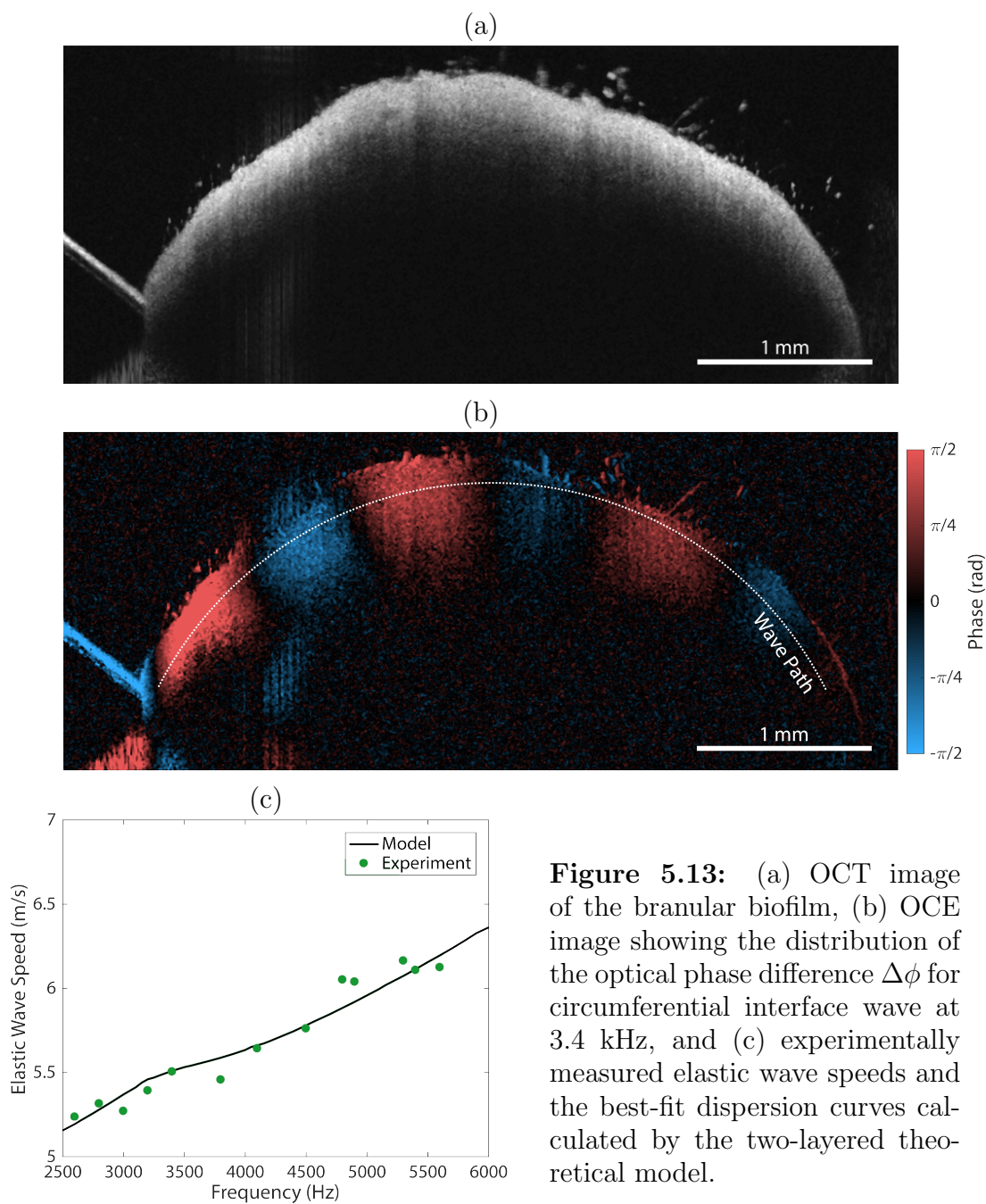


Figure 5.13: (a) OCT image of the branular biofilm, (b) OCE image showing the distribution of the optical phase difference $\Delta\phi$ for circumferential interface wave at 3.4 kHz, and (c) experimentally measured elastic wave speeds and the best-fit dispersion curves calculated by the two-layered theoretical model.

Table 5.2: Model inputs and estimated properties for the granular biofilm.

Sample	Granular biofilm
Outer radius b (mm)	2.29
Inner radius a (mm)	50% of b
Density (kg/m ³)	1000
Longitudinal wave speed (m/s)	1480
Shear wave speed of outer layer c_L^B (m/s)	2.90
Shear wave speed of inner layer c_L^A (m/s)	74.3% of c_L^B
Shear viscosity of outer layer η_μ^B (Pa-s)	0.375
Shear viscosity of inner layer η_μ^A (Pa-s)	53.8% of η_μ^B

5.6. Concluding Remarks

In this chapter, we modified the circumferential interface wave model developed in Chapter 4 to address the multi-layered structure in practical granular biofilms. The modified model can more precisely predict the circumferential interface wave propagation recorded by the OCE measurements, which leads to a more accurate estimation of the viscoelastic properties of the biofilm samples. The model requires the information—the sizes of the layers and the property contrast between the layers in the granular biofilms—as input for the dispersion curve calculation. Therefore, we developed a novel approach to probe local wave speed which is associated to the local properties in the material. The approach was investigated by a numerical simulation tool PZFlex to characterize its mechanical resolution and validated against an artificial heterogeneous agarose gel phantom composed of three layers of different agarose concentration. Then, we used this approach to probe the wave speed variation on a section of a granular biofilm, acquiring the property contrast between the layers. The findings regarding the property contrast was verified by two kinds of artificial alginate spheres which simulate the properties in different layers of the granular biofilms, including the ratio of the shear modulus and the ratio of the shear viscosity. At the end, the ratios were used in the two-layered cylindrical model for interpreting the dispersion data recorded by the OCE measurements on a practical granular biofilm.

The work presented in this chapter provides a useful tool to nondestructively characterize the viscoelastic properties of granular biofilms in practical applications, enabling further study of the relationships between growth conditions, morphology, and material properties. It also holds great potentials to evaluate practical material systems with complex composition and geometry.

CHAPTER 6

Conclusions and Future Work

6.1. Key Findings and Significance

This study demonstrates a first-of-its-kind metrology approach to characterize the viscoelastic properties of biofilms in mesoscale. This approach uses the OCE technique to measure the frequency-dependent phase velocity of elastic waves and interprets the OCE measurements by inverse modeling, yielding a quantitative estimation of biofilms' shear modulus and shear viscosity. Here the key achievements from Chapter 3 to Chapter 5 are summarized.

Chapter 3 laid the framework foundation of the metrology approach. The guided wave model was developed to predict theoretical dispersion curves given certain viscoelastic properties, thickness, and boundary conditions. The model was validated against a group of artificial agarose gel phantoms with different concentration (1.0% and 2.0% w/v) and thicknesses (10 mm and 1 mm). The material properties estimated by our approach were further confirmed by rheometry measurements. Finally, this approach was applied to a lab-developed mixed-culture planar biofilm. We successfully estimated the shear modulus and viscosity of the biofilm to be 429 Pa and 0.06 Pa-s, respectively, and these values fall within the range reported in the literature.

Chapter 4 and Chapter 5 investigated the viscoelastic characterization in granular biofilms, a different type of biofilms with sphere-like geometry. **Chapter 4** adapted the elastic wave model developed in Chapter 3 and modified the model geometry from a plate structure to a curved structure. The modified model involved Bessel functions with complex

orders, which caused tremendous challenges for numerical calculation, and required special numerical methods and approximations that are introduced in Section 4.2.2. A key finding from the model showed that the wave speed varies when structure's radius of curvature changes. Then, the model was validated against a group of artificial alginate spheres with different concentrations (0.8% and 1.2% w/v) and we obtained reasonable values of shear modulus (1.78 kPa and 3.64 kPa, respectively, in average) and viscosity (0.058 Pa-s and 0.134 Pa-s, respectively, in average) that have good agreement with those reported in the literature.

Chapter 5 extended the model efforts from Chapter 4 and added one more layer in the curved structure for more closely approximating the wave propagation in granular biofilms. A new method to probe local wave speed from OCE measurements was also developed to provide required parameters for the two-layered model. The new method was investigated by a numerical simulation tool PZFlex to characterize its mechanical resolution, and validated against an artificial multi-layered agarose gel phantom. It was then applied to a granular biofilm section to estimate its local property variation. These estimations were verified by another group of artificial samples (alginate spheres mixed with biomass). Finally, combining all necessary information acquired, the two-layered model was used for inverse modeling, interpreting the OCE measurements on a granular biofilm and obtaining its shear modulus and viscosity to be 8.41 kPa and 0.375 Pa-s, respectively.

We remark that there is no standard measurement for mechanical properties in soft materials and biofilms. The nondestructive technique presented in this work developed a novel metrology approach for characterizing these properties in mesoscale without affecting the original status of the samples. A huge advantage of using OCE is that it provides co-registered morphology image (OCT image) and dynamic measurement (OCE image) that

can facilitate the study of the relationship between them. Other studies including 3D heterogeneity mapping and the relationships between morphology, material properties, and growth environment can also be realized by the developed tool.

6.2. Opportunities for Future Work

The metrology approach presented in this dissertation is a powerful tool for viscoelastic property characterization of biofilm. Within the scope layout in Fig. 1.1, one may proceed to study the relationships between mechanical properties, growth conditions, and gene expression. Particularly for granular biofilms in wastewater treatment reactors, the granulation mechanism, and the conditions that lead to controllable and stable granular biofilms are still understudied. Such studies would facilitate the understanding of these unsolved questions and ultimately enhance the efficiency both in time and cost for wastewater processing.

The models presented in this work assumed ideal geometry and material properties. However, in the real world, biofilms may have surface roughness, thickness variation, heterogeneity, and anisotropic material properties. The effect caused by these factors on elastic wave propagation is worth exploring. The model of guided wave propagating in a thickness-varying structure may find applications not only in biofilm and environmental engineering, but also in biomedical field. One potential application is using the circumferential wave model for viscoelastic characterization of the cornea, which may be used as a predictive tool for evaluating ophthalmic disease state [60, 102].

References

- [1] H. Kanematsu and D.M. Barry. *Biofilm and Materials Science*. Springer, Cham, 2015.
- [2] V.D. Gordon et al. “Biofilms and mechanics: a review of experimental techniques and findings,” in: *Journal of Physics D: Applied Physics* 50.22 (2017).
- [3] L. Hall-Stoodley, J.W. Costerton, and P. Stoodley. “Bacterial biofilms: from the natural environment to infectious diseases,” in: *Nat Rev Microbiol* 2.2 (Feb. 2004), pp. 95–108.
- [4] J.N. Wilking et al. “Biofilms as complex fluids,” in: *MRS Bulletin* 36.5 (2011), pp. 385–391.
- [5] H.C. Flemming et al. “Biofilms: an emergent form of bacterial life,” in: *Nat Rev Microbiol* 14.9 (2016), pp. 563–75.
- [6] K. Milferstedt. “Biogranules applied in environmental engineering,” in: *International Journal of Hydrogen Energy* 42.45 (2017), pp. 27801–27811.
- [7] S.J. Sarma, J.H. Tay, and A. Chu. “Finding Knowledge Gaps in Aerobic Granulation Technology,” in: *Trends Biotechnol* 35.1 (Jan. 2017), pp. 66–78.
- [8] X.W. Liu, G.P. Sheng, and H.Q. Yu. “Physicochemical characteristics of microbial granules,” in: *Biotechnol Adv* 27.6 (Nov. 2009), pp. 1061–1070.
- [9] Q. Zhang, J. Hu, and D.J. Lee. “Aerobic granular processes: Current research trends,” in: *Bioresour Technol* 210 (June 2016), pp. 74–80.
- [10] C.H. Tan. “Community quorum sensing signalling and quenching: microbial granular biofilm assembly,” in: *NPJ Biofilms Microbiomes* 1 (2015), p. 15006.

- [11] H.F. Wang et al. “Characterization of anaerobic granular sludge using a rheological approach,” in: *Water Res* 106 (Dec. 1, 2016), pp. 116–125.
- [12] Y. Liu and J.-H. Tay. “The essential role of hydrodynamic shear force in the formation of biofilm and granular sludge,” in: *Water Research* 36.7 (2002), pp. 1653–1665.
- [13] S.G.V. Charlton. “Regulating, measuring and modelling the viscoelasticity of bacterial biofilms,” in: Jun 10, 2019.
- [14] H.-C. Flemming, T.R. Neu, and J. Wingender. *The Perfect Slime: Microbial Extracellular Polymeric Substances (EPS)*. 2016.
- [15] S.S. Adav, D.J. Lee, and J.H. Tay. “Extracellular polymeric substances and structural stability of aerobic granule,” in: *Water Res* 42.6-7 (Mar. 2008), pp. 1644–50.
- [16] C. Caudan et al. “Multiple EPS interactions involved in the cohesion and structure of aerobic granules,” in: *Chemosphere* 117 (Dec. 2014), pp. 262–70.
- [17] Z. Ding. “Role of extracellular polymeric substances (EPS) production in bioaggregation: application to wastewater treatment,” in: *Appl Microbiol Biotechnol* 99.23 (Dec. 2015), pp. 9883–905.
- [18] L. Zhu et al. “Role and significance of extracellular polymeric substances on the property of aerobic granule,” in: *Bioresour Technol* 107 (Mar. 2012), pp. 46–54.
- [19] T. Seviour et al. “Understanding the properties of aerobic sludge granules as hydrogels,” in: *Biotechnol Bioeng* 102.5 (Apr. 1, 2009), pp. 1483–93.
- [20] K.M. Colvin. “The pel polysaccharide can serve a structural and protective role in the biofilm matrix of *Pseudomonas aeruginosa*,” in: *PLoS Pathog* 7.1 (2011), p. 1001264.
- [21] J.J. Harrison, H. Ceri, and R.J. Turner. “Multimetal resistance and tolerance in microbial biofilms,” in: *Nat Rev Microbiol* 5.12 (Dec. 2007), pp. 928–38.
- [22] P.S. Stewart and J. William Costerton. “Antibiotic resistance of bacteria in biofilms,” in: *The Lancet* 358.9276 (2001), pp. 135–138.

- [23] T.-F.C. Mah and G.A. O'Toole. "Mechanisms of biofilm resistance to antimicrobial agents," in: *Trends in Microbiology* 9.1 (2001), pp. 34–39.
- [24] Y. Salama et al. "Characterization, structure, and function of extracellular polymeric substances (EPS) of microbial biofilm in biological wastewater treatment systems: a review," in: *Desalination and Water Treatment* 57.35 (2016), pp. 16220–16237.
- [25] Y. Wang. "Identification of the function of extracellular polymeric substances (EPS) in denitrifying phosphorus removal sludge in the presence of copper ion," in: *Water Res* 73 (2015), pp. 252–64.
- [26] X. Lin and Y. Wang. "Microstructure of anammox granules and mechanisms endowing their intensity revealed by microscopic inspection and rheometry," in: *Water Res* 120 (Sept. 1, 2017), pp. 22–31.
- [27] Y.J. Ma et al. "A rheological approach to analyze aerobic granular sludge," in: *Water Res* 50 (Mar. 1, 2014), pp. 171–8.
- [28] Y.M. Lin, P.K. Sharma, and M.C. van Loosdrecht. "The chemical and mechanical differences between alginate-like exopolysaccharides isolated from aerobic flocculent sludge and aerobic granular sludge," in: *Water Res* 47.1 (Jan. 1, 2013), pp. 57–65.
- [29] T. Seviour et al. "Gel-forming exopolysaccharides explain basic differences between structures of aerobic sludge granules and floccular sludges," in: *Water Res* 43.18 (Oct. 2009), pp. 4469–78.
- [30] V. Sekkar et al. "Evaluation by various experimental approaches of the crosslink density of urethane networks based on hydroxyl-terminated polybutadiene," in: *Journal of Applied Polymer Science* 103.5 (2007), pp. 3129–3133.
- [31] C.J. Rupp, C.A. Fux, and P. Stoodley. "Viscoelasticity of *Staphylococcus aureus* biofilms in response to fluid shear allows resistance to detachment and facilitates rolling migration," in: *Appl Environ Microbiol* 71.4 (Apr. 2005), pp. 2175–8.

- [32] V. Körstgens et al. “Uniaxial compression measurement device for investigation of the mechanical stability of biofilms,” in: *Journal of Microbiological Methods* 46.1 (2001), pp. 9–17.
- [33] C. Douarche, J.M. Allain, and E. Raspaud. “Bacillus subtilis Bacteria Generate an Internal Mechanical Force within a Biofilm,” in: *Biophys J* 109.10 (2015), pp. 2195–202.
- [34] E.C. Hollenbeck. “Mechanical Behavior of a Bacillus subtilis Pellicle,” in: *J Phys Chem B* 120.26 (2016), pp. 6080–8.
- [35] E.H. Poppele and R.M. Hozalski. “Micro-cantilever method for measuring the tensile strength of biofilms and microbial flocs,” in: *Journal of Microbiological Methods* 55.3 (2003), pp. 607–615.
- [36] S. Aggarwal, E.H. Poppele, and R.M. Hozalski. “Development and testing of a novel microcantilever technique for measuring the cohesive strength of intact biofilms,” in: *Biotechnol Bioeng* 105.5 (Apr. 1, 2010), pp. 924–34.
- [37] B.J. Cooley. “The extracellular polysaccharide Pel makes the attachment of *P. aeruginosa* to surfaces symmetric and short-ranged,” in: *Soft Matter* 9.14 (2013), pp. 3871–3876.
- [38] G. Zeng, T. Muller, and R.L. Meyer. “Single-cell force spectroscopy of bacteria enabled by naturally derived proteins,” in: *Langmuir* 30.14 (2014), pp. 4019–25.
- [39] Y. Chen et al. “Viscous nature of the bond between adhering bacteria and substratum surfaces probed by atomic force microscopy,” in: *Langmuir* 30.11 (Mar. 25, 2014), pp. 3165–9.
- [40] O. Galy et al. “Mapping of bacterial biofilm local mechanics by magnetic microparticle actuation,” in: *Biophys J* 103.6 (Sept. 19, 2012), pp. 1400–8.

- [41] A. Ashkin et al. “Observation of a single-beam gradient force optical trap for dielectric particles,” in: *Optics Letters* 11.5 (1986), pp. 288–290.
- [42] A. Keloth et al. “Single Cell Isolation Using Optical Tweezers,” in: *Micromachines (Basel)* 9.9 (2018).
- [43] N. Leartprapun et al. “Photonic force optical coherence elastography for three-dimensional mechanical microscopy,” in: *Nat Commun* 9.1 (May 25, 2019), p.
- [44] C.D. Chapman et al. “Onset of Non-Continuum Effects in Microrheology of Entangled Polymer Solutions,” in: *Macromolecules* 47.3 (2014), pp. 1181–1186.
- [45] B.W. Towler et al. “Viscoelastic Properties of a Mixed Culture Biofilm from Rheometer Creep Analysis,” in: *Biofouling* 19.5 (2003), pp. 279–285.
- [46] D.N. Hohne, J.G. Younger, and M.J. Solomon. “Flexible microfluidic device for mechanical property characterization of soft viscoelastic solids such as bacterial biofilms,” in: *Langmuir* 25.13 (2009), pp. 7743–51.
- [47] J.D. Mathias and P. Stoodley. “Applying the digital image correlation method to estimate the mechanical properties of bacterial biofilms subjected to a wall shear stress,” in: *Biofouling* 25.8 (2009), pp. 695–703.
- [48] P.C. Lau et al. “Absolute quantitation of bacterial biofilm adhesion and viscoelasticity by microbead force spectroscopy,” in: *Biophys J* 96.7 (2009), pp. 2935–48.
- [49] F.C. Cheong et al. “Holographic microrheology of polysaccharides from *Streptococcus mutans* biofilms,” in: *Rheologica Acta* 48.1 (2008), pp. 109–115.
- [50] E. Morgenroth and K. Milferstedt. “Biofilm engineering: linking biofilm development at different length and time scales,” in: *Reviews in Environmental Science and Bio/Tech-nology* 8.3 (2009), pp. 203–208.

- [51] M. Wagner et al. “Investigation of the mesoscale structure and volumetric features of biofilms using optical coherence tomography,” in: *Biotechnol Bioeng* 107.5 (Dec. 1, 2010), pp. 844–53.
- [52] A. Manduca. “Magnetic resonance elastography: Non-invasive mapping of tissue elasticity,” in: *Medical Image Analysis* 5.4 (2001), pp. 237–254.
- [53] T.A. Krouskop et al. “Elastic Moduli of Breast and Prostate Tissues under Compression,” in: *Ultrasonic Imaging* 20.4 (1998), pp. 260–274.
- [54] J. Ophir et al. “Elastography: A Quantitative Method for Imaging the Elasticity of Biological Tissues,” in: *Ultrasonic Imaging* 13.2 (1991), pp. 111–134.
- [55] B.F. Kennedy, K.M. Kennedy, and D.D. Sampson. “A Review of Optical Coherence Elastography: Fundamentals, Techniques and Prospects,” in: *IEEE Journal of Selected Topics in Quantum Electronics* 20.2 (2014), pp. 272–288.
- [56] X. Liang, V. Crecea, and S.A. Boppart. “Dynamic Optical Coherence Elastography: A Review,” in: *Journal of Innovative Optical Health Sciences* 3.4 (2010), pp. 221–233.
- [57] M. Wagner and H. Horn. “Optical coherence tomography in biofilm research: A comprehensive review,” in: *Biotechnol Bioeng* 114.7 (July 2017), pp. 1386–1402.
- [58] K.V. Larin and D.D. Sampson. “Optical coherence elastography - OCT at work in tissue biomechanics,” in: *Biomed Opt Express* 8.2 (Feb. 1, 2017), pp. 1172–1202.
- [59] S. Wang and K.V. Larin. “Optical coherence elastography for tissue characterization: a review,” in: *J Biophotonics* 8.4 (Apr. 2015), pp. 279–302.
- [60] L. Ambrozinski. “Acoustic micro-tapping for non-contact 4D imaging of tissue elasticity,” in: *Sci Rep* 6 (Dec. 23, 2016), p. 38967.
- [61] S. Song. “Shear modulus imaging by direct visualization of propagating shear waves with phase-sensitive optical coherence tomography,” in: *J Biomed Opt* 18.12 (Dec. 2013), p. 121509.

- [62] V. Crecea, A. Ahmad, and S.A. Boppart. “Magnetomotive optical coherence elastography for microrheology of biological tissues,” in: *J Biomed Opt* 18.12 (Dec. 2013), p. 121504.
- [63] M.A. Kirby. “Optical coherence elastography in ophthalmology,” in: *J Biomed Opt* 22.12 (Dec. 2017), pp. 1–28.
- [64] A.F. Rosenthal et al. “Morphological analysis of pore size and connectivity in a thick mixed-culture biofilm,” in: *Biotechnol Bioeng* 115.9 (Sept. 2018), pp. 2268–2279.
- [65] C. Li. “Detection and characterisation of biopsy tissue using quantitative optical coherence elastography (OCE) in men with suspected prostate cancer,” in: *Cancer Lett* 357.1 (Feb. 1, 2015), pp. 121–128.
- [66] X. Liang et al. “Dynamic spectral-domain optical coherence elastography for tissue characterization,” in: *Optics Express* 18.13 (2010), pp. 14183–14190.
- [67] M. Razani. “Optical coherence tomography detection of shear wave propagation in inhomogeneous tissue equivalent phantoms and ex-vivo carotid artery samples,” in: *Biomed Opt Express* 5.3 (Mar. 1, 2014), pp. 895–906.
- [68] S. Song et al. “Quantitative shear-wave optical coherence elastography with a programmable phased array ultrasound as the wave source,” in: *Opt Lett* 40.21 (Nov. 1, 2015), pp. 5007–10.
- [69] J. Zhu. “Imaging and characterizing shear wave and shear modulus under orthogonal acoustic radiation force excitation using OCT Doppler variance method,” in: *Opt Lett* 40.9 (May 1, 2015), pp. 2099–102.
- [70] V. Crecea et al. “Magnetomotive nanoparticle transducers for optical rheology of viscoelastic materials,” in: *Optics Express* 17.25 (2009), pp. 23114–23122.

- [71] P.C. Huang. “Magnetomotive Optical Coherence Elastography for Magnetic Hyperthermia Dosimetry Based on Dynamic Tissue Biomechanics,” in: *IEEE J Sel Top Quantum Electron* 22.4 (2016).
- [72] S. Wang and K.V. Larin. “Shear wave imaging optical coherence tomography (SWI-OCT) for ocular tissue biomechanics,” in: *Opt Lett* 39.1 (Jan. 1, 2014), pp. 41–4.
- [73] P. Stoodley et al. “Biofilms as complex differentiated communities,” in: *Annu Rev Microbiol* 56 (2002), pp. 187–209.
- [74] R.M. Donlan. “Biofilms: microbial life on surfaces,” in: *Emerging infectious diseases* 8.9 (2002), pp. 881–890.
- [75] J. Wimpenny, W. Manz, and U. Szewzyk. “Heterogeneity in biofilms,” in: *FEMS Microbiology Reviews* 24.5 (2000), pp. 661–671.
- [76] J.W. Costerton et al. “Microbial Biofilms,” in: *Annual Review of Microbiology* 49.1 (1995), pp. 711–745.
- [77] M. Couade. “Quantitative assessment of arterial wall biomechanical properties using shear wave imaging,” in: *Ultrasound Med Biol* 36.10 (Oct. 2010), pp. 1662–76.
- [78] J. Laperre and W. Thys. “Experimental and theoretical study of Lamb wave dispersion in aluminum/polymer bilayers,” in: *The Journal of the Acoustical Society of America* 94.1 (1993), pp. 268–278.
- [79] Z. Zhu and J. Wu. “The propagation of Lamb waves in a plate bordered with a viscous liquid,” in: *The Journal of the Acoustical Society of America* 98.2 (1995), pp. 1057–1064.
- [80] F. Simonetti. “Lamb wave propagation in elastic plates coated with viscoelastic materials,” in: *The Journal of the Acoustical Society of America* 115.5 (2004), pp. 2041–2053.

- [81] A.F. Fercher et al. “Measurement of intraocular distances by backscattering spectral interferometry,” in: *Optics Communications* 117.1 (1995), pp. 43–48.
- [82] G. Haeusler and M.W. Lindner. “Coherence radar and Spectral radar—new tools for dermatological diagnosis,” in: *Journal of Biomedical Optics* 3.1 (1998), pp. 21–31.
- [83] J.D. Achenbach. *Wave Propagation in Elastic Solids*. Amsterdam/New York: North-Holland Publishing Company/American Elsevier, 1973.
- [84] M.J.S. Lowe. “Matrix techniques for modeling ultrasonic waves in multilayered media,” in: *IEEE Transactions on Ultrasonics, Ferroelectrics, and Frequency Control* 42.4 (1995), pp. 525–542.
- [85] J.L. Rose. *Ultrasonic waves in solid media*. Cambridge University Press, 1999.
- [86] N.A. Haskell. “The dispersion of surface waves on multilayered media*,” in: *Bulletin of the Seismological Society of America* 43.1 (1953), pp. 17–34.
- [87] W.T. Thomson. “Transmission of Elastic Waves through a Stratified Solid Medium,” in: *Journal of Applied Physics* 21.2 (1950), pp. 89–93.
- [88] I.A. Viktorov. *Rayleigh and Lamb waves: physical theory and applications*. New York: Plenum Press, 1967.
- [89] B.N. Pavlakovic et al. *Disperse: A General Purpose Program for Creating Dispersion Curves*, 1997.
- [90] C.B. Scruby. *Laser ultrasonics: techniques and applications*. A. Hilger, 1990.
- [91] H. Boudarel et al. “Towards standardized mechanical characterization of microbial biofilms: analysis and critical review,” in: *NPJ Biofilms Microbiomes* 4 (2018), p. 17.
- [92] M. Jafari et al. “Effect of biofilm structural deformation on hydraulic resistance during ultrafiltration: A numerical and experimental study,” in: *Water Res* 145 (Nov. 15, 2018), pp. 375–387.

- [93] B.W. Peterson. “Viscoelasticity of biofilms and their recalcitrance to mechanical and chemical challenges,” in: *FEMS Microbiol Rev* 39.2 (Mar. 2015), pp. 234–45.
- [94] S. Felz et al. “Extraction of Structural Extracellular Polymeric Substances from Aerobic Granular Sludge,” in: *JoVE* 115 (2016), p. 54534.
- [95] S. Towfighi and T. Kundu. “Elastic wave propagation in anisotropic spherical curved plates,” in: *International Journal of Solids and Structures* 40.20 (2003), pp. 5495–5510.
- [96] J. Yu et al. “Characteristics of guided waves in anisotropic spherical curved plates,” in: *Wave Motion* 44.4 (2007), pp. 271–281.
- [97] G. Liu and J. Qu. “Guided Circumferential Waves in a Circular Annulus,” in: *Journal of Applied Mechanics* 65.2 (1998), pp. 424–430.
- [98] K.L.J. Fong. “A study of Curvature Effects on Guided Elastic Waves,” in: Imperial College London, London, 2005.
- [99] M. Abramowitz and I.A. Stegun. *Handbook of mathematical functions: with formulas, graphs, and mathematical tables*. Ed. by D. C 1972 with corrections Washington. Dec. 1972.
- [100] C.-C. Chang and S.-K. Tseng. “Immobilization of *Alcaligenes eutrophus* using PVA crosslinked with sodium nitrate,” in: *Biotechnology Techniques* 12.12 (1998), pp. 865–868.
- [101] M.A. LeRoux, F. Guilak, and L.A. Setton. “Compressive and shear properties of alginate gel: Effects of sodium ions and alginate concentration,” in: *Journal of Biomedical Materials Research* 47.1 (1999), pp. 46–53.
- [102] A. Ramier, B. Tavakol, and S.H. Yun. “Measuring mechanical wave speed, dispersion, and viscoelastic modulus of the cornea using optical coherence elastography,” in: *Opt Express* 27.12 (2019), pp. 16635–16649.